
The Interplay of Pressure and Doping Effects on BaFe_2As_2 Superconductors

A DISSERTATION SUBMITTED TO

TE HERENGA WAKA - VICTORIA UNIVERSITY OF WELLINGTON

IN PARTIAL FULFILMENT OF THE REQUIREMENTS FOR THE DEGREE OF

DOCTOR OF PHILOSOPHY

BY

GABRIEL BIOLETTI



8TH MARCH 2022

ABSTRACT

The study of iron-based superconductors exists at the intersection of some of the most fascinating disciplines in physical sciences, with avenues to reach illuminating conclusions in the study of magnetism, quantum physics, materials science, and applications at the forefront of technical engineering. The youth of the field is apparent, having only been discovered in 2008, with many open questions as to how the many facets of their normal-state and superconducting properties intermingle, and behave under the extreme conditions made imperative by their significant promise of applicability in magnet technologies.

This thesis hones in on the study of BaFe_2As_2 and the way in which isovalent doping with phosphorous, charge doping with nickel, and the application of intermediate amounts of hydrostatic pressure (1.2 GPa) affect its superconducting critical current density (J_c) and superconducting critical temperature (T_c). This avenue of study already provides a multitude of interesting results.

We uncover a significantly orientation dependent sharp peak in the Ni-doping dependent phase diagram, coincident with a large increase in the susceptibility of J_c to applied pressure. Pressure applied at the optimal doping of $\text{Ba}(\text{Fe}_{0.95}\text{Ni}_{0.05})_2\text{As}_2$ result in increases of 300 %, drastically up from 50 % $\text{Ba}(\text{Fe}_{0.95}\text{Ni}_{0.048})_2\text{As}_2$, exemplifying a behaviour correlated with the posited quantum critical point (QCP) at this doping. The fact that this striking behaviour only manifests in a field oriented perpendicular to the materials ab-plane at ambient pressure, reinforced by the application of Dew-Hughes and strong pinning models, makes a strong case for it being

a phenomena dependent on the coexistence of both δT_c and δI forms of pinning.

The behaviour of the phosphorous doped material is immediately contrasting, with changes in J_c completely correlated with changes in T_c . The behaviour of T_c under applied pressures illuminates a non-linear response at low pressures due to the difference in compressibility of orthogonal lattice parameters along the c and a axes. This effect results in huge suppression of T_c with the optimally doped sample displaying a shift from $T_c = 29$ to 15.5 K at a rate of 35 K/GPa. Further analysis shows that this may be related to a softening in the structural lattice induced by the P-doping.

This work exemplifies the complex nature of the interacting material and superconducting properties of BaFe_2As_2 , and will prove useful to any future research attempting to optimise BaFe_2As_2 for future application as well as filling out the body of work necessary to understand the nature of superconductivity in iron-based superconductors.

ACKNOWLEDGEMENTS

As is the case for any extended period of time, there are myriad people to thank, and for many reasons. But, the thanks I owe for this particular period of time are beyond any I have previously given. The dedication needed for this intense and extended sojourn into the world of physics research did not come solely from within. The simple pleasure of working beside someone, the contributions of expertise and aid without which my accomplishments would simply not be feasible, and the consistent support of those around me are as much a part of this accomplishment as my own faculties.

First of all, thank you Shen Chong and Grant Williams, I appreciate your supervision, expertise, and understanding in helping me for the last 3.5 years. I have learnt a great deal over this time, and so much of that learning came from you both.

A huge thank you to David Uhrig, we were a team, and your consistent presence, conversation, and input was invaluable to me. Other fellow students; Tom Nott, Ratu Mataira, Gus Brooks, Joe Schuyt, Hellen Nalumaga, Tehreema Nawaz, and others. I appreciate the conversations, presentations, writing sessions - I needed them.

Finally, a huge thank you to my family, particularly my parents. This is the culmination of over 20 years of education, and I have never for one moment felt like this was beyond me. My confidence stems indubitably from your consistent and unwavering support.

CONTENTS

1	INTRODUCTION	3
2	THEORY/LITERATURE REVIEW	7
2.1	Basic Superconductivity	8
2.1.1	Penetration depth and Coherence Length	9
2.1.2	Macroscopic parameters	13
2.2	Vortices and Pinning Models	16
2.2.1	Single Vortex Pinning	18
2.2.2	Weak-collective Pinning	20
2.2.3	Strong Pinning	23
2.2.4	Dew-Hughes Theory	25
2.2.5	δT_c and δl pinning	28
2.3	Iron-based Superconductors	28
2.3.1	Structure	29
2.3.2	Higher temperature transitions	32
2.3.3	Quantum Critical Points	34
2.4	Pressure Studies	36
2.4.1	Induced superconductivity in parent compounds	37
2.4.2	Effect on T_c and J_c	38
2.5	Research Questions	39
3	EXPERIMENTAL METHODS	41
3.1	Samples	41
3.1.1	Self-flux Methods	41
3.1.2	Lattice Parameter Determination	42
3.1.3	Resistive measurements	42
3.2	Magnetic Measurements	44
3.2.1	Zero-Field Cooled (ZFC) measurements	48
3.2.2	Hysteresis Measurements and Bean Model	49

3.3	Pressure Methods	52
3.3.1	Calibration	52
3.3.2	Background Measurements	54
4	PRESSURE EFFECTS ON ISOVALENTLY DOPED $\text{BaFe}_2(\text{As}_{1-x}\text{P}_x)_2$	57
4.1	Doping dependent measurements	58
4.1.1	Temperature Dependent Magnetisation	59
4.1.2	Transition Temperature versus Doping	63
4.1.3	Magnetic Hysteresis Loops	64
4.1.4	Critical Current Density versus Applied Field	69
4.1.5	J_c versus Doping	75
4.2	Pressure dependence	76
4.2.1	Effects of a Pressurisation Cycle on Samples	76
4.2.2	Transition Temperature versus Pressure	80
4.2.3	Magnetic Hysteresis Loops	88
4.2.4	Pressure Effects on Critical Current Density	88
4.2.5	Comparison to Previous Pressure Studies	90
4.3	Conclusions	93
5	DOPING DEPENDENT PROPERTIES OF $\text{Ba}(\text{Fe}_{1-x}\text{Ni}_x)_2\text{As}_2$ SINGLE CRYSTALS	95
5.1	Temperature Dependent Magnetisation	97
5.1.1	Transition Temperature versus Doping	98
5.2	Critical Current Density versus Applied Field	103
5.2.1	J_c versus Doping	108
5.3	Pinning Analyses	109
5.3.1	Dew-Hughes	109
5.3.2	Strong Pinning	116
5.3.3	Temperature Dependent Pinning	120
5.4	Conclusion	124
6	PRESSURE DEPENDENT PROPERTIES OF $\text{Ba}(\text{Fe}_{1-x}\text{Ni}_x)_2\text{As}_2$ SINGLE CRYSTALS	127
6.1	Transition Temperature Measurements	128

6.1.1	Temperature Dependent Magnetisation versus Pressure	128
6.1.2	Transition Temperature versus Pressure	130
6.2	Magnetic Hysteresis Loops	135
6.3	Critical Current Density versus Applied Field	137
6.3.1	Pressure results by sample	138
6.3.2	Pressure Effects on Critical Current Density	147
6.4	Conclusion	152
7	CONCLUSIONS	155
	BIBLIOGRAPHY	157

ACRONYMS

BCS - The Bardeen-Schrieffer-Cooper theory of superconductivity.

FeSC - Iron-Based Superconductor.

HTS - High Temperature Superconductivity.

MPMS - Magnetic Property Measurement System.

NMR - Nuclear Magnetic Resonance.

PPMS - Physical Property Measurement System.

QCP - Quantum Critical Point.

RSO - Reciprocating Sample Option.

SQUID - Superconducting Quantum Interference Device.

COMMONLY USED PARAMETERS

a - The vortex lattice parameter.

a - Lattice parameter aligned with the x-axis of the unit cell.

c - Lattice parameter aligned with the z-axis of the unit cell.

Δl - Pinning derived from spatial fluctuations of the charge carrier mean free path.

ΔT_c - Pinning derived from spatial fluctuations of T_c .

ϵ_1 - The line tension of a vortex.

F_p - The Pinning force = $J_c \times H$.

γ - anisotropy.

G_i - The Ginzburg number.

H_c - Superconducting thermodynamic critical field.

H_{c1} - Superconducting lower critical field.

H_{c2} - Superconducting upper critical field.

H_{irr} - Irreversibility field.

h_{max} - The reduced magnetic field value at the pinning force maximum.

J_0 - The superconducting depairing current density.

J_c - The superconducting critical current density.

κ - Ginzberg-Landau parameter = λ/ξ .

l - Mean free path.

λ - Superconducting penetration depth.

λ_L - London penetration depth.

L_c - Collective pinning length.

μ - The strong pinning power-law exponent.

n_p - Density of pinning centers.

Φ - The magnetic flux quantum.

Q_u - Quantum resistance parameter.

R_c - Collective pinning radius.

r_p - maximum displacement of a pinned vortex perpendicular to it's length.

T_c - Superconducting transition temperature.

T_S - Structural transition temperature.

T_N - Neel Temperature.

u_p - Potential energy of a single vortex.

ξ - Superconducting coherence length.

INTRODUCTION

Superconductivity is a field periodically overturned by startling, seemingly fortuitous, and out-of-the blue discoveries - it's discovery in 1908 being simply the first in a long line of experiments puzzling the minds of theoretical physicists, now for over a century.

The discovery of zero resistivity below 4 K in mercury at the Leiden Physics Laboratory was a result of investigation into the possible theories of low temperature resistivity in metals - of which, a sudden drop to zero resistivity was in no way considered as a candidate. At the time, Kamerlingh Onnes owned a monopoly on the production of liquid helium worldwide, a reasonable prize for the amount of time and effort that had been poured into the problem. From the time he was appointed the first chair in physics at the University of Leiden, it had taken Onnes and his cohort of technicians and students 25 years to successfully liquefy helium, and it was yet another 15 years before another lab managed to replicate the effort. Thus, the hidden gem of superconductivity was his for the taking.

Onnes commissioned a student named Gilles Holst to undertake high-precision measurements of the low temperature resistivity of mercury, in an attempt to distinguish between the different predominant theories of what happens to resistivity at low temperatures. In particular, Albert Einstein's theory of quantum oscillators which posited the existence of thermal oscillations which impeded the flow of current, an effect which would diminish at low temperatures thus explaining the diminishing of resistivity in metals. However, what was observed was a sharp drop from a value of 0.08 Ω above 4

K to a value south of the sensitivity limits of the experiment which were approximately 3×10^{-6} K.

Further intrigue followed an experiment conducted by Walther Meissner and Robert Oschenfeld in 1933, in which they had been attempting to ascertain whether currents in a superconductor flowed in the surface or bulk of the material. Results of the experiment showed that the magnetic field between two single-crystal cylinders of tin increased upon cooling through the superconducting transition temperature, even with no applied current. This effect of expulsion of magnetic flux from the interior of a superconductor i.e. perfect diamagnetism was dubbed the 'Meissner Effect'.

These two characteristics - perfect conductivity, and perfect diamagnetism - are now the two fundamental characteristics of a superconducting material, and immediately stimulated the imagination of many physicists and engineers with the seemingly boundless possibility of useful application.

Fast forward to now - the introduction of iron-based superconductors as the newest family of high-temperature superconductors only a decade ago [1] ensure that the study of superconductivity continues to inspire and confound. Materials containing iron, once thought of as antithetical to the existence of superconductivity, provide significant promise for superconducting applications. Significantly easier to manufacture into tapes and wires than the cuprate superconductors - the current gold standard in superconductivity - a myriad papers have been published trying to get to the bottom of how they work, why they work, and what we can do with them.

Iron-based superconductors occupy an important place in the realm of superconducting research, providing a new playground, for experimentalists and theorists alike, to interrogate what it means to be a superconductor. Iron-based superconductors fit unambiguously under the umbrella of 'un-

conventional superconductivity' with much to be uncovered in terms of what mechanism is responsible, what sort of transition temperatures can be achieved, and how much current they can drive. The fact that they are able to exist, and operate, in huge external magnetic fields is another one of their properties which makes them extremely attractive.

One particular avenue of research which has yet to be fully explored in iron-based superconductivity is how the application of external pressures can affect their superconducting properties. The significance of applied pressure has been demonstrated in many ways - many materials only superconduct under applied pressure, including 23 of the elemental solids, record high values of T_c have been induced in carbonaceous sulfur hydride at 287 K [2], and studies have reported increases as high as 100-fold in NaFeAs [3] induced by hydrostatic pressure.

In this thesis, we will present a study into the way in which hydrostatic pressure affects the critical current density (J_c) and superconducting transition temperatures (T_c) in one particular material - BaFe₂As₂ (Ba122). The undoped material manifests a superconducting transition at ≈ 30 K [4, 5] under applied pressures, and also (at varying values of T_c) upon doping with K on the Ba site, Co, Ni, Pd or Rh doping on the Fe site, and isovalent P doping on the As [6, 7]. This plethora of doping possibilities means there is a huge parameter space to uncover, and provides the means to isolate different contributions to the superconductivity. Thus, Ba122 is an important material to have the body of literature filled out.

To this end we will be performing magnetic measurements of J_c and T_c , on two series of crystals: Ba(Fe_{1-x}Ni_x)₂As₂ and BaFe₂(As_{1-x}P_x)₂. We have access to single crystals ranging from underdoped through to the overdoped regions of the parameter space, as well as an MPMS compatible pressure cell capable of applying pressures as high as 1.2 GPa. Measurements will

be performed in an applied field ranging up to 7 T, applied along two different sample orientations, and in temperature environments as low as 2 K.

After a brief introduction to the theories of superconductivity in Chapter 2, and an outline of the experimental methods in Chapter 3, we will explore three chapters of experimental results. Chapter 4 is primarily focused on the effect of applying hydrostatic pressure to $\text{BaFe}_2(\text{As}_{1-x}\text{P}_x)_2$ single crystals. This chapter provides insight into some of the unexpected effects of applying hydrostatic pressure to Ba122, uncovering a non-linear dependence of T_c on pressure which is important for future pressure dependent measurements.

Chapter 4 is focused on the doping dependence of superconductivity in $\text{Ba}(\text{Fe}_{1-x}\text{Ni}_x)_2\text{As}_2$ single crystals. This avenue of research highlights the importance of field orientation for magnetic J_c measurements, and provides a baseline for the parameters which affect J_c in this material. Lastly, we will present pressure dependent measurements on these same $\text{Ba}(\text{Fe}_{1-x}\text{Ni}_x)_2\text{As}_2$ crystals, bringing together what we have learnt from the previous two chapters in order to interpret the often convoluted results of pressure dependent J_c measurements, and determine how effectively pressure can be used to increase J_c in Ba122.

THEORY/LITERATURE REVIEW

The study of materials science often results in measurements of quantities dependent on a great deal of interconnected parameters. In particular, for this study, the behaviour of the superconducting properties of BaFe_2As_2 can be appreciably affected by various aspects of the physical structure, electronic structure, Fermi surface topology, and immediate environment quite broadly. Therefore, it is necessary to have some introduction to existence of these factors and throughout this section I will attempt to review a range of ideas that are potentially pertinent. The idea is not to immediately insinuate that these factors are of unequivocal importance, more that it would be unwise to ignore their existence. To this end, this theory section will be broken up as follows:

Section 2.1 is an introduction to basic superconductivity, with a focus on the two main properties we are interested in evaluating - critical current density (J_c) and superconducting transition temperature (T_c) - and touching on other superconducting properties which have the ability to affect these measurements. The existence of vortices, and their effect on our measurements of J_c is a large enough topic to warrant its own section, where we will focus on two main paradigms for the treatment of vortex pinning (strong/weak collective pinning, and the Dew-Hughes model) - Section 2.2.

This will be followed by an overview in Section 2.3 of the important characteristics of the various members of the iron-based superconductor family (FeSCs), and the way in which their normal-state magnetic and structural parameters are linked to the existence of superconductivity. This is followed

by an overview of the previous studies of pressure dependent (2.4) properties of FeSCs. In these sections we will also touch upon similarities with the cuprate superconductors, as these studies provide a skeleton road-map for the direction of future studies.

2.1 BASIC SUPERCONDUCTIVITY

The key characteristics of superconductivity (being perfect conductivity and diamagnetism) are awfully blatant, the fact that they exhibit some extreme properties makes it easy to underestimate the nuance involved, and even a macroscopic understanding of how these characteristics come to be requires some careful thought.

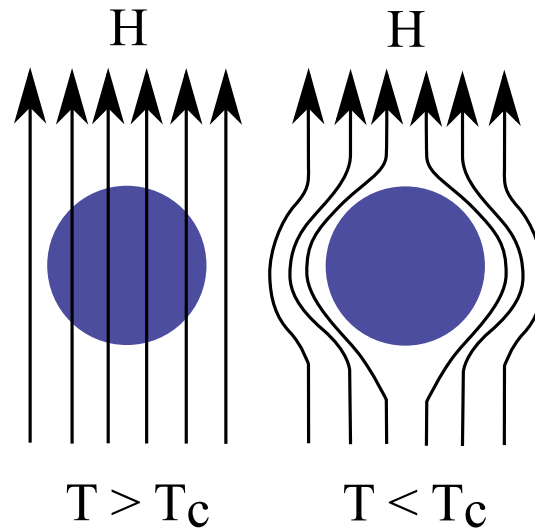


Figure 2.1: When cooled below a characteristic temperature (T_c), a superconductor will expel any field previously present in its interior. This is the Meissner effect.

First, we will describe the broad ideas that have been used to explain how superconductivity is at all possible, then we will introduce the key parameters which arise when thinking about these behaviours and finally link these parameters to the predominant theories which are used to underpin the interpretation of experimental investigations into superconductivity.

2.1.1 Penetration depth and Coherence Length

For a long time, the only clues superconductivity researchers had to go on were the known properties of zero resistance (perfect conductivity), and perfect diamagnetism i.e. complete expulsion of any applied magnetic field, illustrated in Figures 2.1 and 2.2, respectively. These behaviours become visible as a material is cooled through its superconducting transition temperature (T_c), and could resist the application of applied field only up to a critical field (H_c), often referred to as the thermodynamic critical field.

The first milestone task on the path towards a full description of these materials was a macroscopic theory to solidify the link between the perfect diamagnetism and perfect conductivity.

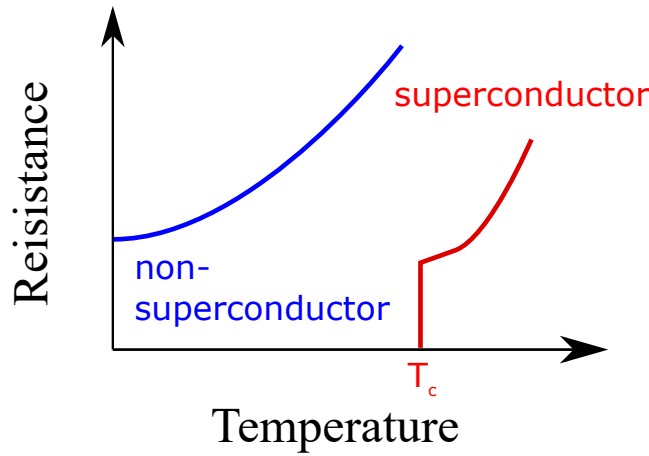


Figure 2.2: At the superconducting critical temperature, as well as exhibiting the Meissner effect, shown in Figure 2.1, a superconducting material will display a sharp drop from finite to zero resistivity.

The London brothers in 1935 successfully produced an intuitive description of how the Meissner effect manifests [8, 9], building upon the existing idea of treating the superconductor as being comprised of two fluids of super-

conducting electrons with density (n_s) and normal state electrons (n_n) with total density such that

$$n = n_n + n_s \quad (1)$$

$$\frac{n_n}{n} = \left(\frac{T}{T_c}\right)^4 \quad (2)$$

Thus, seeing as we have the superconducting electron density, we can arrive at an expression for the supercurrent density \mathbf{J} ,

$$\mathbf{J} = -ev_s n_s \quad (3)$$

by differentiating and utilising Newtons second law we arrive at;

$$\begin{aligned} \frac{\partial \mathbf{J}}{\partial t} &= \left(\frac{e^2 n_s}{m}\right) \mathbf{E} \\ &= \frac{\partial}{\partial t} (\Lambda \mathbf{J}) \end{aligned} \quad (4)$$

where $\Lambda = \frac{m}{e^2 n_s}$

Next, plugging this into Faraday's Law we find,

$$\frac{\partial}{\partial t} [c \nabla \times (\Lambda \mathbf{J}) + \mathbf{B}] = 0 \quad (5)$$

This equation rests solely on the existence of a density of conduction electrons equal to n_s .

However, the London brothers looked at restricting the set of solutions to this differential equation to only those satisfying the tighter constraint that the quantity within the square brackets equals zero. This set of solutions reproduces the Meissner effect behaviour, somewhat empirically finding a set of equations describing superconducting materials.

Thus, by solving the equation,

$$\mathbf{B} = -c\nabla \times \mathbf{A} \quad (6)$$

we arrive at the solutions for \mathbf{B} and \mathbf{J} the form;

$$\nabla^2 \mathbf{B} = \mathbf{B}/\lambda_L^2, \nabla^2 \mathbf{J} = \mathbf{J}/\lambda_L^2 \quad (7)$$

Solutions to equations of this form are well known to be an exponential decay with a decay constant of λ_L . Thus, this provides a nice picture of how a superconductor acts when placed in a magnetic field: the field penetration into the superconductor decays exponentially over a length scale λ_L , the field being screened by a current density that flows around the surface of the conductor with the same exponential decay constant as shown in Figure 2.3.

This derivation includes the introduction of the concept of a superconductors penetration depth λ_L , a parameter of fundamental importance and is given by

$$\lambda_L = \frac{mc^2}{4\pi n_s e^2} \quad (8)$$

The penetration depth is one of two characteristic lengths associated with a superconducting material, the other is the coherence length, denoted ξ ,

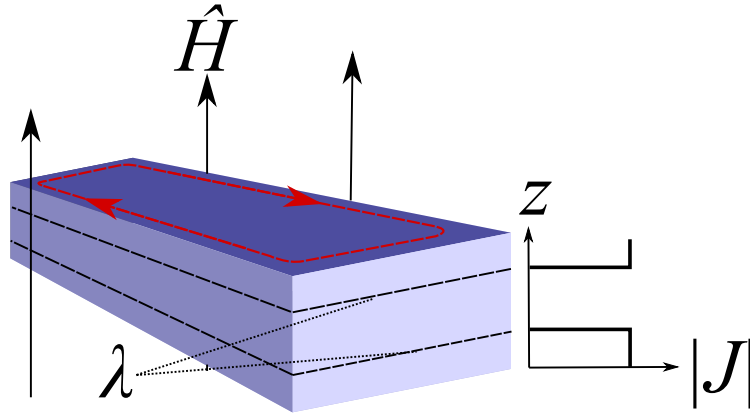


Figure 2.3: A sample material, placed in a magnetic field H , will incorporate currents only in the region within one λ of its surface, where λ is the superconducting penetration depth.

which is a measure of the decay of the superconducting carrier states wavefunction [8, 10]. The idea of ξ came about in 1953 when Pippard noticed discrepancies in the experimentally measured values of λ_L , where the values appeared to be more sensitively dependant on the amount of alloying when compared to other superconducting properties T_c and H_c .

In order to address this problem Pippard [11] utilised a non-local model where the superconducting current density is not calculated at a point but instead takes into account nearby electric fields by integrating over a volume determined by ξ . The value of ξ is sensitive to the addition of impurities into the material and is thus related to the mean free path, l , by the equation

$$\frac{1}{\xi} = \frac{1}{\xi_0} + \frac{1}{l} \quad (9)$$

where ξ_0 is the coherence length of the pure material. This equation illustrates what is referred to as the 'dirty' and 'clean' limit, in a superconducting material, terms which are commonly found when trying to compare

experimental measurements of ξ , λ_L and related properties. The dirty limit refers to a material where $l \ll \xi_0$, and thus $\xi \approx l$, whereas the clean limit is when $\xi_0 > l$ - this distinction between dirty and clean limits arises later in formulae used to approximate ξ from measurements of H_{c2} .

These two properties (λ_L and ξ), as well as being integral to defining the nature of superconductivity in a given material at a microscopic level, will also prove particularly important for us to consider because of another reason. That is, they are instrumental in describing the nature of interactions at superconducting/non-superconducting interfaces, providing us with decay constants for penetration of magnetic fields, and the superconducting wavefunctions across such interfaces. The most common situation we will encounter where this is relevant is when we begin to admit the existence of 'vortices' - normal regions which admit a single quantised flux line through the interior of the superconductor.

2.1.2 *Macroscopic parameters*

To reiterate, upon entering the Meissner state, a superconducting material will exhibit zero resistance where any current present can exist absolutely unimpeded, and perfect diamagnetism, where any and all applied magnetic field will be prevented from penetrating into the material by virtue of arbitrarily large induced screening currents. Each of these characteristics provide a method in which the transition from a normal to superconducting state can easily be observed. It can be seen through cooling a superconductor in a small applied field, measuring the macroscopic moment of the sample and observing the large jump in susceptibility associated with the Meissner effect or, of course, measuring the resistivity of the material and observing the drop to zero associated with perfect conductivity.

But what makes this transition possible? Furthermore, to what extent is it robust against the application of external fields? First and foremost is the obvious question as to how we can realise dissipation-free resistance at all. After some 50 years of theoretical and experimental work on superconductivity, the first microscopic theory of superconductivity was proposed by Bardeen, Cooper and Schrieffer (BCS) in 1956 [12].

It is clear that, in order to set up a sufficient screening current to expel the applied magnetic field, energy must be spent. This energy comes from the difference in Gibbs free energy between normal and superconducting states, an expression of which can be obtained via Ginzberg-Landau theory [10]. Equating this expression to the amount of energy stored in a magnetic field, it is found there is a maximum field that can be applied before breaking the superconducting properties of a material. This field is commonly known as the thermodynamic critical field (H_c). Thus, a magnetization (M) versus applied field (H) plot will look something like that shown in Figure 2.4. The superconducting critical current density (J_c) is simply the current that can be put through a superconductor before producing a field equal to H_c .

Unfortunately, for the sake of simplicity, everything up until this point is focused solely on what are now known as ‘type 1’ superconductors. When we extend the conversation to include the other ‘type 2’ superconductors (one example of which this current research is focused on), significantly more refinement of the details becomes necessary.

In type 2 superconductors there exists both areas of superconducting and normal state simultaneously — a mixed state in which it is energetically favourable to allow the penetration of quantised magnetic flux lines (referred to as vortices) into the material resulting in small normal cores surrounded by the superconducting bulk. The introduction of these vortices

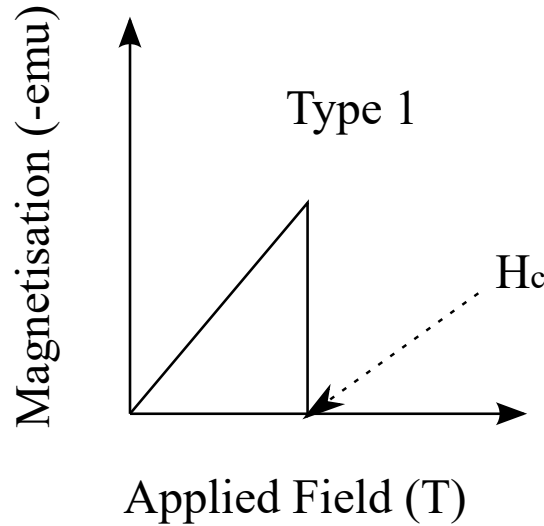


Figure 2.4: Magnetisation versus applied magnetic field behaviour for a type 1 superconductor. Magnetisation increases steadily up until the applied field $H = H_{c1}$ where superconductivity is immediately suppressed.

begins once an applied field is greater than the ‘lower critical field’ (H_{c1}) and continue to be pushed into the system until the normal cores ‘overlap’ and the entire material becomes normal at the ‘upper critical field’ (H_{c2}).

The size of these vortices, and the distance they penetrate into the material are governed by the parameters London penetration depth (λ) and coherence length of the material (ξ), respectively. Values of the Ginzberg-Landau parameter $\kappa = \frac{\lambda}{\xi}$ are used to delineate between type 1 and type 2 superconductors. This behaviour results in a M versus H plot more like the Figure 2.5.

This picture severely complicates the concept of a critical current because one consequence of the introduction of vortices is that J_c becomes significantly applied field-dependent. A simple picture of a vortex is a single electron pair circulating and screening only enough of the superconductor to allow through a single quantum of flux (see, Figure 2.6). Thus, these vortices, when placed in a magnetic field will feel a Lorentz force and begin to move. It is this movement of vortices that sets up a resistive potential

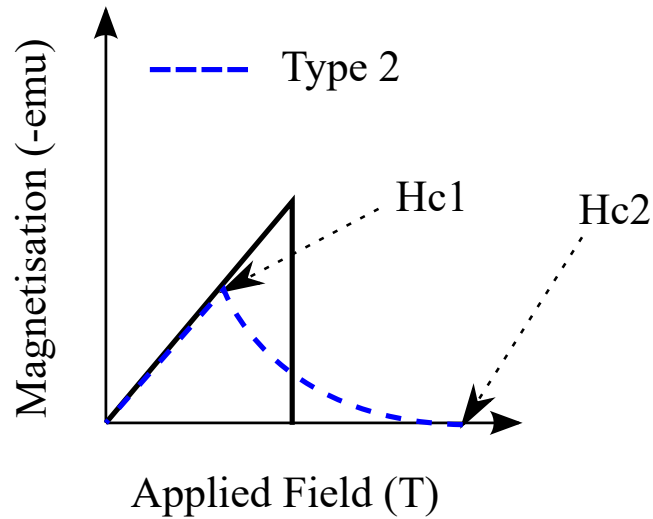


Figure 2.5: Magnetisation versus applied magnetic field behaviour for a type 2 superconductor. Unlike, type 1 superconductors, type 2 have a broad region over which dissipation is re-introduced. This 'Meissner' state begins at $H = H_{c1}$, and ends at $H = H_{c2}$ - dubbed the lower and upper critical field respectively.

within the superconductor, resulting in dissipation of energy. So, a higher field will result in more dissipation, and thus a lower J_c .

Because we are primarily interested in increasing the amount of current we can put through our superconducting materials, we need to prevent the movement of these vortices. The way of doing this is by a process called 'vortex/flux pinning' on which we will now elaborate.

2.2 VORTICES AND PINNING MODELS

In order to maximise current carrying capability for a type 2 superconducting material, it is necessary to prevent the movement of vortices which re-establishes a mechanism for the dissipation of energy from the supercurrents present. In order to have a full understanding of the many ways this effect can be achieved, researchers have attempted to articulate the mechanisms by which a vortex can become 'pinned', having been an avenue of research interest since the prediction of vortices in 1964 by A. Abrikosov

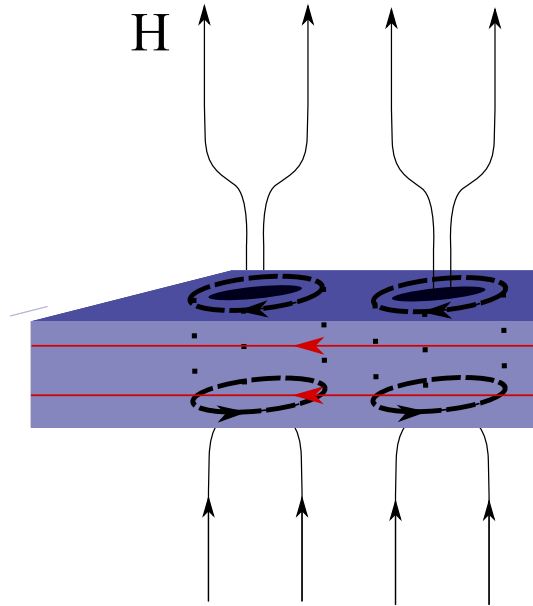


Figure 2.6: Type 2 superconductors allow the penetration of singular flux lines through the bulk of the material. These flux lines are referred to as vortices, and play an important part in determining the current carrying properties of a superconducting sample.

[13].

There are several key aspects to this problem. First of all is the problem of how to describe the behaviour of a single vortex line within the periodic potential of a physical lattice. Next, we must admit forms of inter-vortex interactions which lead to different forms of ‘vortex matter’ i.e. a vortex lattice, a vortex glass, or a vortex liquid. Simultaneously, we must consider what sort of mechanisms allow the pinning of a vortex to be energetically favourable, and what sort of inclusions/defects/features of a superconducting materials structure allow for such interactions to exist.

In the existing literature, there are a few models which have gained widespread integration into the process of characterising the types of pinning present in superconductors, particularly the works of Dew-Hughes [14], and Blatter et al. [15] which have each garnered thousands of citations. It is on these models that we will attempt to focus our energies. However, by no means

will this provide a comprehensive overview of all the theories present in the current superconducting communities body of work.

2.2.1 *Single Vortex Pinning*

A vortex can be considered analogous to an elastic string, extending through our sample along the axis in the direction of the applied magnetic field. According to the review on vortices in HTS materials by Blatter et al. [15] there are 3 classes of forces acting upon a single vortex:

- A Lorentz force due to the laminar current flow within the sample
- Microscopic scattering processes in an otherwise homogeneous system
- And, a pinning force associated with defects present in an inhomogeneous system

The Lorentz force felt by a flux-line is of the form

$$\mathbf{f}_L = \frac{\Phi}{c}(\mathbf{J} \times \mathbf{n}) \quad (10)$$

In a homogeneous system, this is balanced against a friction force, and a Hall force associated with scattering processes to arrive at an equation of motion for the vortex. However, in the present case, we are more interested in preventing the movement of vortices, and thus balance the Lorentz force against pinning forces associated with whatever form of disorder we have present in the material.

The strength of disorder is described via three dimensionless parameters. First, the parameter $j_0 = J_c/J_0$, where J_0 is an upper limit on current density derived from the force required to pull apart a Cooper pair, often referred

to as the depairing or pair-breaking current [16, 17]. This gives an intuitive measure of the strength of pinning, and describes the strength of a system's quenched disorder i.e. the depth of a potential well associated with potential pinning sites. Left to their own devices this quenched disorder can re-establish dissipation free current flow dependent on the applied magnetic field. However, this order can be overcome via thermal or quantum fluctuations, re-introducing vortex motion by virtue of thermally or quantum activated flux creep where the vortices are provided enough energy to break free of the confining potential.

The strength of thermal fluctuations are described via the parameter G_i . G_i , the Ginzburg number, is defined as measure of the relative size of the zero temperature condensation energy in a coherence volume and T_c ($G_i = [T_c/H_c^2(0)\epsilon\xi^3(0)]^2/2$), here ϵ describes the intrinsic anisotropy of the material. Fluctuations cause the oscillation of flux-lines about their equilibrium position, and if the magnitude of these oscillations reach a certain fraction of the flux-line lattice constant (defined by the Lindemann criterion [18]), we observe melting of the vortex lattice. A similar concept exists for the case of quantum fluctuation, with the key parameter being designated Q_u , or the quantum resistance. Because quantum process involve complex time dependencies the definition of Q_u differs, dependent on the nature of the system's dynamics (damped, overdamped etc.) [15, 19].

For a single straight vortex in an environment of random pinning centres, the individual forces will compete with one another. Consequently, for a vortex segment of length L , and pin density of n then the total pinning force is given by [15, 20]

$$F_{\text{pin}}(L) \approx (f_{\text{pin}}^2 n \xi^2 L)^{1/2} \quad (11)$$

where f_{pin} is the average pinning force of a single pinning centre.

The key observation in this situation is that F_{pin} scales as \sqrt{L} , whereas the Lorentz force felt by the vortex scales linearly in L . This means that a rigid vortex will not be able to scale to arrive at a situation where F_{pin} will be large enough to prevent it being overcome by the Lorentz force. Thus, it is absolutely necessary to consider the ability of a vortex to undergo physical deformations, in order to re-orient itself to achieve a non-random summation of pinning forces.

Within the single vortex regime we can further bifurcate into two significant subregimes: *weak-collective pinning*, and *strong pinning*. The distinction between these two regimes relies on the magnitude of the pinning energy (u_p) associated with each individual pinning centre. In weak-collective pinning, deformations caused by the flux-line-pin interaction induces only elastic deformations of the vortex whereas if pinning centres present in the material have the ability to deform vortex lines on the order of a , the lattice constant of the unperturbed vortex lattice, then we begin to introduce plastic deformations of the vortex lines. This definition leads to a condition on strong versus weak pinning centres based on the curvature of the flux line referred to as the Labusch criterion [21, 22].

2.2.2 *Weak-collective Pinning*

So, in weak-collective pinning, we admit a situation where pinning centres only induce elastic deformations. This results in a picture where segments of length L_c , referred to as the Larkin length, pin individually from one another, with the length determined by balancing the elastic force created by its distance from the equilibrium position of the vortex, and the pinning force on that segment. A well-known expression for this quantity is found by doing exactly that [20]; finding the differences in the pinning energy and

elastic energy:

$$\delta E(L) = \epsilon_1 \delta \frac{r_p^2}{L} - \sqrt{n_p L r_p^2 u_p} \quad (12)$$

and minimising with respect to L :

$$L_c \approx \left(\frac{\epsilon_1 r_p}{\sqrt{n_p u_p}} \right)^{2/3} \quad (13)$$

where r_p is the transverse displacement of the length L i.e. the ‘range’ of the pinning centre, n_p is the density of pins, u_p is the typical pinning energy. ϵ_1 is the line energy of the vortex.

Once we have an expression for L_c we can obtain one for J_c by equating the Lorentz force per unit length to the pinning force ($\sqrt{n_p L r_p^2 u_p}/r_p$) acting on a volume $L r_p^2$ per unit length (L) when $L = L_c$, i.e.

$$\begin{aligned} \frac{\Phi_0}{c} J_c &= \frac{\sqrt{n_p L_c r_p^2 u_p}}{r_p L_c} \\ &= \frac{\sqrt{n_p u_p}}{L_c} \end{aligned} \quad (14)$$

Because we are working in the regime of a single vortex, this result is irrespective of the applied magnetic field - J_c is proportional only to the pinning energy of each site, and the density of pins.

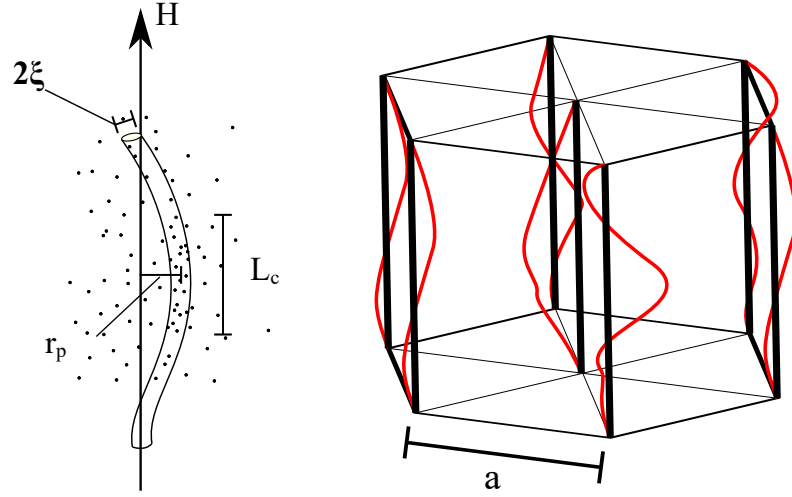


Figure 2.7: Collective pinning of a single vortex (left) by many weak, point-like pinning centres. Minimising the energy difference in the pinning and elastic forces leads to sections of length L_c (Larkin lengths) being pinned individually of one another by fluctuations in the pin density. For larger fields (right) more pinning sites are occupied and intervortex interactions become important. As long as the fluctuations about equilibrium remain less than a , we still remain in the elastic, weak pinning regime.

Once we are no longer in the single vortex regime, it is necessary to begin considering ‘vortex bundles’, with a transverse trapping area of short range order of the vortex lattice. This transverse area is often referred to as R_c , and is always larger than a . Introducing this notion of the trapping volume also reintroduces a dependence on the local flux density, B , due to the trapping volume being unequivocally linked to the shear and tilt moduli of the vortex lattice which are proportional to B and B^2 respectively. These two regimes of weak pinning are illustrated in Figure 2.7.

The same procedure as for the single vortex is presented in reference [20], and produces the result:

$$J_c \propto \begin{cases} \exp(-B^{3/2}/n_p) & \lambda > R_c \\ 1/B^3 & \lambda < R_c \end{cases}$$

2.2.3 Strong Pinning

If pinning centres are strong enough to induce plastic deformations, the situation changes slightly. A pinning centre has the ability to keep a section L of the vortex pinned, and instead of obtaining L by equating elastic and Lorentz forces, the length it pins is determined by the nature of the vortex-pin interaction and the line tension of the vortex. At slightly higher fields, the interaction between vortices also becomes an interaction which must be taken into account. If the individual pin requires a force f_p to break, then

$$\frac{\Phi_0}{c} J_c \approx \frac{f_p}{L} \quad (15)$$

For a single vortex, there are two relations used to estimate the trapped length. First, the longitudinal trapping distance u_l , in the direction of vortex motion, is known via the pin-breaking criteria, i.e. by comparing the force exerted by the pin on a segment of length L with the restoring force defined by the line tension exerted for a displacement u_l .

$$\epsilon_1 u_l = f_p L \quad (16)$$

and further, by insisting that we consider the length L to be only pinned by one site:

$$n_p L u_l u_t = 1 \quad (17)$$

where u_t is the trapping distance transverse to the vortex motion.

In reality, these trapping distances are defined by the nature of the pin-vortex interaction. If the interaction requires the vortex to collide with the

pin in order to be captured then we estimate u_t to simply be the size of the pin in that dimension. Interactions which can act over a distance, such as those present with pins associated with magnetic inclusions require more treatment.

From these two equations, in the case of a direct collision, we can approximate $u_t = b$, where b is the size of the pin in the direction transverse to vortex motion. Then, by utilising equations 16 and 17, we can obtain an expression for L and substitute into equation 15 for J_c :

$$J_c \propto f_p^{3/2} \sqrt{\frac{n_p b}{\epsilon_1}} \quad (18)$$

Again, extending this type of treatment to higher fields, involves the introduction of the shear moduli of the vortex line. The interactions between vortices contribute to a significantly more complex form for the determination of u_l . But for a direct collision, the restoring force is given by $\bar{C}u_l$ where,

$$\bar{C} \approx \frac{5}{4} \sqrt{\frac{\Phi_0}{4\pi B \epsilon_0 \epsilon_1}} \quad (19)$$

if we generalise equation 15 to include the possibility of including multiple pins in the trapping volume, and equate the restoring force $u_l \bar{C}$ with the pin breaking force as a criteria for J_c then we find:

$$J_c \approx \frac{c f_p^2 n_p b}{\Phi_0 \bar{C}} \quad (20)$$

where we know \bar{C} is proportional to $1/\sqrt{B}$.

When considering the possibility that we have pin-vortex interactions which can act at a distance, the result from reference [23] shows that this dependence should be expected to be proportional to $B^{-5/8}$ instead.

It is important to note, that in the strong pinning regime, extending to slightly higher fields is not the same as treating vortex bundles as was done for the weak collective pinning. Thus, the results of equation 20 are not insisting on being outside of the single vortex regime, i.e. involving a trapping distance larger than the inter-vortex distance, but simply taking into account the competition between vortices to attach to pinning sites.

From these theories, we have obtained expressions for J_c with a specific dependence on the magnetic field. Thus, when we are performing magnetic measurements of J_c , the observed behaviour of J_c versus H should provide us with some insight into both the nature of the pinning sites present, and the density of pins available in a certain range of fields.

2.2.4 Dew-Hughes Theory

Next, we will briefly describe the model of Dew-Hughes, who takes a very simplified approach to describe measurable differences in types of pinning. The Dew-Hughes model begins by considering only the amount of work done to move a vortex from a pinned to a non-pinned position. This has the advantage of being the foundation of a theory which does not need to introduce the concept of flux line elasticity. Thus, the Dew-Hughes model can be utilised to infer results about the geometry of a pinning landscape, but is unable to resolve the different behaviours expected for changes in the state of the flux lattice itself.

In this theory there are two ways in which a vortex can be energetically favoured to lie on a pinning site; by virtue of what are referred to as the

magnetic interaction, and the core interaction. Which of these interactions proves dominant for a given pinning landscape is dependent on the spacing between centers, as illustrated in Figure 2.8.

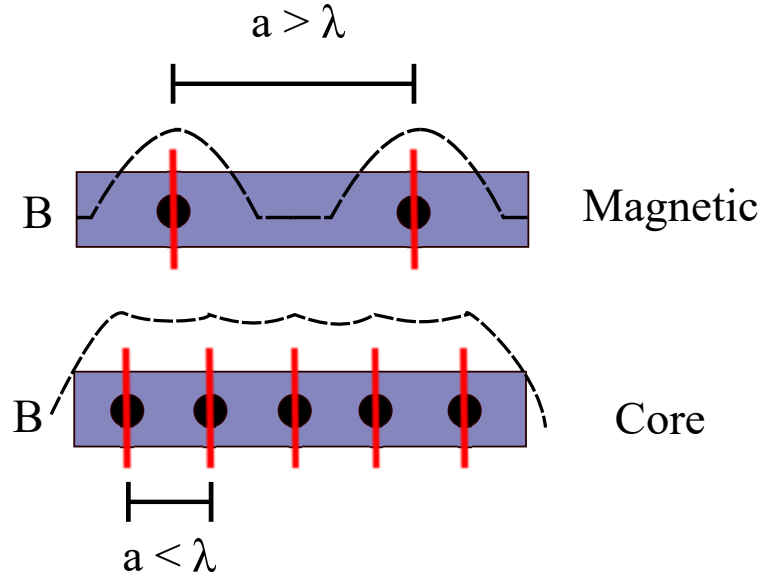


Figure 2.8: Dew-Hughes distinguishes between two pinning mechanisms, dependent on the spacing between pinning centres. If $\lambda < a$ (top) then local induction B differs between pinning sites and superconducting bulk, causing pinning via Bean-Livingston barriers. If $\lambda > a$, B attains an mean value, and pinning is caused by the difference in condensation energy between pinning sites and the superconducting bulk (bottom).

When pinning centres are adequately spaced apart (further than a few penetration depths), magnetic induction is afforded the space to reach an equilibrium value, resulting in a spatially modulating B and a Bean-Livingstone barrier to flux motion at the interface between the pin and surrounding lattice. This is the magnetic interaction. When pinning centres are more tightly packed, magnetic induction is forced to assume an appropriate mean value and, consequently, the difference in condensation energy between flux lines in the superconducting bulk and on the pinning centres prevents flow. This is the core interaction.

Type of interaction	Geometry of pin	Type of centre	Position of maxima
Magnetic	Volume	Normal	$h = 0.33$
		$\Delta\kappa$	$h = 0.17, 1$
Core	Volume	Normal	–
		$\Delta\kappa$	$h = 0.5$
	Surface	Normal	$h = 0.2$
		$\Delta\kappa$	$h = 0.6$
	Point	Normal	$h = 0.33$
		$\Delta\kappa$	$h = 0.67$

Table 1: Table showing the positions of $h=H/H_{irr}$ expected from Dew-Hughes theory [14]. Pins are divided into different types depending on the geometry, pinning mechanism (core or magnetic) and type of pinning centre (normal or $\Delta\kappa$). ‘Normal’ refers to a non-superconducting inclusion, whereas $\Delta\kappa$ refers to a region with a difference in the Ginzberg-Landau parameter κ .

This model leads to a scaling behaviour of the quantity pinning force per unit volume ($F_p = J_c \times H$). Dew-Hughes reasons this quantity to be expressed as follows:

$$F_p = \frac{\eta L \Delta W}{\chi} \quad (21)$$

Where L is the total length of a flux line, ΔW is the work needed to move a unit length of flux line from a pinning centre to its closest, non-pinned position, χ is the range of the pinning interaction and η is an efficiency factor related to the strength of interactions between flux-lines. Considerations of the nature of the pinning interaction and the dimension of the pinning centre result in a table of expected behaviours of pinning force density as a function of $h = H/H_{irr}$ [14]:

Thus, this theory provides a relatively straight forward way to experimentally characterise the type of pinning present in a material.

2.2.5 δT_c and δl pinning

Griessen et al. [24] have also provided an oft-utilised model to illuminate the nature of pinning centres in type 2 superconductors. According to their 1994 paper, building upon the work of Blatter et al. they obtained expressions for normalised J_c as a function of reduced temperature ($t = T/T_c$) which distinguish two basic classifications of pinning centres.

Griessen proposed that the nature of pins could be divided into those which result from local variation in the T_c (δT_c) or in the mean free path (δl) of a material. An important distinction to make between these two types of pinning is that the defects in δT_c pinning cause pair-breaking scattering whereas δl defects do not [20]. Thus, disorder caused by these distinct processes have different dependencies on the coherence length (i.e. size of vortices) leading to two distinct equations for J_c .

2.3 IRON-BASED SUPERCONDUCTORS

Now we will move on to a review of the relevant superconducting and normal state properties of FeSCs, in order to provide context for the measurements in this study which are performed on the specific material BaFe_2As_2 (Ba122).

Iron-based superconductors were discovered in 2008, as a result of work by Kamihara et al. [1], and have garnered a huge amount of attention since. This attention is owing in no small part to the desire of the community to coalesce their existence and theoretical underpinnings with those of the cuprate superconductors [25, 26], discovered in 1986 [27]. The discovery of FeSCs promised to be a significant boon to the study of unconventional superconductivity, i.e. superconductors which do not fit into the traditional

BCS framework, as they provide a direct avenue to interrogate the theories of superconducting cuprates, and define which of the properties of superconductors discovered up until this point are sufficient, and which are necessary.

2.3.1 *Structure*

There has been a huge number of different FeSCs uncovered, each of which can generally be sorted into different groups based on their chemical stoichiometry. For example, LaFeAsO is a member of what is referred to as the 1111 family. Other often cited groups are the 11 (FeSe, FeTe), 111 (NaFeAs, LiFeAs) and 122 (AFe₂As₂), where A = Ba, Sr, Eu, etc.), although there do exist more exotic structures. Each of these groups have a similar layered structure where FeAs or FeSe planes (analogous to CuO planes in cuprate superconductors), are separated with various spacer molecules. Figure 2.9 shows representative examples of each main structure family.

As a subset of the FeSCs, the 122 structural family has attracted a great deal of attention in a research capacity. This is largely due to their high upper critical fields (H_{c2}), low anisotropy (γ), and relatively high J_c at high magnetic fields making the 122 family a promising candidate for industrial, high magnetic field application [28–33]. A number of properties also promise applicability in a research environment: the relative ease with which we are able to fabricate high quality large single crystals using a self-flux method [34], and the rich array of substitution possibilities [35] (including hole doping, electron doping, and isovalent substitution) provides versatility in the choice of chemical tuning parameters and thus, scope for more intricate probing of the nature of superconducting properties in these materials.

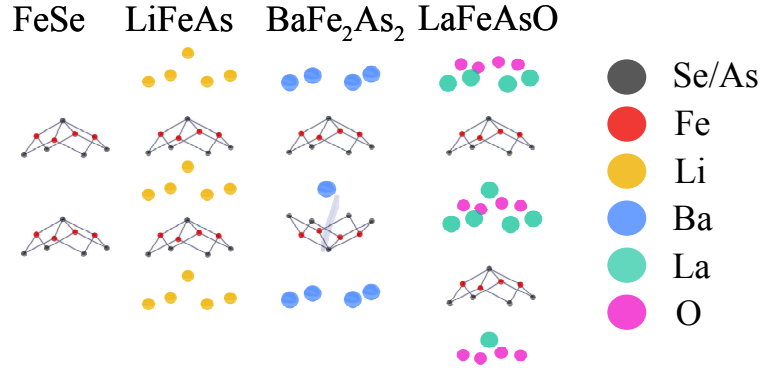


Figure 2.9: All of the various FeSC structures are comprised of FeAs (or FeSe/FeTe) planes with different amounts of 'spacer' layers in between. This is closely analogous to the cuprate family of superconductors with their common CuO planes.

Each structure family of FeSCs have garnered studies on samples of single crystal, polycrystalline, and wire/tape forms, and each of these types of sample display unique advantages, disadvantages, and peculiarities. For the purpose of our studies we are confining ourselves to single crystal samples unless otherwise stated.

There are several avenues of study which have point to structural parameters being important for the determination of superconducting properties. For example, early on, it was noticed that the T_c of representative examples of each structure family scaled with c-axis length [35] - FeSe_{1-y} ($T_c=8$ K, 5.49 Å) [36], LiFeAs ($T_c = 18$ K, 6.36 Å) [37], Ba_{0.6}K_{0.4}Fe₂As₂ ($T_c = 38$ K, 6.65 Å) [38], SmFeAsO_{1-x}F_x ($T_c = 55$ K, 8.44 Å) [39] - leading to attempts at increasing T_c via introduction of larger spacer layers.

Numerous studies on the cuprate superconductors have found that an increase in critical temperature is linked to increasing the inter-planar distance (or c-axis lattice parameter), and decreasing the area of the CuO planes [40]. This leads to the reasonable intuition that there is a significant, and reliable connection between the value of T_c and the ratio c/a , as proposed in reference [41]. Reference [42] used strain dependent mea-

surements of T_c to elucidate a similar behaviour in P-doped Ba122, however these measurements were only done up to values of approximately 20 MPa.

Thus, it is reasonably taken for granted that the measurement of superconducting properties, T_c in particular, has an immediate interpretation in terms of the structural parameters and makeup of the material itself. However, it is far from clear as to whether it is in fact, the lattice parameters themselves that are the determining factor or whether it is some particular ratio related to a different physical parameter. For example, perhaps more fundamental than the value of c/a is the electronic of the Fe site in these materials. The nearest neighbour distance in these compounds is short, generally less than 3.0 Å, ensuring that the Fe 3d electrons dominate the DOS at the Fermi energy and, thus, the character of the Fe-3d electrons, and consequently the structure of the Fe-As planes, is of significant consequence.

The Fe-As bond angles and lengths have immediate flow on effects for the magnetic moment of the Fe electrons and the symmetry of electrons participating in the pairing. Reports [43] show that the effect of hybridisation of As 4p and Fe 3d electrons results in a lifting of the d_{xy} - d_{yx} degeneracy of the Fe 3d orbitals and can alter the ground state energy enough to induce a structural transition [43]. Even more fundamental is that this hybridisation means the Fe magnetic moment is immediately dependent on Fe-As bond length [44, 45], providing a direct means to affect the magnetic ordering, and magnetic quasi-particles which may be responsible for the superconducting transition in the first place.

Thus, these structural parameters, which have been experimentally demonstrated to be directly affected by hole [38], electron [46], and isovalent doping [47] as well as applied hydrostatic [48] pressure in the Ba122 family. Thus, these are interesting markers to keep track of when detailing changes in the superconducting properties. For example, it was found that for a

large range of FeSC materials taken from the 1111 and 122 families, that T_c found a peak centered at $\alpha = 109.47^\circ$ [49], (where α is the Fe-As-Fe bond angle) and peaked at a consistent value of the anion height in the Fe-As planes [50]. Indicating that the interaction between Fe and As atoms are important for the mediation of superconductivity in this material.

To make matters slightly more complicated, results of pressure based measurements of iron-based superconductors have been shown to be very dependent on the pressure medium used [40, 51, 52]. This highlights the pivotal role of understanding the way in which structural parameters are being affected when applying hydrostatic pressure in particular, as the hydrostatic limits of a given fluid can be reached at varying pressures, and the strains induced even when confidently applying hydrostatic pressure are not trivial due to the anisotropic elastic moduli of many iron based superconductors.

2.3.2 *Higher temperature transitions*

To complicate this picture even further, all the iron-based superconductors exhibit higher temperature magnetic and structural transitions which are eagerly dependent on the lattice parameters. The family of FeSCs exist in a tetragonal structure and almost all undergo a tetragonal to orthorhombic structural transition at $T = T_S$. In undoped, and unstrained, parent compounds, the value of T_S usually lies in the range of 155 K for LaFeAsO to 140 K in BaFe₂As₂ and is readily suppressed by hole, electron, or isovalent doping as well as external applied pressures.

This structural distortion is sometimes followed by a transition to a collapsed tetragonal phases under large pressures (e.g. 17 GPa in undoped Ba122 and always accompanied by a transition from paramagnetic to anti-

ferromagnetic order at the Neel temperature (T_N). This AFM order is also pushed to lower temperatures with applied pressure and doping. However, whilst these transitions usually occur at the same temperature in the parent compound, some materials show a separation of the transitions as they move to lower temperatures. The degree to which these transitions occur at the same time affects the strength/behaviour of any magneto-elastic coupling.

In particular regard to the Ba_{122} , each of these features are well exemplified. The parent compound, BaFe_2As_2 exhibits paramagnetic to antiferromagnetic and tetragonal I_4/mmm to orthorhombic $Fmmm$ transitions [6, 53] at 140 K, which are shown to be suppressed by doping on the Fe, As, and Ba sites, application of hydrostatic pressures, or the introduction of an applied magnetic field [6, 35]. In doped Ba_{122} [54], the two transitions have been shown to separate under each of these operations, a phenomena possibly linked to the establishment of a intermediary nematic order parameter. Neutron diffraction studies have indicated a suppression of the magnetic order parameter and the orthorhombic structure below T_c , revealing both the possibility to coexist and compete with superconducting order.

One particular feature related to the existence of these transitions that we find important is the presence of a magneto-elastic coupling. Studies of this coupling, which include exploration both through theoretical DFT and experimental means, establishes not only that the magnetic and structural normal state properties of the iron pnictides can not be treated as separate phenomena, but also that the strength of this coupling is dependent on dopant, doping levels [54], and applied external pressure [55]. For example, it has been demonstrated that the structural and magnetic transitions remain coincident when K doping on the Ba site, P doping on the As site and Ru doping on the Fe site of the BaFe_2As_2 parent compound whereas doping with Co, Ni, Rh, Pt, or Pd results in a separation of the two transi-

tion temperatures [54].

Another feature of intrigue is the fact that the superconducting dome appears to be centered around the point on the doping axis of their phase diagram where these transitions appear to be pushed to 0 K. This behaviour is not unique to FeSCs - it has been seen with a number of materials, particularly those exhibiting non-Fermi liquid behaviours. For example, cuprate superconductors with the normal state pseudogap playing the analogue of AFM/structural transitions [56] and heavy fermion superconductors under applied pressure [57], both present similar features in their phase diagrams. The temptation to associate this phenomena with quantum critical fluctuations being responsible for the unconventional superconductivity is great, and there has been plenty of research attempting to uncover thermodynamic critical behaviour in order to lend credibility to this avenue.

2.3.3 *Quantum Critical Points*

To briefly elaborate on the point above, a quantum critical point (QCP) represents a phase transition occurring within a material at 0 K, see Figure 2.10, during which the state of the system is determined not by thermal fluctuations in the material, but a disordered motion driven by Heisenberg's uncertainty principle [58]. A large amount of intrigue has followed the idea of QCPs in superconducting materials as a result of its potential for providing a mechanism to mediate the existence of superconductivity in unconventional superconductors [7, 59].

In the $\text{Ba}(\text{Fe}_{1-x}\text{Ni}_x)_2\text{As}_2$ system, the doping levels $x=0.05$ and 0.07 have been shown, by virtue of NMR measurements [61], to correspond to the existence of two critical points potentially associated with significant quantum fluctuations. In similar materials, a QCP has been shown to be related to seemingly anomalous behaviour of physical properties, such as the diver-

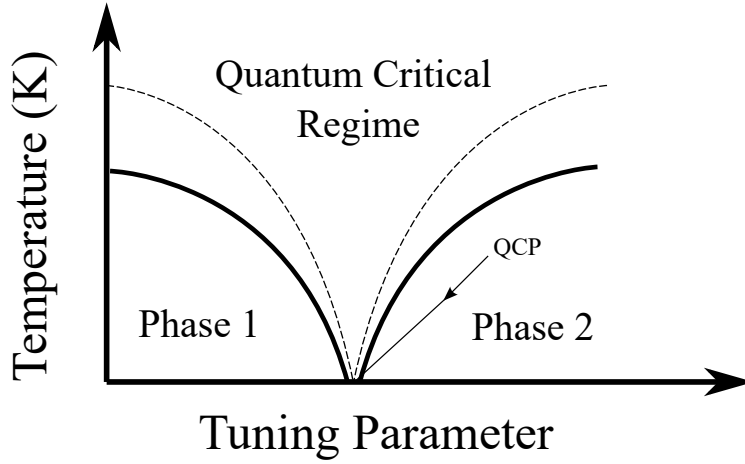


Figure 2.10: Quantum critical/non-Fermi liquid behaviours are found in the parameter space emanating from the point of transition between two phases at 0 K. The point is referred to as the quantum critical point (QCP). QCPs are believed to exist under the superconducting dome of some unconventional superconductors including $\text{BaFe}_2(\text{As}_{1-x}\text{P}_x)_2$ [60] and $\text{Ba}(\text{Fe}_{1-x}\text{Ni}_x)_2\text{As}_2$ [61].

gent effective mass [62], London penetration depth [63] and lower critical field [60] in $\text{BaFe}_2(\text{As}_{1-x}\text{P}_x)_2$. Therefore, the variation of any or all tuning parameters (doping, pressure, and magnetic field) provides an interesting and broad avenue for research into the nature of unconventional superconductivity.

There are a number of behaviours considered to be signatures of quantum critical superconductors. At an optimal value of a given tuning parameter (doping fraction, pressure etc.) both electrical resistivity (ρ) and the electronic specific heat coefficient ($\gamma = C/T$) have been found to disobey the predicted behaviour for Landau-Fermi liquids [64]. In particular, ρ does not obey the standard T^2 -dependence, whereas γ tends to diverge instead of saturate with decreasing temperatures. In heavy-fermion superconductors, and some FeSCs these behaviours are related to the existence of a QCP hidden inside the SC dome at this critical doping. Thus, these are some of the behaviours we will be keeping an eye out for during the process of characterising this material over the course of my studies.

So, we can see that there a great deal of different characteristics of FeSCs which need to be taken into account when we are attempting to study superconducting parameters. To quickly recap we have briefly covered the effect of antiferromagnetic and structural transitions, the possibility of QCPs, the existence of doping incurred pinning sites, different forms of doping (hole, electron, and isovalent), and changes to the Fermi surface, DOS of the Fe 3d orbitals, and Fe local magnetic moment.

In order to move forward with some cohesive direction, and motivated by the fact that a large portion of the current study is centred around the effect of externally applied pressures, we will continue forward largely framing the changes we observe in terms of two distinct avenues: 1) the effect on material parameters, particularly T_c , which can be related to distortions of the structural lattice parameters c and a , and 2) changes to the pinning landscape/behaviour through the lens of observed changes in J_c .

2.4 PRESSURE STUDIES

When it comes to applied pressure studies, there are two significantly different avenues down which the field has grown: the application of hydrostatic has quantitatively different effects than uniaxial pressures. Experimentally, hydrostatic pressures provide the easiest avenue of research, once an appropriate hydrostatic fluid is found, as it does not involve precise alignment of crystal structures with the pressure application axis. However, the way in which hydrostatic pressures correspond to strains in the lattice axes themselves is non-trivial, and immediately dependent on the elastic moduli and whether or not the structure itself is amenable to shear stresses.

Application of uniaxial pressures results in significant changes to the superconducting and normal-state properties of a particular structure, and are able to be more immediately linked to changes in a particular lattice con-

stant. However, these experimental conditions are less convenient. Despite this there are a number of studies which have successfully revealed distinctive effects on the superconducting properties.

Pressure results in a dome-like behaviour of T_c in all the major FeSC families, see Figure 2.11, but they all reach a maximum T_c values at very different pressures. In fact, some examples such as $\text{SmFeAsO}_{0.85}$, NaFeAs , and $\text{NdFeAsO}_{0.6}$ clearly show maximum T_c at ambient pressure. Kimber et al. [65] demonstrate that, just as in the case for ambient pressure and varying doping levels, the pressure for maximum values in T_c relate to those resulting in a regular tetrahedron angle of 109.45° for the Fe-As bonds.

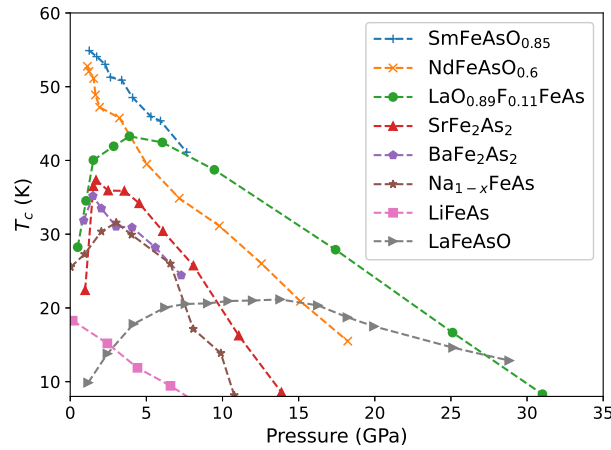


Figure 2.11: T_c vs applied pressure for a wide range of iron-based superconductors show large variation in the maximum T_c and the pressure at which this value is attained. Data for this plot was compiled in the the review 'Superconductivity in Iron Compounds' by G R Stewart [35], and includes studies from references [4, 66–71] .

2.4.1 Induced superconductivity in parent compounds

In Figure 2.11, the data of Mani et al. [4] demonstrates an onset of superconductivity in the parent compound BaFe_2As_2 around 1 GPa and a maximum value of T_c of 35 K at 1.5 GPa. However there is significant disagreement

about how much pressure is needed to induce superconductivity and reach maximum T_c in many of the FeSC representatives. The most likely source of this disagreement is simply the validity of the hydrostaticity of each study.

As is to be expected, the application of external pressures has an immediate effect on the lattice parameters of 122 superconductors. Furthermore, from previous sections, we know that this will immediately translate to a shift of the transition temperature for the magneto-structural transitions present in the parent compound. A high pressure neutron diffraction study performed by Jorgenson and Hansen [72] demonstrates that application of pressures up to 6.5 GPa results in compression of the a and c -axis lattice parameters by 2.49 and 3.66 %, respectively. Consequently, the Fe-As and Fe-Fe atomic bond lengths decrease by the same amount also. From these observations the bulk modulus B_0 was calculated as 59 GPa, which for comparison is marginally lower than that measured for CaFe_2As_2 (60 GPa) and SrFe_2As_2 (61.7 GPa), and significantly lower than that measured for a BSCCO superconductor (73 GPa) [73].

Reports of the pressure value of maximum T_c vary from $T_c, P = 29 \text{ K}, 4.5 \text{ GPa}$ [74], $31 \text{ K}, 5.5 \text{ GPa}$ to as far afield as $13 \text{ K}, 11.5 \text{ GPa}$ [75]. This is a particularly stark example of the difference hydrostaticity can make. This occurs wholly because of the susceptibility of the c -axis in particular to changes under pressure, and subsequent changes in the pnictogen height, a parameter which has been shown to have significant effects on the Fermi surface topology and density of states thus directly affecting the superconducting pairing.

2.4.2 *Effect on T_c and J_c*

During the last few years, extremely high values of T_c have been achieved by virtue of applying large pressures as high as hundreds of GPa [76]. Sig-

nificant J_c improvements in members of the 111 [3], 21311 [77] and 122 [78] FeSCs have been reported after applying comparatively low pressures around 1.2 GPa. In addition, a pressure induced change in the pinning mechanism present in superconducting MgB_2 [79] has been observed.

Pressure studies on K-doped $BaFe_2As_2$ (hole-doping) have been undertaken and found to have positive effects on J_c and T_c but, as of yet, very little in the way of J_c -pressure studies on electron doped Ba122 have been performed. Determination of asymmetry, or lack thereof, between electron and hole doped pressure dependence is an important step in revealing potential commonalities and/or differences with the well-documented cuprate behaviours [80].

2.5 RESEARCH QUESTIONS

Now, with some idea of the factors surrounding pressure studies on iron-based superconductors, we are in a place to present the questions we intend to address over the course of this thesis:

1. How do the basic superconducting properties of $Ba(Fe_{1-x}Ni_x)_2As_2$ evolve as a function of applied hydrostatic pressure. In particular, does the possibility of quantum critical behaviours around the proposed critical doping of $x = 0.050$ introduce complicating factors which can be discerned by pressure effects on T_c and/or J_c ?
2. How does the application of pressure effect the nature of pinning in $Ba(Fe_{1-x}Ni_x)_2As_2$? Do previously observed changes to pinning characteristics of other Ba122 systems translate to Ni-doping, and are they consistent over the pressure range of 0-1.2 GPa?
3. Can a comparison between isovalent doping, with P on the As site, and electron doping, with Ni on the Fe site, provide extra insight into the complex interaction of pressure with J_c and T_c in the Ba122 family?

After a description of the experimental methods, the following results chapters are laid out in an order as to provide some continuity in the logic.

First, Chapter 4 presents pressure studies on the $\text{BaFe}_2(\text{As}_{1-x}\text{P}_x)_2$ single crystals first, as they provide some immediate insight into the way pressure is translated to strains in the crystal structure and how this effects T_c in our samples.

Chapter 5 presents doping dependent measurements on the $\text{Ba}(\text{Fe}_{1-x}\text{Ni}_x)_2\text{As}_2$ single crystals, so as to establish some of the already interesting properties of this series before they are convoluted by the application of pressure. Finally, Chapter 6 presents our pressure dependent measurements on selected crystals from the same $\text{Ba}(\text{Fe}_{1-x}\text{Ni}_x)_2\text{As}_2$ series.

EXPERIMENTAL METHODS

3.1 SAMPLES

Samples of nickel doped BaFe_2As_2 were obtained for this experimental program via a collaboration with Michael A. Susner, Materials and Manufacturing Directorate, and Timothy Haugan at the Air Force Research Laboratory, Wright-Patterson Air Force Base, Ohio 45433 USA. The samples are single crystals, grown using a self-flux method described below, and characterised using EDS analysis with a Bruker solid state detector paired with a JEOL SEM. The following descriptions were provided by Michael Susner.

Samples of phosphorous doped BaFe_2As_2 were obtained for this experimental program via collaborations with Dr Yuta Mizukami and Prof. Shibauchi from University of Tokyo Japan, and Dr Shigeru Kasahara and Prof. Yuji Matsuda from Kyoto University, Japan.

3.1.1 *Self-flux Methods*

Synthesis of the single crystal materials was accomplished through a self-flux growth. $\text{Fe}_{1-y}\text{Ni}_y\text{As}$ was synthesized through reaction of pure elements in sealed quartz ampoules under vacuum at 1050°C for 24 hrs. These materials were sintered ground and placed together with Ba (molar ratio 1 Ba: 5 $\text{Fe}_{1-y}\text{Ni}_y\text{As}$) into an Al_2O_3 crucible. The ampoules were heated to 900°C over 30 hours, held for 20 hours, heated to 1195°C over 60 hours, held for 10 hours, and finally cooled to 1040°C over 78 hours. The sealed ampoules were pulled from the box furnace and centrifuged to decant the $\text{Fe}_{1-y}\text{Ni}_y\text{As}$ flux. Compositions were determined through energy disper-

sive spectroscopy (EDS) analysis of at least three discrete spots on three separate crystals.

Single crystals of $\text{BaFe}_2(\text{P}_{1-x}\text{As}_x)_2$ were grown from stoichiometric mixtures of Ba flakes, and FeAs, Fe, P, or FeP (powders) placed in an alumina crucible, and sealed in an evacuated quartz tube. It was heated up to 1150–1200 °C, kept for 12 hours, and then cooled slowly down to 800 °C at the rate of 1.5 °C/h. Platelet crystals with a shiny [001] surface were extracted, and the x values were determined by an energy dispersive x-ray analyzer.

3.1.2 *Lattice Parameter Determination*

A Bruker D8 Discover DaVinci system was used with either Cu $K\alpha$ (1.540590 Å) or Co $K\alpha$ (1.78919 Å) radiation. Low temperature measurements were performed from 70- 300 K on an Oxford Instruments Chimera system. All analysis was accomplished via LeBail fits to the c -axis reflections using the FullProf software package [81] using the widely-available BaFe_2As_2 cif file as a starting reference. Uncertainties were determined by probing 3-4 spots on each of 3-4 crystals from each batch. Standard error propagation was used to convert the range in measurement results into uncertainties on the doping of each batch.

3.1.3 *Resistive measurements*

Resistive measurements were performed on a Quantum Design Evercool® Physical Property Measurement System (PPMS) using a standard 4-point technique. Samples were mounted on cigarette paper using VGE-7031 varnish (Lakeshore Cryotronics). Copper leads were attached to the single crystal specimens using silver paint. Resistive data was taken from 2-300 K

under magnetic fields ranging from 0-9 T in both heating and cooling configurations. Heating/cooling rates were kept to 0.2 K/min, or less when going through the superconducting transition.

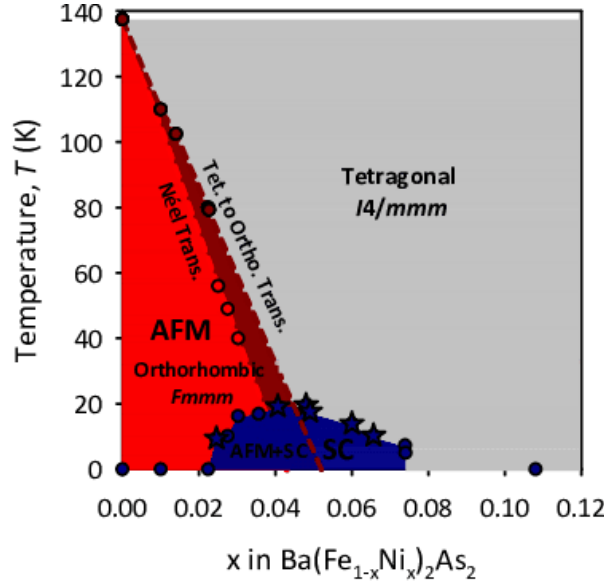


Figure 3.1: Phase diagram of the $\text{Ba}(\text{Fe}_{1-x}\text{Ni}_x)_2\text{As}_2$ system as elucidated from measurements on our single crystal specimens. T_c and T_N were taken from resistivity versus temperature measurements; structural transition temperatures were estimated from XRD measurements taken as a function of temperature (see inset). The points denoted by the star symbol denote the samples subjected to J_c investigation as the focus of this study. The linear extrapolations point to potential critical concentrations within the superconducting dome.

These measurements were used to create Figure 3.1; a doping phase diagram establishing the trends in the antiferromagnetic and structural transition temperatures (T_N and T_s , respectively). These trends, when extrapolated through the superconducting dome estimate the doping concentration of potential quantum critical points in the material and consequently, samples in the vicinity of these concentrations were chosen for further investigation of J_c .

3.2 MAGNETIC MEASUREMENTS

Further measurements to establish the superconducting properties as a function of doping and pressure from magnetic measurements provide the original experimental data for this research program.

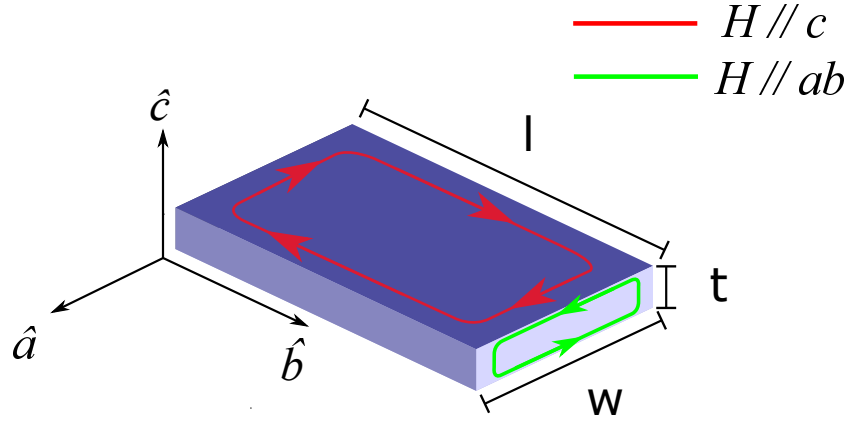


Figure 3.2: Diagram of relative orientations of a sample. Red and green lines represent the supercurrents induced by fields applied parallel to the c -axis and b -axis, respectively. This change in orientation is achieved physically in our measurements by changing the physical orientation of the sample, not the field.

Magnetic measurements were taken using a Quantum Design Magnetic Property Measurement System (MPMS) [82]. Samples measured in the MPMS were cut from the post-processed large samples into a rectangular shape with typical dimensions of $1.5 \times 1 \times 0.1$ mm and typical mass of approximately 1-2 mg for the doping dependent measurements. As shown in Figure 3.2, the c -axis is normal to the large surface of the sample, which is characterised as the ab -plane.

Each sample was placed in a gel cap, held between the side walls of each part of the cap in order to maintain an orientation parallel to the applied field. For perpendicular orientation, the same sample was placed in a PPMS VSM capsule, and allowed to lay flat. These capsules were placed in a straw, and kept in place by straw segments of equal length and shape in order to

avoid asymmetric background contributions. For pressure cell measurements, the sample needed to be cut smaller in order to fit into the 2.67-mm outer diameter Teflon capsule. Samples were cut from samples used in the doping dependent measurement series, and had a typical dimensions of $1.0 \times 0.5 \times 0.1$ mm, and a typical mass of approximately 0.5 mg.

Values for the magnetic moment associated with a sample are obtained via measuring the voltage induced in a SQUID (Superconducting QUantum Interference Device) magnetometer (illustrated in Figure 3.3), when physically moving the sample through the middle of the SQUID coils over a specified range. The MPMS has the capability to perform measurements with an applied field ranging up to 7 T, and temperatures as low as 2 K.

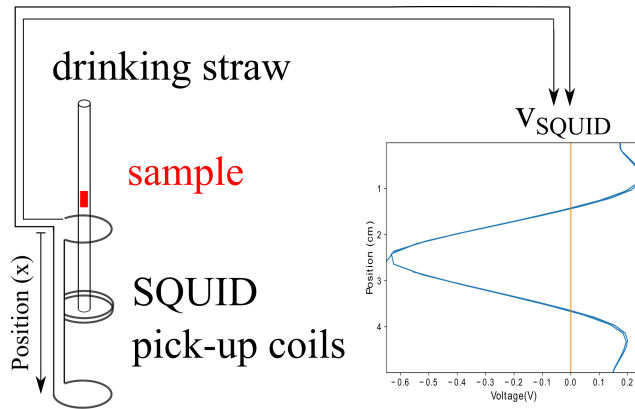


Figure 3.3: Samples are placed in a symmetric drinking straw and attached to the relevant transport system. A positional sweep through the SQUID pick up coils produces an output voltage.

The raw measured voltage is processed in two ways before being used to fit to an equation representing a perfect dipole and returning a value for the magnetic moment of the sample. Before fitting, the raw voltage is de-meaned, meaning that the average of all values over the position range is subtracted from each point. Next, in order to account for any drift in voltage induced in the SQUID, the position range is swept twice and used

to determine a linear drift in the voltage signal and subtracted. Figure 3.4 shows a representative example of the signal at the unprocessed, demeaned, and detrended stages of this process.

Figure 3.4 is the output when using the reciprocating sample option (RSO) which was used for all doping dependent investigations. Due to the weight of the MPMS compatible pressure cell, for pressure dependent measurements, the ‘standard transport’ option was used.

Once the detrended and demeaned voltages are obtained, each measurement is fit with an equation of the form [83]:

$$V(Z) = X_1 + X_2 \times Z + X_3 \left\{ 2[R^2 + (Z + X_4)^2]^{-1/2} - [R^2 + (\Lambda + (Z + X_4))^2]^{-3/2} - [R^2 + (-\Lambda + (Z + X_4))^2]^{-3/2} \right\} \quad (22)$$

Where Z is the sample position, Λ and R are geometric calibration parameters. X_1 and X_2 are the parameters associated with a vertical offset, and linear drift, respectively. These two parameters should be very small, as they have been theoretically accounted for by the signal processing. X_3 is the value used to derive a magnetic moment whereas X_4 corresponds to a vertical offset of the sample - fits will struggle to converge to an appropriate result if this value is too far from zero.

The form of equation 22 is associated with a perfect dipole located in the center of the 5 cm positional sweep range. The insistence that the sample is in the center of the positional range is dealt with via a centering procedure consisting of running the sample through a full positional sweep, and

conflating the local extrema (minima in the case of a perfect diamagnetic signal) with the sample being in the center of the SQUID magnetometer. This also minimises the value of X_4 , allowing the best possible fit.

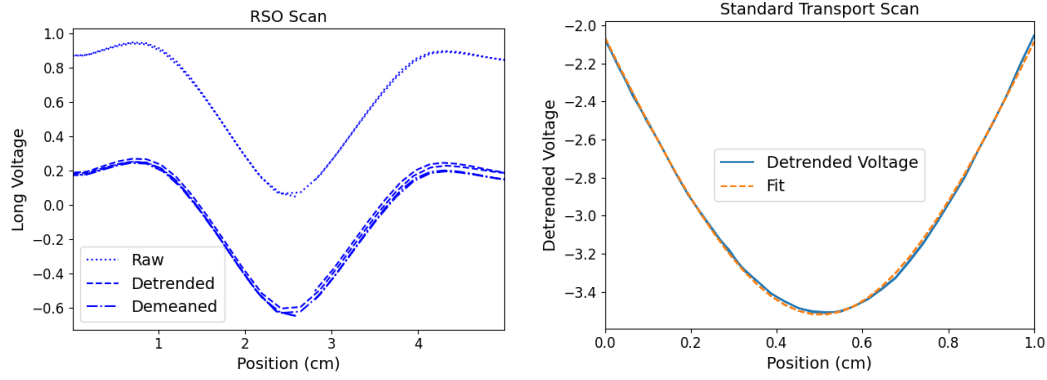


Figure 3.4: The output voltage obtained from a positional sweep of the SQUID outputs a signal from which a vertical offset, and a linear drift are compensated for (left). This signal is then fit using equation 22, with a derived parameter for the magnetic moment of the sample.

For measurements using the RSO transport option, each data point consists of 2 scans, from which a value for the magnetic moment, and a standard deviation of those values is calculated. This value of the standard deviation was calculated according to the standard definition [84]:

$$SD = \sqrt{\frac{1}{n-1} \left[\sum_{i=1}^n m_i^2 - \frac{1}{n} \left(\sum_{i=1}^n m_i \right)^2 \right]} \quad (23)$$

This value of SD provides a measure with which to identify potentially awry data points, and was used to filter out such points.

For measurements using the pressure cell set-up, the MPMS standard transport option was used. For these measurements, the sample was moved through a positional range of only 1 cm for the sake of the condition of the motor. Additionally, because of the smaller scan length, the presence of the

pressure cell and having to use smaller samples, the signal is significantly noisier. To account for this, the number of scans in each data point was doubled to 4.

3.2.1 *Zero-Field Cooled (ZFC) measurements*

In order to obtain values for the T_c and volume fraction of each of our samples, we performed a series of measurements where the sample is cooled, in zero field, to 2.0 K (significantly below T_c) and consequently placed in a small magnetic field ($H = 0.5$ mT) to have the magnetic moment of the sample tracked as it is warmed through the superconducting transition. At the lowest temperature point of this sweep, the sample is fully superconducting, and produces a large diamagnetic signal if placed in a magnetic field. This signal is what is used to center the sample in the scan length as previously discussed.

The field used for the ZFC measurements is as small as possible (0.5 mT) in order to avoid broadening the superconducting transition and thus obtaining as accurate a value for T_c as possible. In order to obtain such a small field, the magnet was degaussed using a field oscillating between ± 1 T and reset by briefly heating the magnet between each set of measurements (i.e. between swapping samples). If this was not done, residual fields would manifest in a complication of the centering signal, quite often in the form of producing a ferromagnetic, instead of diamagnetic, signal.

T_c was obtained from the ZFC curve by T_c -crossover calculations. A straight line is fit to the transition region, and extrapolated out to intersect a constant fit to the values above T_c . An example of this method is illustrated in Figure 3.5. Uncertainties in T_c measurements were obtained via calculating a standard deviation on the value of the zero line, and varying the points

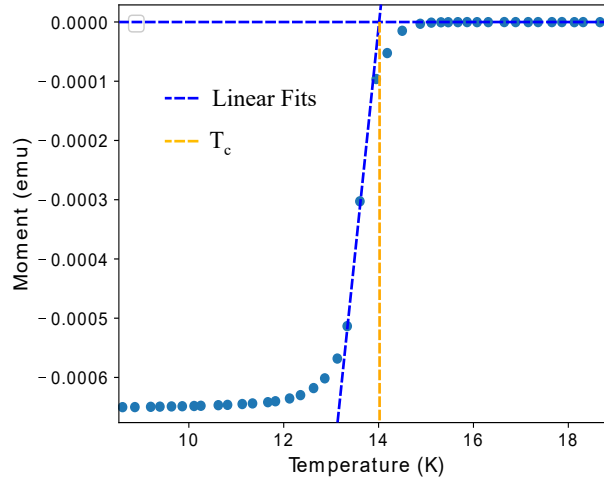


Figure 3.5: T_c was estimated by extrapolating a linear fit of the critical region to a zero line extrapolated from points above the onset of the transition.

used for the fit to the transition area, and taking the maximum deviation from the optimal fit.

3.2.2 Hysteresis Measurements and Bean Model

Measurements of J_c were obtained using magnetic hysteresis measurements and converted to values of J_c via the Bean Critical State Model. This is done by ramping the sample through a closed magnetic field loop with maximum value of 7 T obtainable in the MPMS. An example is shown below, in Figure 3.6, of the stereotypical raw data obtained from a single run of one of these hysteresis measurements.

The key assumption of the Bean model is that all current flowing in the interior of the sample flows at the critical value (J_c), that is analogous to saying that the gradient of magnetic induction B , penetrating into the interior of the sample is constant. The magnetic field at the surface interface of the sample is equal to the applied field, H , and as this is increased the field

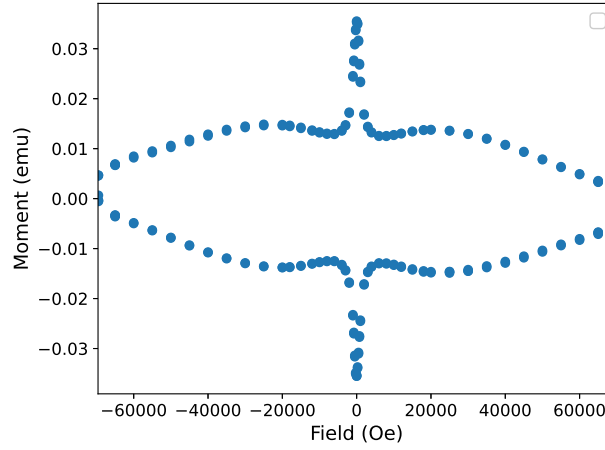


Figure 3.6: An example of a raw hysteresis loop measurement at 2 K which were undertaken to produce values of J_c versus H .

penetrates deeper into the interior of the sample.

From the Bean model we obtain an estimate for the distribution of currents within the superconducting sample, as illustrated in Figure 3.7, which demonstrates the evolution of magnetic field for the increasing field branch of a hysteresis loop.

By virtue of integrating the currents present in our sample over its dimensions we can arrive at a generic expression for the magnetic moment created by the sample at a given field. For example, in a cylinder shaped sample of radius R :

$$M = \frac{-1}{10R^2} \int_0^R J(r)r^2 dr \quad (24)$$

However, you will notice in Figure 3.7 that there is a particular field $H = H^*$ where the field penetrates fully into the middle of this sample. This corresponds to the field where we have a current induced everywhere in our sample equal to J_c . This means that any further applied field will result in

the introduction of dissipative currents into our system.

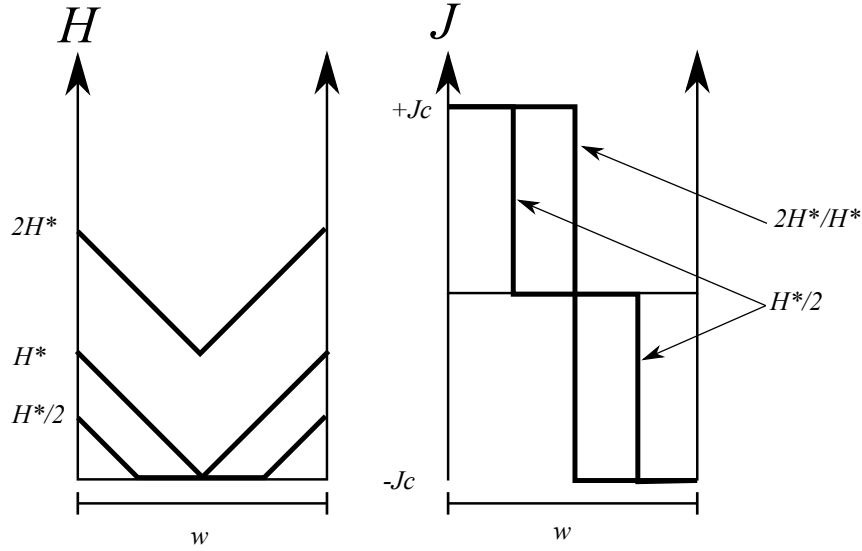


Figure 3.7: The Bean model stipulates a constant gradient of H into the interior of a sample. This means that, as H is increased, the induced supercurrents, which all flow at a value J_c , penetrate further into the interior of the sample.

Thus, at this particular point, if we were to measure the magnetic moment of our sample, assume a constant $J_c(r)$, then simply dividing by the width of this spatial dimension would give us J_c . But for points before, and after this particular H^* , we must first subtract the contribution from the dissipative currents. Thus, generically:

$$J_c(H) = A * \left(\frac{M^+(H) - M^-(H)}{R_{\text{eff}}} \right) \quad (25)$$

where R_{eff} and A are factors determined from the shape of the given sample.

In our case, we are dealing with samples in the slab geometry, and the standard result of geometry considerations leads to using equation 26 to calculate critical current densities from each measurement.

$$J_c = 20 \frac{\Delta M}{a(1 - \frac{a}{3b})} \quad (26)$$

where a and b are the width and length of the sample ($a < b$) and ΔM is the difference in volume magnetization for increasing and decreasing fields.

3.3 PRESSURE METHODS

Each sample was loaded in a 2.67-mm-diameter, 9-mm-long Teflon capsule along with Fluorinert FC70 and FC77 mixed in 1:1 ratio as a cryogenic hydrostatic pressure medium. The sample capsule was then placed in a miniature home-built nonmagnetic Be-Cu Mico Metal, 97.75 % Cu and 2 % Be piston clamp cell (dimensions of 8.8 mm diameter, 65 mm length) with cobalt-free tungsten carbide pistons, see Figure 3.8. The pistons of this cell are lightly tapered using electric-discharge machining. To apply pressure, the cell was pre-loaded before clamping at room temperature using a laboratory press with calibrated digital pressure gauge Ashcroft model 2089, 0.05 % accuracy. A more detailed description of this pressure cell can be found in reference [85].

Uncertainty the applied pressure were estimated by taking a monitoring the pressure before and after the tightening of the locking nuts. Quoted values are taken as the average of these two values.

3.3.1 Calibration

The applied pressure was calibrated by observation of reported shifts in T_c of lead at zero field [85]. Figure 3.9 shows the result of measurements

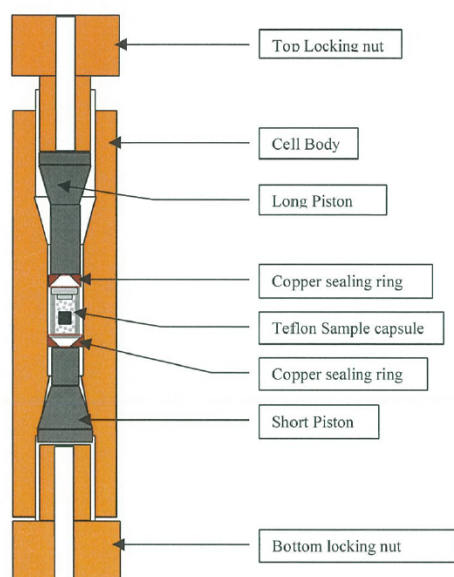


Figure 3.8: Experimental set-up for the pressure dependent measurements. samples are placed in a Teflon capsule, and pressure applied using a laboratory pressure through the top locking nut before tightening.

using the pressure cell, $\text{GPa}(T_c)$ versus nominal applied pressure. Values of T_c are converted to GPa using the results in [86], which provide verification of a linear relationship up to 5 GPa, well above the max pressure of our measurements. A linear trend is observed and provides us with the means to convert our observed values in psi to a reliable value in GPa.

Figure 3.9 shows the nominal pressure values of 1150 Psi do not maintain the linear trend. This is due to approaching either the limits of the tensile strength of the Be-Cu body of the cell, or the hydrostaticity limits of the Fluoroinert mixture pressure medium. The hydrostaticity limits are important to consider, as uniaxial pressures have been shown to induce measurably different rates of dT_c/dP when compared to that of hydrostatic pressure [51].

A study of various pressure mediums by Tatiewa et al. [87] monitored hydrostaticity via the breadth of the ruby R_1 fluorescence line as a function

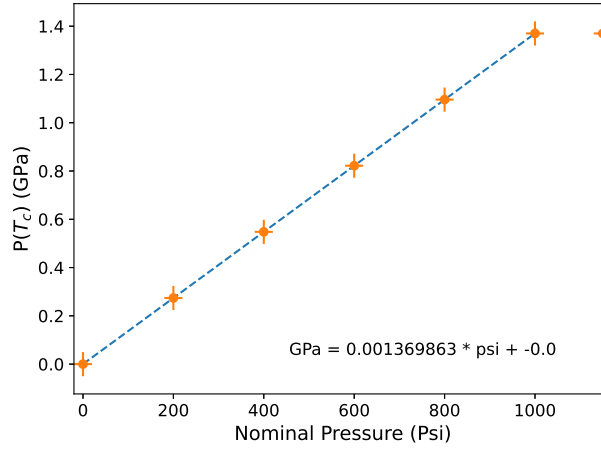


Figure 3.9: A linear trend between nominal applied pressure and the pressure associated with measured values of the T_c of a Pb sample.

of nominal applied pressures and found broadening at room temperature began at 1.2 GPa. Thus, it is likely that this final data point at nominal pressure of 1150 psi, fails to fall on the linear trend due to broadening of the superconducting transition induced by non-hydrostatic effects.

Thus, any data taken at this pressure should be considered to present effects expected of a uniaxial component of pressure. In BaFe_2As_2 this corresponds to a more sensitive dependence of the the c-axis lattice parameter, and consequently a more rapid suppression of the higher temperature transitions. This will directly affect the value of T_c , and J_c , although we have little to suggest that the pinning landscape should be affected.

3.3.2 Background Measurements

Background measurements were used to identify potential spurious contributions to the hysteresis measurements. Because we are measuring J_c magnetically, using equation 26, only sources that contribute to the hysteresis between ascending and descending field branches of the loop will result

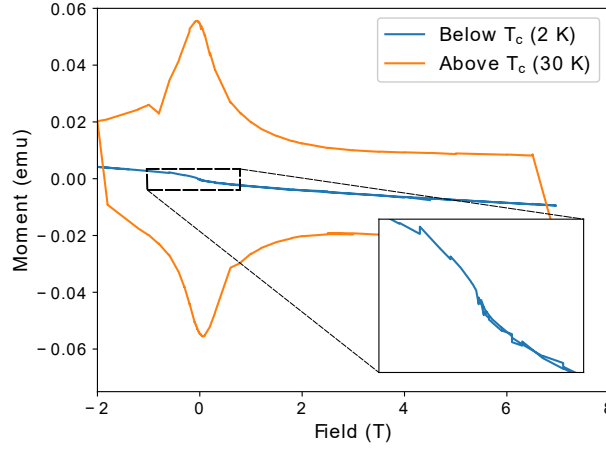


Figure 3.10: An example of a background hysteresis loop taken above T_c . This particular measurement was of the $x = 0.29$ phosphorous doped sample at 1 GPa. No hysteresis is observed, only a small diamagnetic signal associated with the copper gaskets and/or BeCu housing, leaving the J_c measurement unaffected.

in a difference to the value of J_c .

Figure 3.10 shows a representative measurement for the $x = 0.29$ $\text{BaFe}_2(\text{As}_{1-x}\text{P}_x)_2$ sample at ≈ 1 GPa. This clearly shows that the hysteresis contributing to the Bean model measurement of J_c is completely provided by the superconducting effects, even at high pressures. The background measurement displays no hysteresis, only a small diamagnetic signal attributable to the Cu and CuBe components of the pressure cell set-up.

PRESSURE EFFECTS ON ISOVALENTLY DOPED

$\text{BaFe}_2(\text{As}_{1-x}\text{P}_x)_2$

This first results chapter centres around measurements of an isovalently doped $\text{BaFe}_2(\text{As}_{1-x}\text{P}_x)_2$ series of samples, both as a function of doping and applied hydrostatic pressure. In terms of doping dependence, we have four samples with $x = 0.25, 0.29, 0.35$, and 0.38 ranging from firmly underdoped to overdoped, with optimal doping occurring at $x \approx 0.33$ [88, 89]. Following magnetic determination of the T_c and J_c characteristics as a function of doping, one sample was chosen from each region of the phase diagram (underdoped, optimally doped, and overdoped) and thus, the $x = 0.25, 0.29$, and 0.35 samples were measured again as a function of pressure, ranging from 0 to 1.2 GPa.

These pressure studies unveiled a number of interesting phenomena. A large decrease in T_c at pressures $\approx 0.2\text{-}0.4$ GPa, corresponding to percentage changes as high as 50 %, was observed in every sample, with the greatest decrease in T_c occurring for the critically doped $x = 0.29$. This initial decrease was followed by a recovery in each sample to at least the initial value of T_c , or even higher in the case of the underdoped sample.

The trend observed in the T_c behaviour dominates the corresponding measurements of J_c , resulting in significant suppression of J_c at low pressures. We posit that this behaviour can be explained as a non-linear response of the structural lattice strains to applied hydrostatic pressure.

4.1 DOPING DEPENDENT MEASUREMENTS

In this initial section, we will present the first examples of our magnetic measurements, which consist of measuring magnetisation as a function of temperature and field for samples at different phosphorous doping fractions. In the course of doing so, we will define and elaborate on some of the features of magnetisation curves that will pervade the measurements in all the subsequent chapters. First, however, we need to briefly expand upon what changes we expect to be brought about by isovalent doping with phosphorous.

We know that the isovalent doping provides no extra charge carriers to the material, meaning that isovalent doping should largely provide the effects associated with the chemical pressure induced by substituting with atoms of smaller effective radii. A previous study of the crystal structure of P-doped Ba_{122} shows a resulting reorganisation of the crystal structure [47], not solely a difference in the pnictogen height.

Thus, naively we do expect to see less effects associated with the charge doping of Ni, or Co on the iron site, such as shifting of the Fermi energy [90, 91], and introduction of pair-breaking pinning centres [25]. Instead, phosphorous doping seems more likely to favour effects associated with changes to the crystal structure, such as altering lattice parameters, and the consequent effect of changing the Fe magnetic moment. However, the lattice and electronic structures are intimately linked in 122 superconductors, and ARPES measurements have shown that the Fermi surface characteristics are significantly altered by phosphorous doping [92].

We do know that isoelectronic doping induces superconductivity in BaFe_2As_2 , with phosphorous doping resulting in maximum values around 30.0 K [88, 89]. T_c values attained by P doping are larger than those attained by elec-

tron doping on the Fe site (Co doping gives max T_c around 24 K [93], Ni - 20.5 K [94]), and less than that obtained via hole doping on the Ba site (K doping results in $T_c \approx 38$ K [38]), or by external pressure applied to the undoped parent compound ($T_c \approx 35$ K [4]).

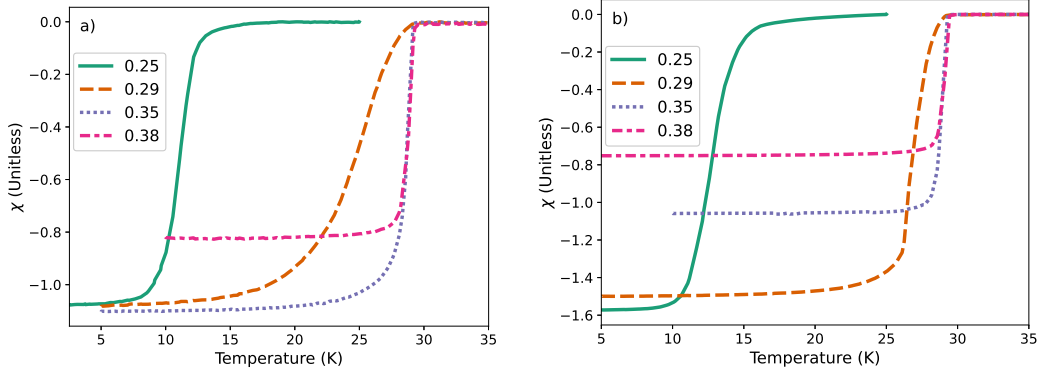


Figure 4.1: Susceptibility versus temperature for each phosphorous doped sample with field oriented parallel (a), and perpendicular (b) to the ab -plane. Curves measured with field in parallel orientation all show values $|\chi| > 0.8$ indicating reliable bulk superconductivity.

The common thread in all these observations is the importance of structural parameters in determining T_c for BaFe_2As_2 samples [35, 40]. Thus, a change to lattice parameters is immediately the most likely culprit for any behaviours we see in our subsequent results.

4.1.1 Temperature Dependent Magnetisation

Figure 4.1a shows the susceptibility (χ) versus temperature for each of the phosphorous doped samples in the parallel field orientation. These ZFC curves should theoretically have no demagnetisation effects, and show all samples reaching close to the perfect diamagnetic value of -1 corresponding to consistent bulk superconductivity. The lowest value occurs in the most overdoped sample at 0.8 - this is indicative of a reliable series of superconducting samples.

Demagnetisation

The difference in values between ZFC curves taken with field oriented parallel (4.1a) and perpendicular (4.1b) to the ab-plane of our samples is due to the effect of demagnetisation i.e. the redistribution of magnetic field density incident on our sample due to the geometry.

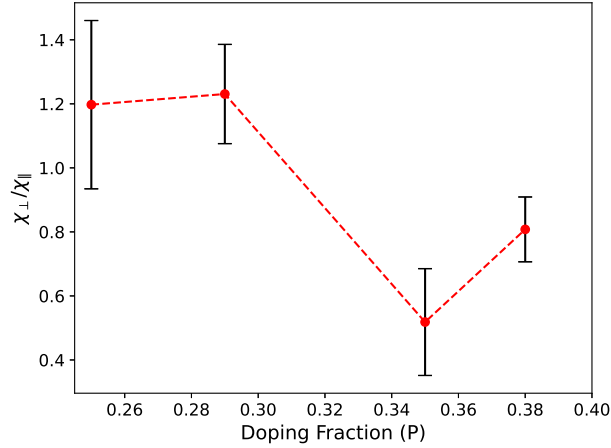


Figure 4.2: A plot of the anisotropy of magnetic susceptibility versus doping shows a distinct change as doping increases beyond the quantum critical point at $x = 0.3$. Values are taken from fits at 2 and 4 K

Demagnetisation in the parallel orientation should theoretically be negligible, whereas we expect a significant difference for perpendicular orientation. Therefore, we have corrected for this via calculations of the expected demagnetisation factor in all perpendicular measurements. We have approximated this factor via calculations presented in references [95] and [96], each based on different assumptions about the sample geometry.

There is still an intrinsic anisotropy present between the values of susceptibility after the demagnetisation correction, presented in Figure 4.2. Magnetic anisotropy has been observed in a range of superconducting materials including (but not limited to) representatives $\text{YBa}_2\text{Cu}_3\text{O}_7$, and $\text{Nd}_{2-x}\text{Ce}_x\text{CuO}_4$ from the cuprate family [97, 98], and FeSe [99], SrFe_2As_2 [100] from the

realm of iron-based superconductors.

In terms of BaFe_2As_2 superconductors, this anisotropy has been observed in the electron doped [101], hole doped [102], strained [103], and undoped [37] material. These reports vary as to whether the anisotropy is observed in or out of plane. Nevertheless, this anisotropy is related to the establishment of some orbital or spin ordering [101, 104] being established below the normal state magnetic/structural transitions, and contributing differently to susceptibility dependent on the sample orientation. In our data we can see clearly the distinct change in χ as we increase doping through the critical doping at $x = 0.3$, indicating a change in magnetic ordering.

Superconducting transition width

A feature of the ZFC curves which will be of interest throughout this thesis is the width of the superconducting transition, which we will denote as ΔT_c . The breadth of a superconducting transition is unavoidable and arises, initially, from statistical variation in the superconducting order parameter, ψ , in Ginzberg-Landau theory (or equivalently, the energy gap Δ in BCS theory [10]). However, this fundamental contribution predicts only a width of 10^{-14} - 10^{-15} K. In reality, even in the most perfect crystal, the natural variation in isotopes present will provide a larger contribution, as much as $\approx 10^{-5}$ K. Any observed ΔT_c larger than this must be attributed to imperfections in the sample quality, such as impurities or polycrystalline structure [105].

Weak Links

Further broadening of magnetisation curves is often analysed in the paradigm of ‘weak-links’. In this context, ‘weak-links’ can refer to a couple of different phenomena. They can be thought of as areas with lower T_c , which could be a result of inhomogeneity in the doping of the sample, stacking faults or even the existence of the non-superconducting Ba spacer layers.

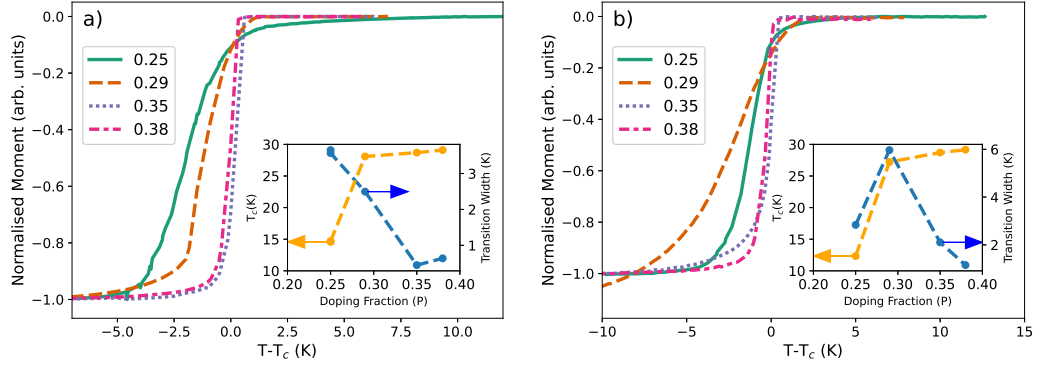


Figure 4.3: Normalised magnetic moments vs temperature for each sample highlight the difference in width of the superconducting transition. Perpendicular field orientation (a) shows a decreasing ΔT_c with doping, whereas the parallel orientation measurements (b) shows a large increase at optimal doping. All measurements taken in a field of $H = 25$ mT.

Suppression of the T_c of these weak-link regions will result in broadening of the superconducting transition as the sample as a whole will need these regions to transition in order to be fully connected and provide a susceptibility value of -1 associated with bulk superconductivity.

Weak links can also refer to a more concise phenomena of a 'conducting junction between bulk superconducting specimens' [106]. These junctions manifest in single crystals as either intrinsic intra-unit-cell weak-links, for example, a Josephson junction coupling between CuO oxide planes in cuprate superconductors, or inter-unit-cell weak-links such as those found in layered cuprate single crystals [107]. The presence of weak-links in a magnetic field is commonly associated with an increase in ΔT_c . ΔT_c for each of our samples, demonstrated in Figure 4.3, shows a significant level of variance, with the $x = 0.25, 0.29$ samples in particular displaying significant broadening.

The value of ΔT_c , calculated as the difference between T_c and the temperature at which 0.1 times the susceptibility above T_c was reached, can be seen

in the inset figures of Figure 4.3. The critically doped sample displays a ΔT_c of approximately 6 K, about 3 times the size of the other samples when in the parallel field orientation. There appears to be no direct correlation between the width of the transition and the value of T_c , nor any monotonic behaviour as a function of doping. Values obtained for T_c lie around 15 K for the underdoped sample, and between 27 K and 29 K for the optimally to overdoped side of the phase diagram.

4.1.2 Transition Temperature versus Doping

Figure 4.4 shows the results of the T_c measurements as a function of doping. The three samples at $x = 0.29$, 0.35, and 0.38 manifest very similar values of 28.9, 29.1, and 29.2 K, respectively. This is representative of the very broad peak in the T_c -doping phase diagram, and slow changes to T_c on the overdoped side, found in previous reports [43, 89]. To be consistent with previous literature, we will refer to the samples as underdoped ($x = 0.25$), critically doped ($x = 0.29$), near-optimally doped ($x = 0.35$), and overdoped ($x = 0.38$).

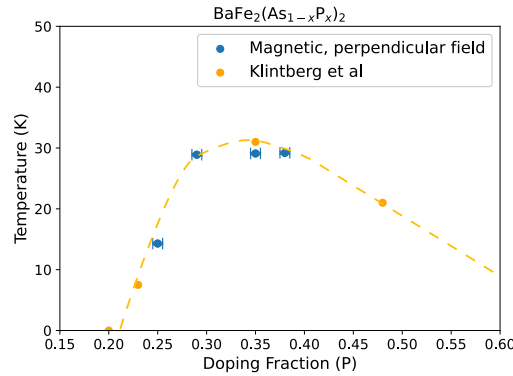


Figure 4.4: T_c as a function of doping for our series of crystals shows good agreement with that in study by Klintberg et al. [108], by comparison we can place our samples as underdoped ($x = 0.25$), critically doped (0.29), near optimally doped (0.35), and overdoped (0.38). The dashed line is a guide to the eye.

4.1.3 Magnetic Hysteresis Loops

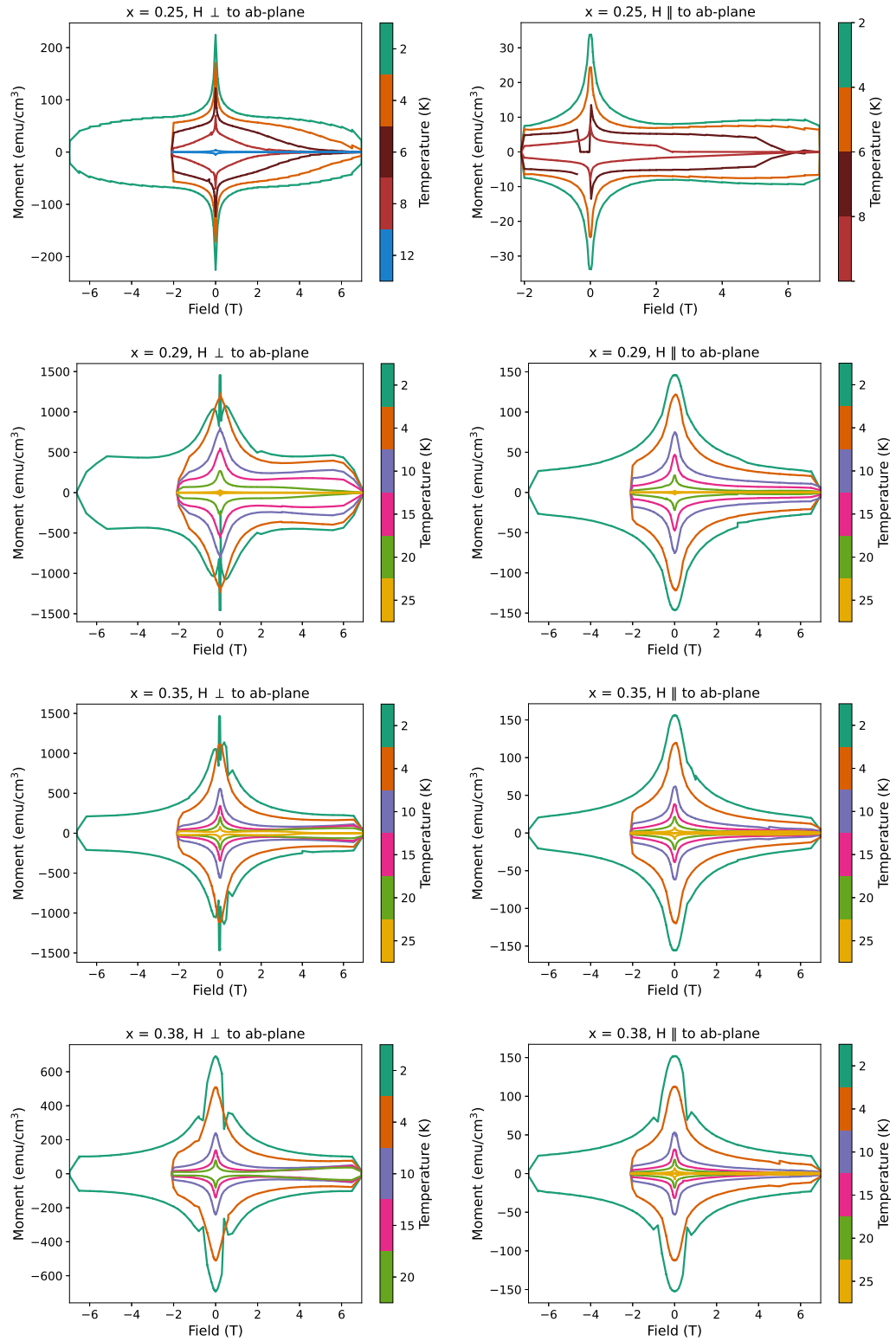


Figure 4.5: Hysteresis loops ranging from 2 K to T_c for each sample in perpendicular (left) and parallel (right) field orientation. A strong anisotropy in current characteristics result in a reduction of the observed moment as high as ten-fold for the parallel orientation. The second magnetisation peak becomes less distinct in parallel orientation, and the low-field irreversibility line manifests as a dip at low-fields in the low-temp, perpendicular orientation loops.

In order to investigate the J_c characteristics of our samples, we measured hysteresis loops for each sample in applied fields ranging from 0 T to 7 T, and temperatures from 2 K up to 25 K. Additionally, each set of measurements was done separately in fields oriented perpendicular and parallel to the ab-plane. The immediate results of these measurements can be seen in Figure 4.5. All the measurements manifest the stereotypical shape associated with hysteresis in most cuprate and iron-based superconductors.

We will now spend some time identifying some of the key features of this field dependence, and what we can then infer. These next features are illustrated in Figure 4.6.

Low-field Peak

The existence of a low-field peak is consistent with samples exhibiting pinning centres with strong individual pinning forces. This makes qualitative sense, when interpreted in the context of the Bean model, as strong pinning centres will prevent the exit of vortices pushed into the interior of the sample as we reach maximum applied field, resulting in a large remnant magnetisation enhanced by the lower likelihood of thermal creep.

The breadth and position of the low-field peak can be correlated to the ‘effective radius’ of the sample introduced in basic Bean model considerations [109], and thus, attempting to gather any quantitative conclusions from its relative size, breadth, or position (it has been observed to shift to fields higher than 0 T in a range of materials) would have to be taken with a rather large grain of salt, as the control over sample size was not systematic in this study.

The breadth of the low-field peak is consistently wider for the parallel orientation. At first thought this makes little sense, as the currents circulating in the ac-plane will be of smaller effective radius than those in the ab-plane,

and thus we would expect a sharper peak. However, this particular broadening is another symptom of the lack of demagnetisation in the parallel orientation, resulting in larger H_{c1} , and staving off penetration of vortices until a higher field.

Irreversibility Field

The point at which the field loop closes corresponds to having no lossless transport of current in the material. Another way of saying this is that we have pushed the sample into a regime where we have melted the flux line lattice, restoring their ability to move freely under the Lorentz forces and resulting in a resistive current flow. This is generally referred to as the irreversibility field (H_{irr}).

For the majority of loops we have measured, H_{irr} is not accessible due to the high critical fields in iron-based superconductors, and our applied fields being limited to 7 T. However, the critical fields scale with reduced temperature, $t = T/T_c$, and thus, for temperatures close to T_c we will be able to access approximate values of H_{irr} by introducing a criterion for the value of J_c when $H = H_{\text{irr}}$. For the remainder of this thesis, this criteria will be:

$$H_{\text{irr}} \approx H(J_c = 1000 \text{ A/cm}^2) \quad (27)$$

One other feature became prevalent at low temperatures, where we see a large dip in the magnetisation at low fields. These low-field features are in fact a manifestation of the low-field analogue of H_{irr} . This phenomena has also been referred to as 'vortex line wandering' [110, 111]. Because we have introduced only a small number of vortices at low fields, the intervortex distance is significantly larger than the London penetration depth and thus, the intervortex interaction reduces to near zero and, consequently, so does

the vortex shear modulus, c_{66} [15].

i.e.

$$c_{66} \propto \exp(a_0/\lambda) \quad (28)$$

Thus the fact that we are seeing this low-field melting behaviour is indicative of either a decreased penetration depth, or increased vortex lattice constant when compared to samples which do not behave in this way. In Figure 4.8 we can see that this melting can only be seen in the 2 K measurements, and moves to higher H with increased doping.

Second Magnetisation Peak (SMP)

Another distinct feature which is of particular interest is the prominence of a second local maximum in the field dependence. This feature is commonly referred to as the second magnetisation peak (SMP) or the fishtail effect, characterised by an increase in magnetisation at fields beyond the initial low-field peak. The SMP is definitely visible in 4.5, however it becomes much more apparent in the log-scale plots of J_c data further on (Figure 4.8).

We can observe that the peak is significantly suppressed in the parallel field orientation at low temperatures when compared to that of the perpendicular field orientation. This observation agrees with the measurements of Ishida et al. [112] where the reduction in J_c values coincided with the disappearance of SMP in their hysteresis loops.

A commonly cited reason for the existence of an SMP is a crossover from weak to strong forms of pinning [113], meaning that the vortex matter has changed to a phase which allows larger dislocations of the vortex from its equilibrium position and consequently increases the current restoring ca-

pability of the pinning force. This changeover could either be related to a change in the pinning strength of individual pinning centres, or a softening of the vortex lattice itself. The distinction between these two regimes is formalised in pinning theories of HTS vortices where the key concept is the need to balance the elastic forces of the vortex line itself with forces exerted by the Lorentz force and the potential well of the pinning site.

The fact our SMP is significantly diminished in the parallel orientation points to the possibility of a source of pinning which is invisible to some, or all, of the vortices when laying parallel to the ab -plane, and provides the force to restore high J_c values in the perpendicular field doping phase diagram. In the context of HTS pinning models, this would translate to a difference in the transverse trapping distance when changing orientation.

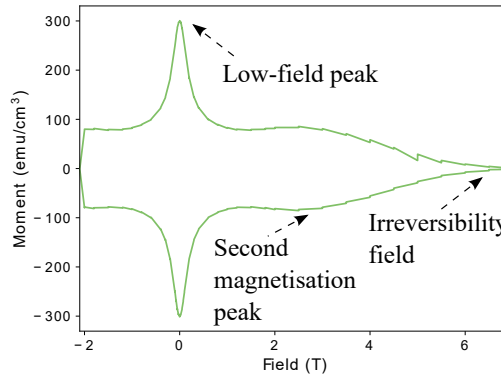


Figure 4.6: A plot of an exemplar hysteresis loop, pointing out standard features in each of our measurements. Each sample shows a high magnetisation at low-fields, followed by a plateau or second magnetisation peak. The point at which the loop closes is the irreversibility field of the sample.

The breadth of the low-field peak is very small in the underdoped sample, a feature which coincides with the smallest T_c by a factor of 2, and also being the only sample which does not exhibit the low-field irreversibility phenomena. These features of the loops are likely all connected and simply a result of the improved superconducting properties of the optimally and

overdoped samples resulting in larger lower critical fields and thus broader peaks, and consequently smaller numbers of vortices present for a given applied field value.

4.1.4 Critical Current Density versus Applied Field

Figure 4.8 presents the J_c versus applied field plots for each sample and orientation after transforming the hysteresis data via the Bean critical state model. In this series of samples we achieve a maximum of 0.93 MA/cm^2 , occurring in the $x = 0.29$ sample at 2 K. These numbers come in close to those presented in previous reports of J_c in P-doped Ba122 which find peaks in the critical current density on the order of 1 MA/cm^2 at the doping $x = 0.030$ [112, 114] associated with a quantum critical point and consequent divergent values for the superfluid density, penetration depth and charge carrier effective mass [60, 62, 63].

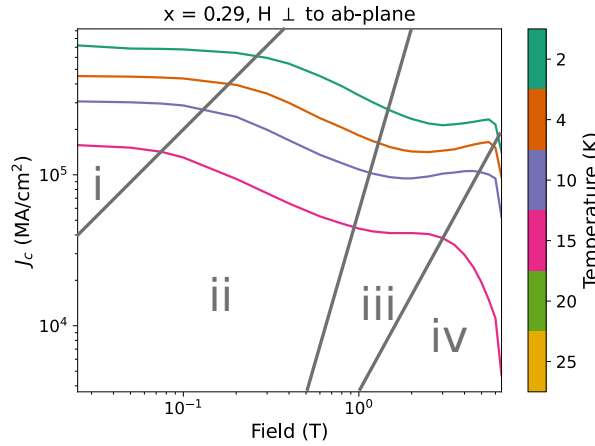


Figure 4.7: An exemplar of the J_c vs H plots displaying the four different regions related to different pinning regimes. i) is the initial, field independent region where all flux lines are successfully pinned individually, ii) is a power-law region where the Lorentz force is strong enough to overcome the pinning force of these pinning centres. iii) represents the onset of collective pinning as a simple plateau, often accompanied by an SM-P/fishtail effect, and iv) relates to the onset of depinned bundles of vortices causing large amounts off dissipation.

Field Dependent Pinning Regimes

Each of the key loop features split our field dependence into 4 reasonably distinct regimes which can be identified from each of the plots in Figure 4.8, and have been highlighted in Figure 4.7.

Region I

In Region I we have a flat, field independent region which maintains the same value for the J_c , i.e. the increase in field in this region corresponds to no noticeable uptick in the amount of flux creep induced dissipation.

The field up until which this behaviour is valid will be related to both the strength of the pinning centres as well as the number of vortices which are present in the material and thus, will be proportional to $H_{c1}(\theta)$ of the material as well as U . The dependence on the orientation of this field due to demagnetisation effects is highlighted by the presence of θ in this quantity, but it is useful to remember that these materials do also possess a more intrinsic anisotropy related to their layered, quasi-2D structure. Values for the lower critical field of this material generally sit around 25 mT, and have a field orientation anisotropy of between 1-3.

Region II - Strong Pinning Regime

Region II is the oft-cited strong pinning 'power-law region'. This is a feature most commonly associated with the presence of strong pinning centres, and thus the power-law exponent obtained when fitting to this region is predicted to be related to the strength of introduced pinning centres [20, 23].

Theoretically, this region exists because of the way in which a vortex remains pinned. A vortex which is considered rigid, i.e. without the ability to deform along its length, can not be reliably pinned due to its inability to

deform and optimise the pinning force along its length.

Consequently, in order to pin a vortex, we must balance the forces keeping a section of a vortex at a pinning site and the elastic energy associated with the deformation of that vortex. This logic results in the following equation for J_c vs H :

$$J_c \approx \frac{cn_p f_p^2 b}{\Phi_0 \bar{C}} \quad (29)$$

In other words, the critical current in a material is proportional to one over the effective 'spring constant' of a vortex (\bar{C}) which, in the case of pinning centres strong enough to pin a vortex by itself, is inversely proportional to \sqrt{B} .

$$\bar{C} \approx \frac{5}{4} \sqrt{\frac{\Phi_0}{4\pi B \epsilon_0 \epsilon_1}} \quad (30)$$

Here Φ_0 is the flux quantum, B the local magnetic field, ϵ_1 the vortex line energy, and $\epsilon_0 = \Phi_0^2 / (4\pi\lambda)^2$.

Thus, for each sample we fit the J_c vs H data to a simple power law equation i.e.:

$$J_c(H) = J_{c0} H^{-\mu} \quad (31)$$

From our J_c data, we can obtain μ as a function of doping and compare to equation 29, with a value of 0.5 being indicative of strong pinning [23, 115, 116]. The value of $\mu = 0.5$ is the result of theory which assumes that vortices are pinned only by direct collision with pinning centres. Extending

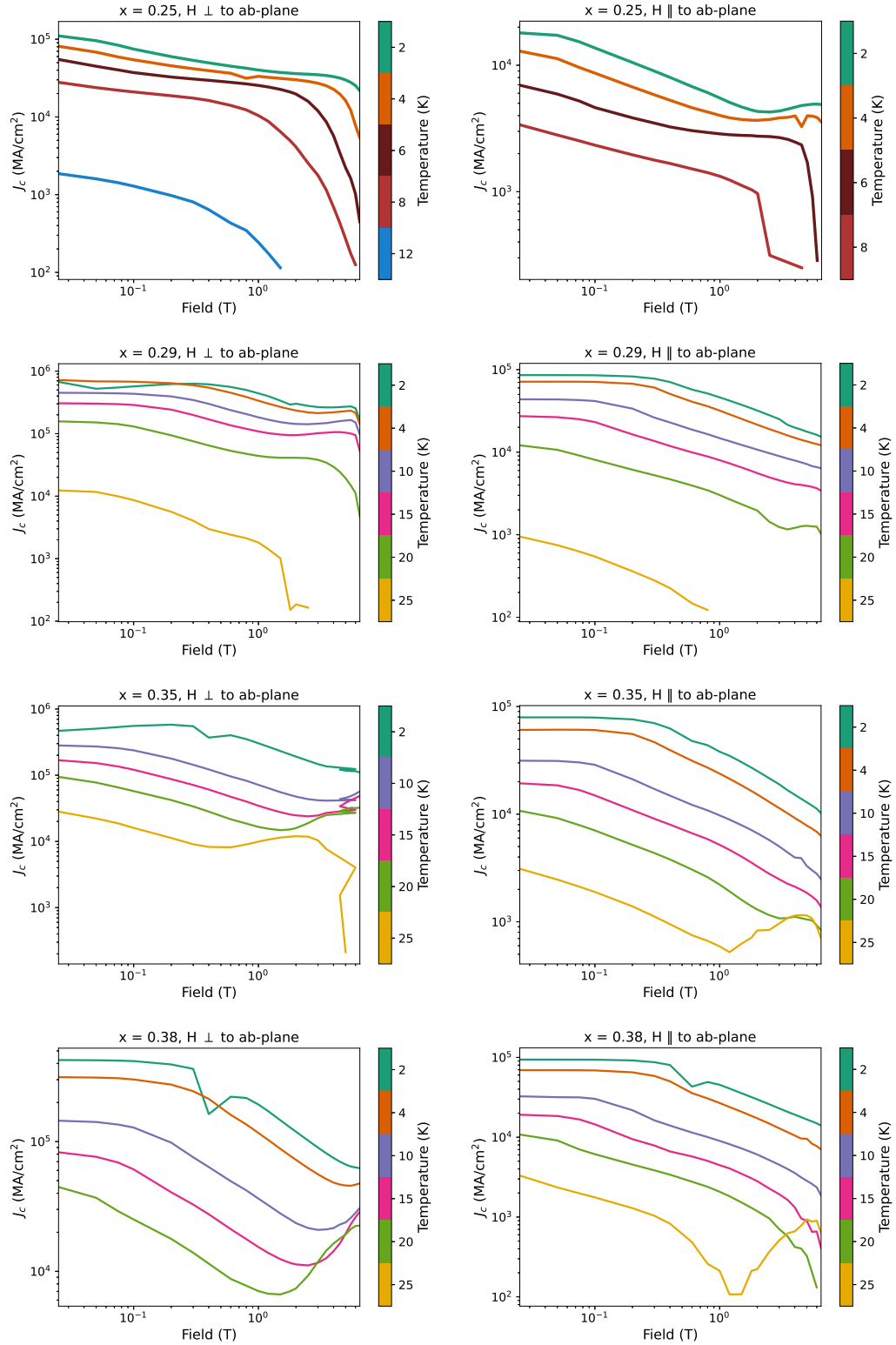


Figure 4.8: J_c vs applied field for each doping in perpendicular (left) and parallel (right) field orientations show a number of distinct features. In perpendicular field, the SMP becomes more distinct with increased doping, and moves to lower fields with increased temperature. The power-law region also becomes visible to higher fields with increased doping. In parallel orientation, the second magnetisation peak is not visible for the critical doping and beyond, and the strong pinning region becomes less distinct.

the theory to pinning cites that have the ability to interact with vortices via long-range interactions, i.e. a magnetic interaction or extended pinning centres, results in a prediction of $\mu = 5/8 = 0.625$ [20].

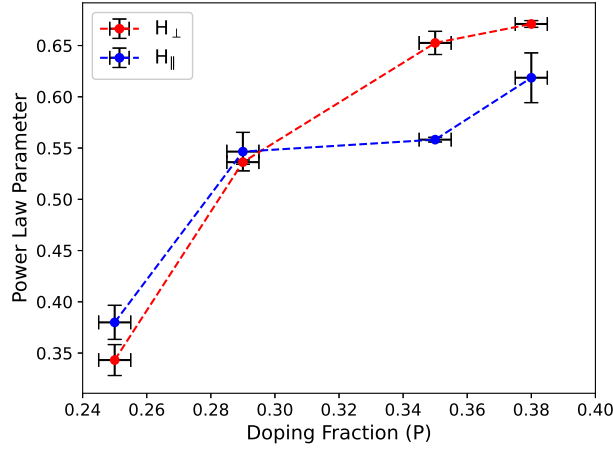


Figure 4.9: This plot of the parameter μ from 31 shows a shift at the critical doping to values consistent with what is expected for strong pinning centres: 0.5 for strong pins [20], and 0.625 associated with strong pins with long-range interactions [23]. These values were taken from fits to the 2 K and 4 K measurements of each sample.

Figure 4.9 presents the value of μ obtained for each sample. These values are the result of fitting to measurements at 2 K and 4 K, in order to stay in the single vortex regime where this analysis is valid, and uncertainties were calculated from the difference in results from these two temperatures. We see quite clearly that the underdoped sample returns values below 0.4, indicating that we do not have strong pinning for this sample. However, once we increase the doping we obtain values above 0.5.

This can be interpreted in terms of the increase in vortex core energy observed at $x = 0.3$ [60] in $\text{BaFe}_2(\text{As}_{1-x}\text{P}_x)_2$. This change in the vortex core energy appears to result in stronger pinning. Furthermore, as doping increases, μ continues to increase, indicating that the pinning centres induced by P-doping are resulting in long range pinning. Pinning in $\text{BaFe}_2(\text{As}_{1-x}\text{P}_x)_2$ has been shown to have a strong contribution from variations in local T_c

[112]. Thus, our observation can be interpreted as increased doping resulting in higher inhomogeneity and, consequently, larger regions of different T_c responsible for the main pinning mechanism in our samples.

Region III - Collective pinning

Region III marks the divergence of J_c characteristics from a single vortex regime. Collective pinning interactions result in a plateau in J_c vs H , and quite often also produce the high field peak at H_{SMP} .

When looking at the hysteresis loops, it appears that this series of crystals only exhibits a definitive SMP in the underdoped sample. However, the plots of J_c versus field on log-log scale show a very distinct and large SMP occurring at high fields. The robustness of this SMP leads to J_c being higher at 20 K than at 15 K for the $x = 0.38$ sample at 6 T. This is a much larger effect than anything seen in the Ni-doped series, and coincides well with other studies performed by Ishida [112].

It is also easier to see that the amount of doping is having a significant effect on the magnitude of the SMP. The underdoped sample clearly displays the fishtail effect in both field orientations, whereas all the other samples show an almost complete suppression of a second peak in the $H \parallel \text{ab-plane}$ orientation, except for at $T = 25$ K for the $x = 0.35$ sample.

Region IV - Vortex bundles

Finally, Region IV is characterised by a large suppression of J_c , quickly moving towards 0 A/cm^2 . This occurs when the Lorentz force acting on the vortices are sufficient to overcome the collective pinning forces associated with Region III. Once this occurs, bundles of vortices begin moving freely as a unit, resulting in a large increase in dissipation with increasing field.

4.1.5 J_c versus Doping

Figure 4.10 shows the evolution of J_c as a function of doping for this series of samples in both perpendicular (left) and parallel field (right). In perpendicular field we observe a peak in J_c which occurs at the critical doping, with a maximum value of 0.9 MA/cm^2 , rather than the optimal doping as one might initially expect. This value coincides very well with that measured by Ishida et al. [112], who obtained a value of 1.0 MA/cm^2 at a doping fraction of $x = 0.30$.

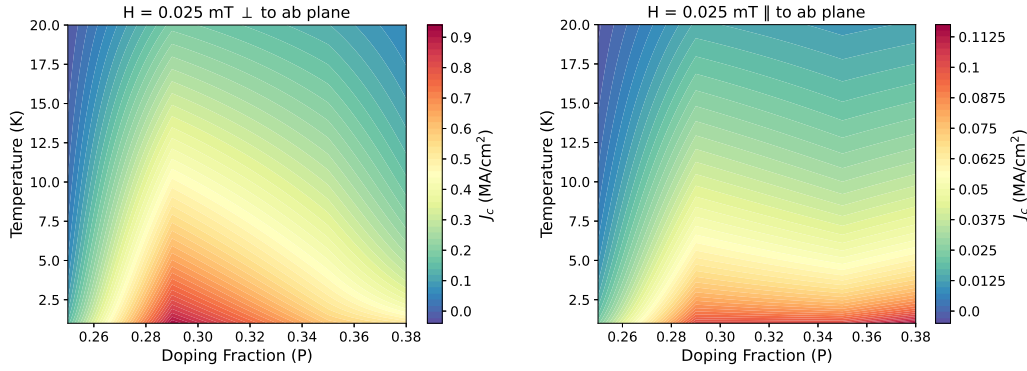


Figure 4.10: J_c vs x for our phosphorous doped sample shows a distinct maximum at $x = 0.29$ in perpendicular field orientation, whereas a parallel field orientation shows very similar values for the critically doped (0.29) and the most overdoped samples.

This observation of extreme values of J_c coincides with observations of other superconducting properties at the critical doping, although the vast majority of doping dependent J_c studies of $\text{BaFe}_2(\text{As}_{1-x}\text{P}_x)_2$ have been performed on thin films. In single crystals, $\text{BaFe}_2(\text{As}_{1-x}\text{P}_x)_2$ samples have been shown to also have peaks in the vortex core energy [60] and superconducting penetration depth [63, 117], which will lead to both an increased strength and range of pinning in the material. Thus, these measurements appear to be a further manifestation of the quantum critical behaviours of

$\text{BaFe}_2(\text{As}_{1-x}\text{P}_x)_2$ samples.

It is interesting to note that this peak is less prominent in the parallel field orientation, also coinciding with much smaller values of J_c , with a peak value just over 0.1 MA/cm^2 . A number of studies in doped BaFe_2As_2 single crystals have found that there is a coexistence of δl and δT_c pinning [112, 118, 119] thus, this difference could be interpreted as each orientation having a dominant contribution from different pinning mechanisms, and the quantum critical behaviour is favouring improvement in one of the two.

4.2 PRESSURE DEPENDENCE

Next, we took respective samples from the underdoped, critically doped and optimally/slightly overdoped region of our doping series, and looked into the effect we are returned when applying hydrostatic pressure up to values of 1.2 GPa . This method does not provide a means to reliably change the orientation of the sample within the pressure cell. Thus, all measurements involve pushing the sample flat, to the bottom of the capsule, resulting in a field oriented perpendicular to the ab -plane. Thus, any comparisons between these measurements with previous RSO measurements will be taken from the perpendicular RSO data.

4.2.1 *Effects of a Pressurisation Cycle on Samples*

For the sake of keeping track of the various ways in which the process of applying pressure can affect our measurements, we have taken ZFC and J_c measurements at 0 GPa before and after application of pressures up to 1.2 GPa . Over the course of this research program, it became clear that the pressurisation procedure had the ability to affect the experimental conditions, such as sample orientation and hydrostaticity, on a quite individual

basis. So, we present here first, the results of our pressure measurements individually, sample by sample.

Underdoped ($x = 0.25$)

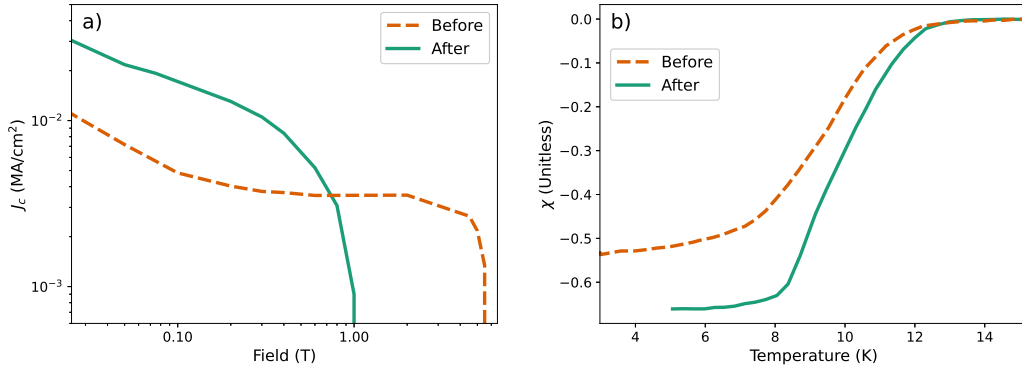


Figure 4.11: The underdoped pressure sample ($x = 0.25$) displays a decrease in H_{irr} and increase in J_c at low fields as a result of the pressurisation cycle (a). The ZFC measurements (b) show an increase in demagnetisation factor, meaning this sample was pushed to a more perpendicular orientation upon pressurisation.

As shown in Figure 4.11, there is an observable change in the ZFC and J_c characteristics before and after the the application of pressure. The initial J_c measurement returned a value of only 10,000 A/cm² at 25 mT, which correlates much closer to values obtained for the parallel field orientation values obtained outside of the pressure cell. This value is ameliorated by a factor of 3 after the pressure cycle was finished, and also coincides with a change in H_{irr} which is approximately doubled during this process.

This all points to a movement from parallel to perpendicular field orientation over the course of the measurements. This is reinforced by the ZFC measurements, which show a slight shift to a larger susceptibility, Thus, it seems likely that upon pressurisation, the sample will have been pushed flat inside the Teflon capsule.

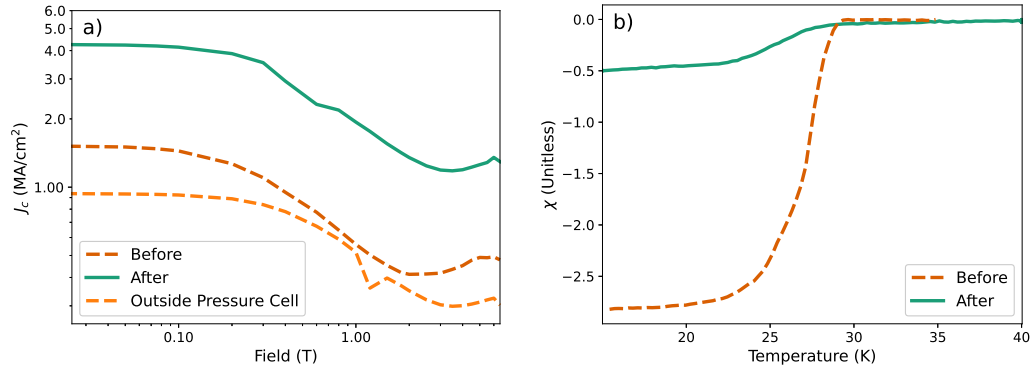
Critical doping ($x = 0.29$)

Figure 4.12: The $x = 0.29$ sample shows a large change in magnetisation (b) at 0 GPa before and after a pressurisation. This corresponds to much larger measured values of J_c (a). The orange dashed line shows a J_c measurement in the perpendicular orientation outside of the pressure cell.

For the $x = 0.29$ sample, it seems the situation is pretty clear as seen in Figure 4.12. The sample shows a massive change in demagnetisation factor after the application of pressure, and coincides with a massive improvement in J_c . However, again, this picture is not quite as simple.

First of all, the magnitude of the low temperature susceptibility value (-2.5) is much larger than what we would expect for a sample in either orientation. Nor do the values of J_c point toward a change in orientation. For the initial measurement of J_c in the pressure cell, the value of 1.5 MA/cm² is already larger than the value of 1 MA/cm² observed in our measurements before placing in the cell. If the sample were indeed parallel to begin with, we would expect J_c values to be an order of magnitude lower.

The other explanation for the change in the measured moment of our samples as we increase the pressure from 0 GPa is that the pressure is homogenising our samples, connecting regions which were previously disconnected by weak-links in the sample growth structure. This is a possible

interpretation of the behaviour we have seen here, as encouraging improved connection means that the area around which a continuous screening current can flow increases, resulting in a larger measured magnetic moment.

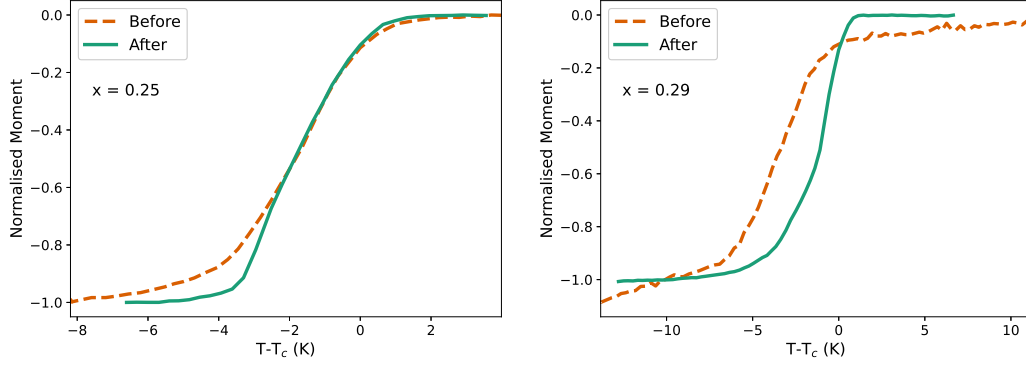


Figure 4.13: Plots of normalised moment for $x = 0.25$ (left) and 0.29 (right) show the superconducting transitions changing before and after pressurisation. The samples display less weak-link type behaviour post pressurisation, indicating an increased connectivity of the superconducting bulk potentially responsible for the observed increase in J_c .

This behaviour should be visible in a reduction of weak-link behaviour in the ZFC curves where weak-links are associated with a broadening of the curve. As shown in Figure 4.13, each of these samples initially show a larger ΔT_c - indicating that this interpretation could indeed be the case.

Because these changes are related to the quality of the sample, when comparing to other pressures, we will use the final (post-pressurisation) values of J_c at 0 GPa so as to be sure we are comparing measurements in the same field orientation.

Optimally Doped ($x = 0.35$)

The final pressure dependent sample does not display any of the peculiarities seen in the previous two samples. There is a slight improvement in J_c after the pressure cycle which coincides with a small increase in the magnitude of demagnetisation, consistent with a slight change in orientation

caused by the applied pressure. This sample also shows no change in the ZFC profile, with before and after curves lying almost completely on top of one another (Figure 4.19).

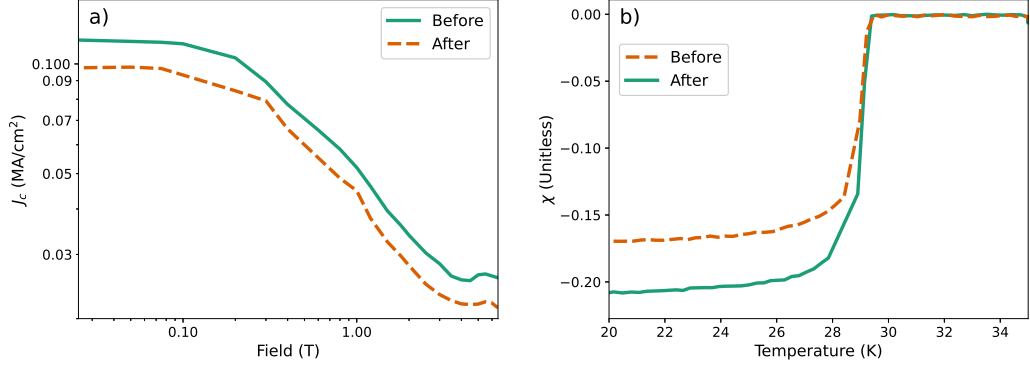


Figure 4.14: The $x = 0.35$ sample shows very consistent behaviour before and after pressurisation. Low temperature values of susceptibility remain very similar (b), as do the J_c measurements (a).

These observations make interpretation of data from this sample the most reliable. It is a distinct possibility that this improved homogeneity is related to the fact that this sample is doped further from the QCP making the formation of alternate phases within the sample less likely. In the next section we will look at the ZFC and T_c characteristics as a function of pressure in order to elucidate the differences in these samples.

4.2.2 Transition Temperature versus Pressure

Upon applying pressures to the P-doped single crystals, we immediately observe very significant changes to the superconducting properties, particular in reference to the T_c of each sample. All three samples exhibited significant decreases in T_c at very low pressures, as demonstrated in Figure 4.15. Immediately upon applying 0.2 GPa of pressure we observed decreases of 6.0 K, 12.7 K, and 6.6 K for the $x = 0.25$, 0.29, and 0.35 samples respectively. These losses correspond to percentage decreases of 50, 46, and 22 % of the

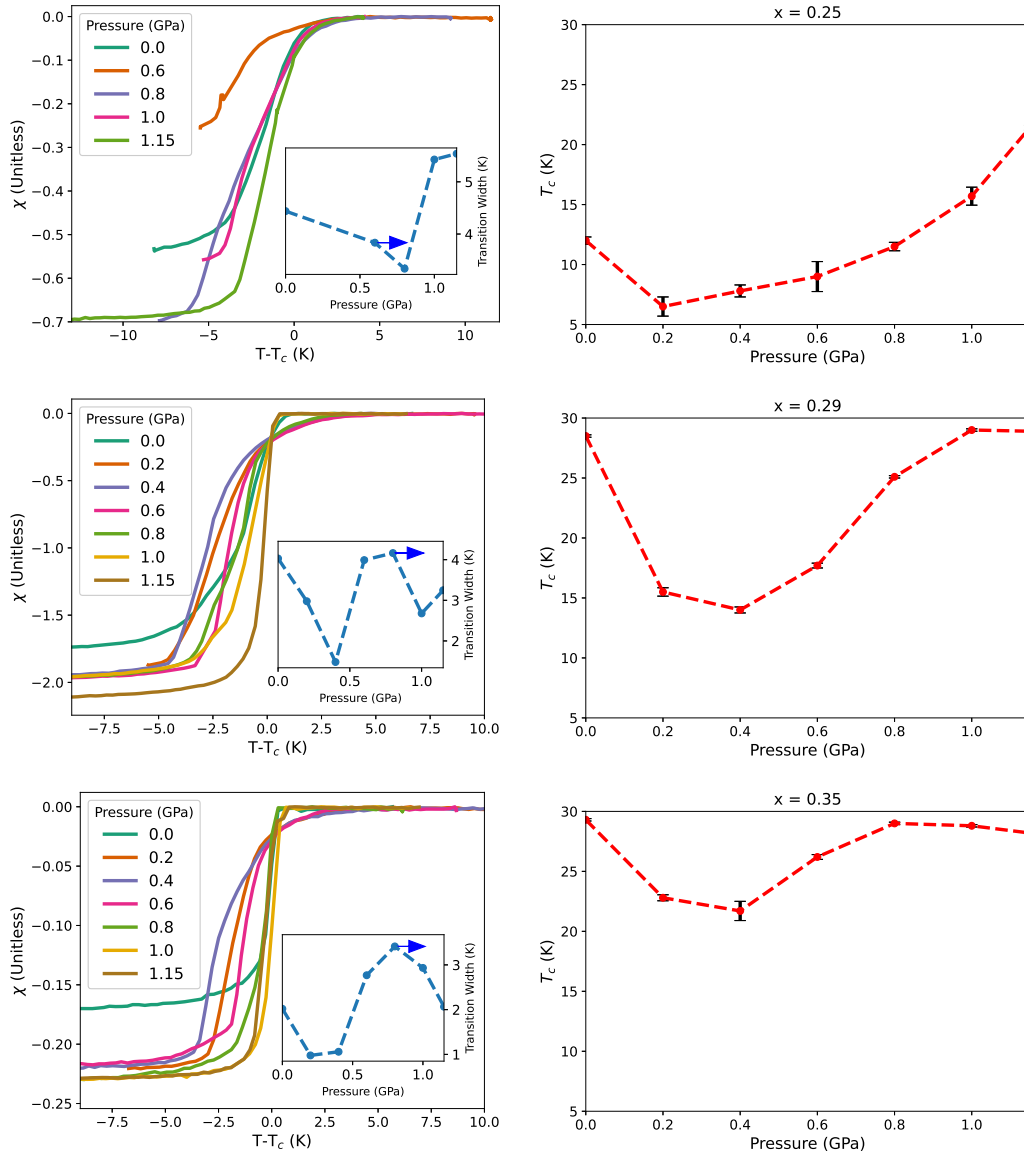


Figure 4.15: ZFC curves (left) and T_c (right) as a function of applied pressure present massive changes upon pressurisation to 0.2 GPa. T_c decreases immediately and consistently for all samples, by as much as 50 % in the critically doped sample. Lower values of T_c correspond to broader transition widths. The negative trend then reverses and, at approximately 0.8 GPa, each sample returns to more traditional pressure dependence.

unpressurised T_c values.

Upon further pressurisation of the samples T_c continues to decrease, until approximately 0.4-0.6 GPa where the trend reverses and T_c begins to improve. The underdoped sample achieves a value of 21.2 K, which is 9.2 K (77 %) higher than its 0 GPa value and corresponds to an overall dT_c/dP of 7.6 K/GPa. This is significantly larger than that found for a sample of similar doping ($x = 0.23$) in reference [108]. The optimally doped samples only reach values of T_c very similar to their initial values, reiterating the fact that the maximum in pressure dependent phase diagrams becomes more shallow for higher doping. The fact that the underdoped sample improves so much more in T_c is also related to the superconducting dome being significantly steeper at the value $x = 0.25$.

Our proposed explanation of this data is as follows: At zero pressure we can, trivially, assume the strains applied to our sample to be isotropic. However, as we apply pressure, contractions along the c-axis will be favoured, causing a decrease in T_c up until contraction along this axis is saturated. Subsequently, pressure will begin to favour contraction along the a-axis, restoring values in T_c when an equilibrium is reached.

This explanation relies on a direct correlation between T_c , and the ratio c/a . It is also important to note here that we are talking about the isotropic strains rather than pressures, which will take into account the different elastic moduli of the orthogonal lattice parameters. That is to say, that we have no reason to believe that energy needed to compress the a lattice parameter by some percentage is the same as that needed to compress c.

To illustrate, first we assume we have no shear stresses and pressures applied from all directions are equal (i.e. hydrostaticity), then:

$$\sigma_{ii} = c_{ii}^{jj} \epsilon_{jj} \quad (32)$$

where σ_{ii} and ϵ_{jj} are the components of the stress and strain tensors (see Figure ??), respectively, c_{ii}^{jj} are the proportionality constants or elasticity. I.e.

$$\sigma_{11} = c_{11}\epsilon_{11} + c_{12}\epsilon_{22} + c_{13}\epsilon_{33} \quad (33)$$

$$\sigma_{22} = c_{21}\epsilon_{11} + c_{22}\epsilon_{22} + c_{23}\epsilon_{33} \quad (34)$$

$$\sigma_{33} = c_{31}\epsilon_{11} + c_{32}\epsilon_{22} + c_{33}\epsilon_{33} \quad (35)$$

and via imposing a symmetry between the x and y axis lattice parameters, i.e. $\epsilon_{11} = \epsilon_{22}$, and $c_{i1} = c_{i2} = c_{2i} = c_{1i}$, for $i = 1, 2, 3$, we arrive at

$$\epsilon_{33} = \frac{c_{11} + c_{12} - 2c_{13}}{c_{33} - c_{13}} \epsilon_{11} \quad (36)$$

When plugging in values for the elastic moduli from [120] for a similar material this demonstrates that the percentage change in the c-axis lattice parameter could be as much as 3.5 times the corresponding change in a.

Thus, initial small pressures will create large changes in the c/a ratio and T_c until the approximation of our lattice lengths acting like springs breaks down, c will become 'stiff' and energy from the applied pressures will begin to pour into changing a , restoring the c/a ratio and eventually returning to an equilibrium with approximately isotropic strains.

Furthermore, because the change in T_c is related to the strain induced in the c-axis lattice parameter, the degree to which T_c diminishes must be correlated with the elasticity along the c-axis. By comparing to previous pressure dependent measurements of Colombier et al. [108] at $x = 0$ we

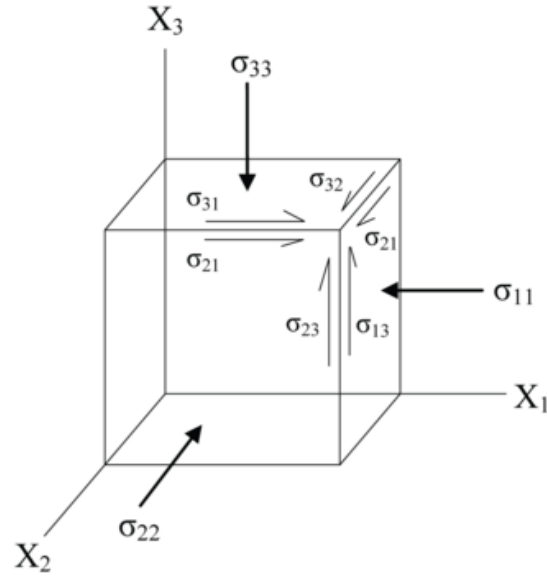


Figure 4.16: Stresses applied to a sample have associated components, σ_{ij} , for a stress applied to the face with normal component in the i -direction, in the direction j . Each stress results in a strain ϵ_{ij} , with elasticity (c) being the constant of proportionality.

find ourselves in a position to evaluate the magneto-elastic lattice softening versus doping. That is to say, we approximate the softening of the lattice (in the z -direction) to be proportional to the difference in pressure needed to attain the same changes in T_c between undoped and doped samples:

i.e. applying 0.2 GPa of pressure to the $x = 0.29$ sample results in decrease in T_c from 29 K to 16 K, the amount of pressure needed to induce that change in the undoped sample would be 0.8 GPa. For the 0.25 and 0.35 sample, this effective pressure (ΔP_{eff}) is 0.2 GPa and 1.4 GPa, respectively.

We made these approximations by fitting a simple parabola to T_c versus pressure for the undoped data, shown in Figure 4.17. Note that we have assumed, based on the data of Klintberg et al., that the application of low pressures along the z -axis direction moves the sample to the equivalent of a lower doping, i.e. to the left on the T_c -doping phase diagram. Note this does introduce some ambiguity as to what side of the peak in the T_c our optimally doped sample lies on.

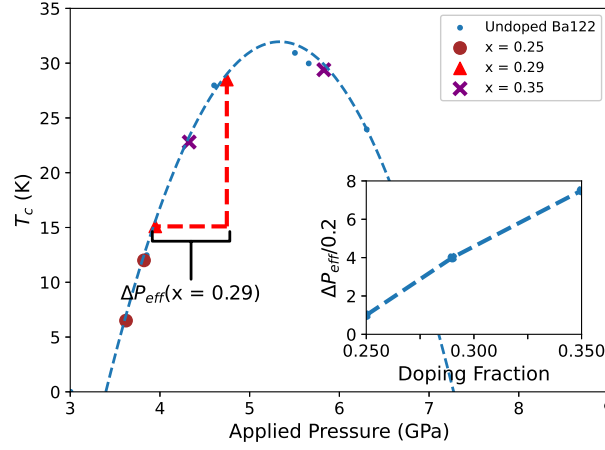


Figure 4.17: Fitting to pressure dependent measurements of undoped Ba122 from Colombier et al. [5], allows the estimate of pressure needed to induce the changes in T_c observed when applying 0.2 GPa to our doped samples (ΔP_{eff}). The inset shows a steady increase in ΔP_{eff} with doping, indicative of an increase in strains induced by hydrostatic pressure.

The inset of Figure 4.17 demonstrates that our underdoped sample experiences no magneto-elastic softening with a one-to-one ratio of pressure to effective pressure. The samples at higher doping however show marked changes in the susceptibility of T_c to pressure. Applying 0.2 GPa of pressure results in changes to T_c corresponding to pressure 4-10 times larger than the undoped sample. This is a clear demonstration of increased susceptibility of the c-axis to uniaxial pressure, for dopings at, and beyond, the critical doping near $x = 0.30$.

To further back up the critical behaviour we appear to be observing for the $x = 0.29$ sample, we performed measurements of H_{c1} versus doping for samples from $x = 0.25$ to 0.35 including one sample at $x = 0.33$ which was from a different batch of samples. These values were again determined using magnetic measurements, performed on MPMS, and following the method outlined in reference [121].

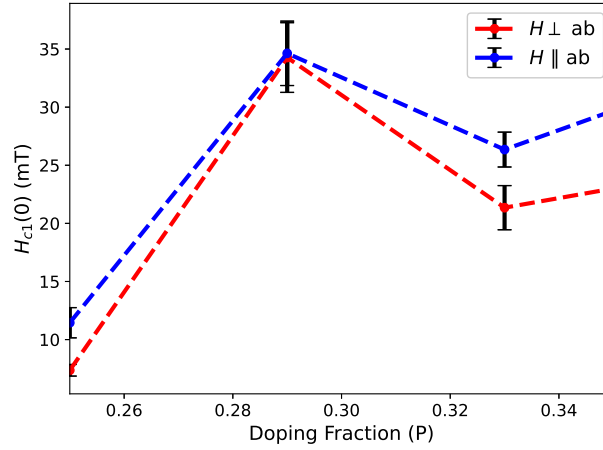


Figure 4.18: Our $\text{BaFe}_2(\text{As}_{1-x}\text{P}_x)_2$ series demonstrate a peak in $H_{c1}(0)$ at $x = 0.29$, for both field orientations. This is a result which has been linked in reference [60] to a peak in core energy of vortices.

Figure 4.18 clearly demonstrates that we observed a peak in $H_{c1}(0)$ at the critical doping. This confirms the same result obtained in reference [60] and, more importantly for us, definitively shows that the increased susceptibility to pressure, and peak in J_c we have observed for the $x = 0.29$ sample are very likely to be occurring in conjunction with an enhancement of the vortex core energy associated with a QCP [60].

Further clues as to what is responsible for these changes, or at the very least the effects we expect to see resulting from them can be taken from the evolution of the ΔT_c of each measurement. In Figure 4.15, we can see that the changes in ΔT_c follow a qualitatively similar trend to that of T_c .

Figure 4.19 shows that this broadening of the ZFC curve is also repeatable, as we cycled the same sample ($x = 0.35$) up to pressures of 0.6 GPa again and finding a repetition of the same behaviour. When doing this, the values for T_c that were obtained were slightly more (i.e. decreased less) over this pressure range. This is likely due to the irreversible nature of compressing the Teflon capsule in the pressure cell, and consequently being unable to

transfer as much pressure to the sample the second time around.

ΔT_c is related to the significance of thermal fluctuations in the material via the relation $\Delta T_c < T_c G_i$ where G_i is the Ginsberg number - the dimensionless scale parameter associated with the presence of thermal fluctuations [15]. This is, in turn, related to the penetration depth via $G_i^{2D} = T_c / \sqrt{2} \epsilon_0 d$ where we have assumed a 2-dimensional material i.e. a material where the coherence length is significantly lower than the interlayer distance d , and $\epsilon_0 = (\Phi / 4\pi\lambda)^2$.

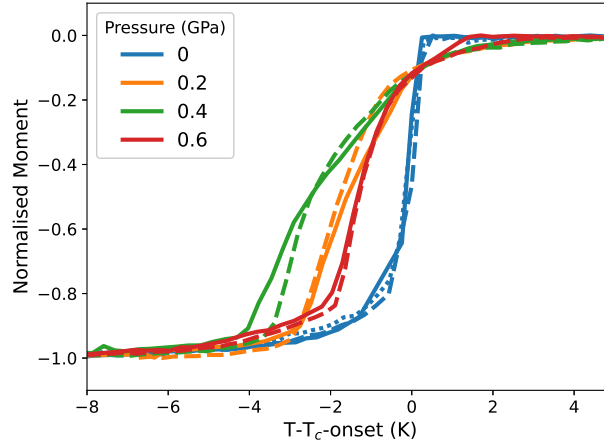


Figure 4.19: The changes to transition width (and T_c) are repeatable upon a performing a second pressurisation cycle (dashed lines) on the same sample ($x = 0.35$). This rules out physical cracking of the sample as being responsible for this behaviour.

This allows us to obtain estimates for the in-plane London penetration depth. The values obtained from this rough calculation return values on the same order of magnitude as those obtained by other studies [122], with values peaking around 300 nm, the same value observed in reference [63] for the sharp peak obtained at critical doping, and going as low as 60 nm. This correlates our diminishing of T_c with a corresponding peak in the penetration depth which will have an immediate impact on the nature of pinning, and thus, J_c as a function of pressure.

4.2.3 *Magnetic Hysteresis Loops*

Figure 4.20 shows the magnetisation loops taken as a function of pressure for each representative sample at 2 K.

The flow on effects from the T_c behaviours is made apparent by significant decreases in J_c immediately upon pressurisation from 0 to 0.2-0.4 GPa, this is shown quite clearly in Figure 4.21. At 2 K and 0.25 mT J_c displays catastrophic decreases; in the 0.25 sample we observe the signal immediately reducing to the point where we have no discernible hysteresis more significant than noise levels, effectively reducing J_c from 0.03 MA/cm² to 0 at a rate of 0.15 MA/cm²/GPa. In the critically doped sample we see a decrease from 4.2 to 0.7 MA/cm², a reduction of 83 % at a rate of 19 MA/cm²/GPa. The effect in the $x = 0.35$ sample is considerably less extreme with a 25 % reduction in J_c from 0.105 to 0.077 MA/cm² at 0.7 MA/cm²/GPa.

4.2.4 *Pressure Effects on Critical Current Density*

The J_c vs H plots also show distinctive effects on the existence of the SMP in these samples. In the underdoped sample the application of pressure induces a more prominent SMP. In the context of the rest of our measurements this further backs up the hypothesis of an increase in the elasticity of the lattice structure as we move towards the critical doping. The highest value of T_c in this sample occurs at 1.15 GPa with a value of 21.2 K, which is approximately the value of T_c one would expect for an unstressed sample at $x \approx 0.27$.

By the same logic we see that the $x = 0.35$ sample loses its SMP by the time we have applied 1 GPa of pressure, meaning that once we have pushed the pressure beyond the initial anisotropic strain stage, we have pushed this sample further from the quantum critical behaviour expected around the

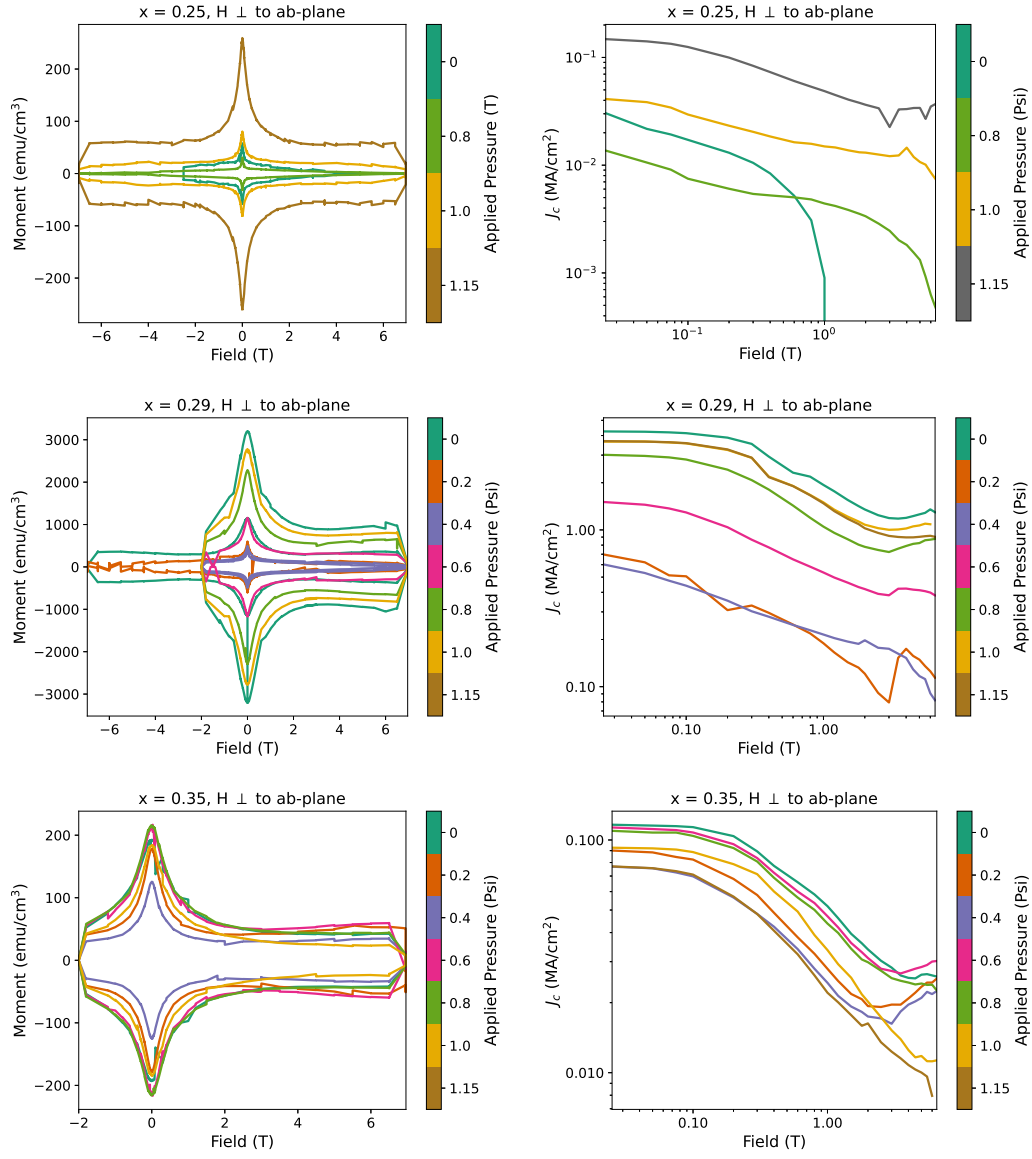


Figure 4.20: Hysteresis loops (left) and J_c plots (right) for each phosphorous doped sample with applied pressures between 0 and 1.2 GPa. Each sample shows a range of J_c values, with the $x = 0.25$ and 0.29 samples showing the largest changes. This correlates with these samples displaying the larger percentage decreases of T_c with pressure.

critical doping, resulting in a denigration of the elasticity related SMP.

Figure 4.21 shows the contour plot of J_c for all fields and pressures. Clearly from Figure 4.21 the observed decreases in J_c follow the trend set out by T_c which is to be expected. However there is still the possibility for pinning landscapes to further affect the materials current carrying properties.

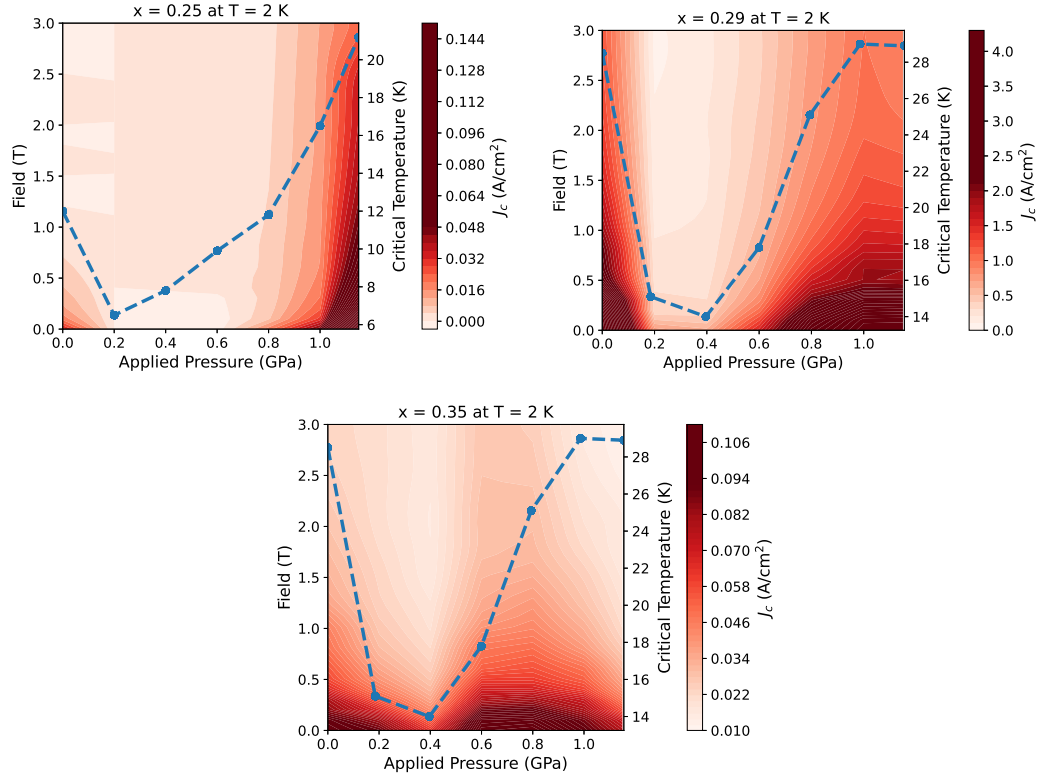


Figure 4.21: All samples show marked decreases in J_c immediately upon pressurisation, followed by a recovery to approximately the same initial values or higher upon reaching 1 GPa. This is the same trend as observed for T_c and thus clearly the two are linked in these samples.

4.2.5 Comparison to Previous Pressure Studies

There are a couple of key reports already published which, in conjunction with the present study fill out the full pressure range of behaviour of T_c with pressure in the P-doped Ba122 series. Our present study occupies a

parameter space which we could call intermediate pressures, whereas another study by Kuo et al. [42] applies very small pressures (< 10 MPa) and a study by Klintberg et al. [108] applies large pressures (up to 10 GPa, not smaller than 1 GPa). These two studies seem to paint very different pictures but, as we shall show, our data provides a very sensible and intuitive link between the two pressure ranges.

The study by Kuo et al. applied uniaxial pressures along the [110], [100] and [001] crystallographic directions. Applying pressures of < 10 MPa, they measured significant changes in both T_c and T_N of each sample of a range of dopings. This study applied pressure using a cantilever adjusted using a turnable screw without any pressure medium [123], and is an important reference for us in terms of reinforcing that our observed phenomena is not due to the hydrostaticity (or lack thereof) of our experimental setup.

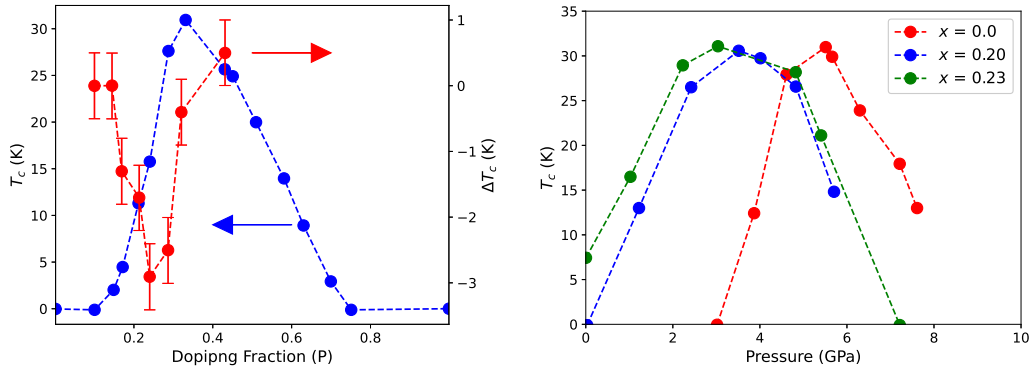


Figure 4.22: Changes in T_c are approximately proportional to the gradient of T_c vs doping (left) in P-Ba122 when applying small uniaxial pressures [42]. The figure right shows that the same material manifests a common dome-like behaviour for large hydrostatic pressures up to 7 GPa which is shifted to lower pressures with increased doping [108].

Figure 4.22 shows that changes in T_c as large as -3 K were achieved, even at the very small applied pressures, demonstrating that the immediate effect of applying pressure is to decrease T_c at a rapid rate. dT_c/dP in this study would be extremely large (~ 300 K/GPa), however it is obvious that this rate

is unsustainable, so it leaves the question as to how this will behave with continued application of pressure unanswered - but of which we have now shown, reverses after a certain amount of strain is applied. The comparison between the rates of change in T_c between this study and ours are not immediately useful due the difference in the methods of applying pressure i.e. uniaxial vs hydrostatic. Moreover, it is clearly demonstrated that ΔT_c is proportional to dT_c/dx at that particular doping.

The study by Klintberg et al. [108] shows that the application of pressure to P-Ba122 single crystals resulted in the standard dome like behaviour associated with both doping and pressure effects on T_c . The breadth and the peak position of the resultant domes appeared directly correlated with the level of doping, resulting in underdoped samples exhibiting a positive dT_c/dx and overdoped samples exhibiting a negative value for dT_c/dx . However, this particular study was done with the smallest pressure step being 1 GPa thus completely skipping over the values seen here. Our values of T_c obtained for both 0 GPa and 1-1.2 GPa line up very nicely with their reported changes in T_c .

Thus, the whole picture lines up as follows: Initial application of pressure has an large depressive effect on T_c in this material when applied along the c-axis direction. Hydrostatic pressures initially favour changes in the c-axis, but once the amount of energy needed to compress c becomes larger, a also begins to compress, leading to a reversal of the trend in c/a until an equilibrium is reached and both c and a will see equal applied strains. Once this equilibrium is reached, at high hydrostatic pressures, the value of c/a will remain relatively constant but the bond lengths will continue to be compressed resulting in the dome-like behaviour we expect to see traditionally. The breadth of this dome is dependent on the amount of phosphorous doping, due to the fact that it effects the elasticity of the lattice parameters,

as we have shown in Figure 4.17.

A stark difference in T_c vs P behaviours below 1 GPa can be found in other compounds. For example, pressure dependent measurements of undoped SrFe_2As_2 [71], and fluorine doped $\text{LaO}_{1-x}\text{F}_x\text{FeAs}$ [67, 68] show rapid increases of T_c below 2 GPa before changing to a broad dome-like behaviour under hydrostatic conditions. Whether or not the low pressure effects manifest as an increase or decrease in T_c will be dependent on whether the initial bond Fe-As bond angle is below or above the ideal tetragonal value.

To contrast, a significant number of materials appear to definitively not display any non-linear low pressure T_c behaviours. For example, in the cobalt doped version of this compound, T_N was shown to only be affected by uniaxial pressures approximately 5 times those applied to the phosphorous samples [42]. In addition, pressure studies on hole doped Ba_{122} [124], LaFePO [125], $\text{Na}_{1-x}\text{FeAs}$ [66], $\text{LaO}_{1-x}\text{F}_x\text{FeAs}$ [67, 68] and cuprate superconductors including Hg_{1223} , Hg_{1212} [126, 127] show a smooth dome-like behaviour. For the K and Co doped Ba_{122} examples, as a function of doping, T_N and T_s grow apart [93, 128], whereas the coupling between these two transitions is enhanced when approaching optimal P concentrations [42]. This points towards a strong magneto-elastic coupling a necessary condition to realise the behaviour we see in this study. In subsequent chapters, we will investigate whether this logic continues to hold when we investigate pressure dependent measurements of nickel doped Ba_{122} .

4.3 CONCLUSIONS

To conclude, we will reiterate the key findings in this chapter:

- Measurements of T_c as a function of applied pressure uncovered a very non-linear trend with large initial decreases as high as 50 % in

the critically doped sample, followed by a reversal of this trend, and the recovery of initial values or higher. The values of J_c followed the same trend, indicating that the suppression of superconductivity is more significant than pinning characteristics when interpreting changes of J_c with pressure in $\text{BaFe}_2(\text{As}_{1-x}\text{P}_x)_2$.

- We attribute this non-linear behaviour to anisotropic strains induced in the material structure when applying hydrostatic pressure. In this scenario, applied hydrostatic pressure will favour compression along the c-axis due to the difference in elastic moduli along different crystallographic axis. This, effectively uniaxial, pressure suppresses the value of T_c up until the a pressure ≈ 0.4 GPa at which point the trend reverses and subsequent strain of the a-axis restores the initial value of T_c .
- Furthermore, we have shown by comparing the changes in T_c as a function of doping that the c-axis lattice parameter is more susceptible to compression as we approach the critical doping value of $x = 0.29$, demonstrating a further anomalous behaviour to attribute to the QCP at this doping.

DOPING DEPENDENT PROPERTIES OF $\text{Ba}(\text{Fe}_{1-x}\text{Ni}_x)_2\text{As}_2$ SINGLE CRYSTALS

The purpose of this chapter is to establish a number of interesting superconducting properties of nickel doped $\text{Ba}(\text{Fe}_{1-x}\text{Ni}_x)_2\text{As}_2$ (Ni-Ba122) single crystals. We have performed ZFC (T_c), and hysteresis (J_c) measurements for a series of 8 different samples of $\text{Ba}(\text{Fe}_{1-x}\text{Ni}_x)_2\text{As}_2$, with one underdoped ($x = 0.041$), three optimally doped ($x = 0.048, 0.049$, and 0.050), and four overdoped samples ($x = 0.059, 0.060, 0.066, 0.075$). From these measurements we extract the J_c and T_c phase diagrams as well as pinning characteristics extracted from the Dew-Hughes and weak collective/strong pinning models.

As we will show, this series manifests optimal values of J_c and T_c at two different doping levels, displays evidence of a core-pinning mechanism, and pinning centres which can be characterised as providing strong pinning. Also, fits to the power-law region of J_c vs H curves, and pinning force plots show a distinct change in pinning with field orientation. These observations, viewed in the context of existing pinning models, provide information about the ideal conditions for increased J_c in Ni-Ba122. Furthermore, they provide valuable information to compare to similar results for other dopant materials, and provide the foundation for understanding results in our subsequent chapters on pressure effects in doped BaFe_2As_2 .

The Effect of Doping

First of all we will introduce how we expect doping with nickel to affect our samples, as there are multiple avenues to think about. As we are substitut-

ing Fe ($Z = 26$) for Ni ($Z = 28$) there is both a difference in the ionic radii (78, 69 pm for $2+$ Fe and Ni respectively [129]) of the atoms at the substitution sites as well as a change in the macroscopic electronic character of the material due to the difference in electronic structure ($(\text{Ar}) 3d^6 4s^2$, $(\text{Ar}) 3d^8 4s^2$).

As is the case for isovalent doping, electron doping results in changes to the parameters involved in the physical structure of the material (bond angles, pnictogen heights, bond lengths etc.). Doping with Ni results in a linear reduction of the c -axis, and very small changes along the a -axis [46, 130, 131], and consequently affects normal state transition temperatures as well as T_c , J_c and associated superconducting parameters.

As shown in Figure 5.1 Ni doping suppresses the c -axis lattice parameter at the same percentage rate as other electron dopants Cu and Co [46]. However there is a difference in the rate at which the a -axis lattice parameter changes, with more electrons per dopant atom resulting in a smaller percentage increase in a . This results in a steeper gradient for the ratio c/a , when compared to $\text{Ba}(\text{Fe}_{1-x}\text{Co}_x)_2\text{As}_2$, proportional to the number of extra electrons per substitution site. Because of this relationship to the added electrons, the difference in changes to c/a is expected to be larger when comparing to $\text{BaFe}_2(\text{As}_{1-x}\text{P}_x)_2$. This is one way in which we know the introduction of extra charge via the doping atom to contrast with the P doping presented in the previous chapter.

Substitution at the Fe site is often referred to as 'direct' substitution due to the fact that excess electrons from donor atoms such as Co or Ni are of $3d$ character, and the Fermi level for these materials is largely comprised of $3d$ electrons [132]. However, dopant atoms are unlikely, if chemical intuition is to be believed, to donate extra electrons to the system as this would imply Co, and Ni acting as $+3$ and $+4$ ions respectively.

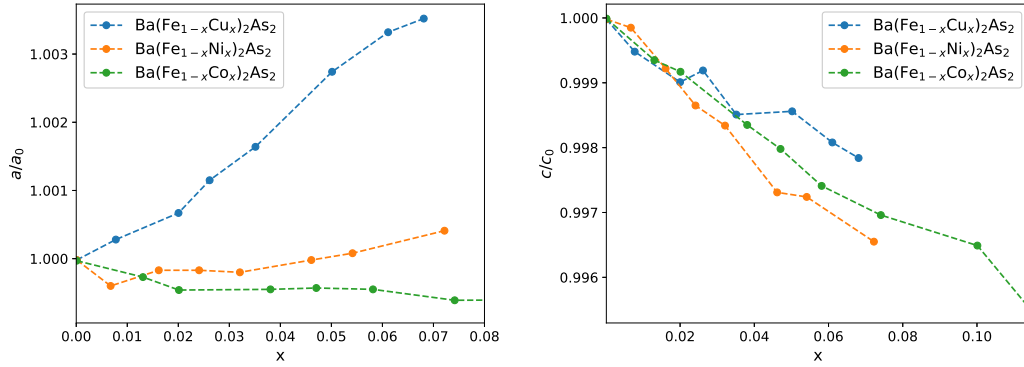


Figure 5.1: Data from reference [46] demonstrates the changes to lattice parameters induced by doping on the Fe site. The c-axis lattice parameter reduces at the same rate, regardless of the difference in number of valence electrons, whereas the a-axis shows marked difference between Co, Ni, and Cu doping.

DFT studies have proposed that instead of the approximately rigid shift in the Fermi level expected by averaging the extra nuclear charge across the whole system, the additional spin density is localised near the dopant atoms in order to compensate for additional nuclear charge [90], making the term ‘charge doping’ potentially a misnomer. This results in the introduction of sites with increased spin density, rather wild changes in the partial DoS (for Ni-doping, less so for Co) and also provides a candidate for a pair breaking pinning centre like those seen for the case of indirect doping of K on the Ba site [133].

5.1 TEMPERATURE DEPENDENT MAGNETISATION

Magnetic zero-field cooled (ZFC) curves at 0.5 mT were used to estimate the superconducting critical temperature (T_c) for each sample.

Demagnetisation

In Figure 5.2 we present the temperature dependent susceptibility for this series of samples in both field orientations. Most samples reach 80% of the ideal diamagnetic signal in both orientations, except for the underdoped

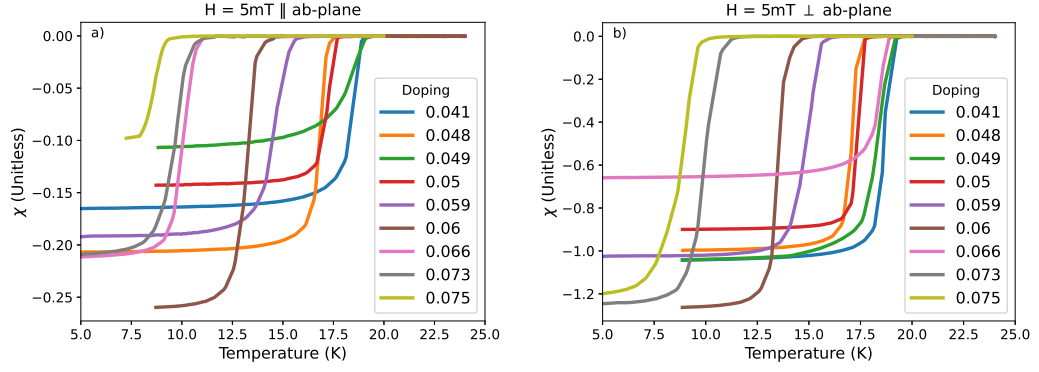


Figure 5.2: ZFC curves of the normalized magnetic moment at 0.5mT for $\text{Ba}(\text{Fe}_{1-x}\text{Ni}_x)_2\text{As}_2$ single crystals with x ranging from 0.041 to 0.066 with the applied field perpendicular to the ab-plane. The superconducting volume fraction of all these samples are $> 70\%$, confirming the presence of strong superconductivity.

and $x = 0.049$ samples.

The susceptibility anisotropy for each sample is presented in Figure 5.3, with error coming from the averaging of two possible formula for the perpendicular demagnetisation factor. Optimally or overdoped samples all present similar anisotropy values, whereas the underdoped sample displays a value approximately double the others.

This is similar to what is seen in $\text{Ba}(\text{Fe}_{1-x}\text{Co}_x)_2\text{As}_2$ where anisotropy develops at the structural transition [101], and also what we have observed in the $\text{BaFe}_2(\text{As}_{1-x}\text{P}_x)_2$ measurements in the previous chapter where we see a change in anisotropy as we increase doping beyond the critical level. The doping level of $x \approx 0.050$ where we see this change occur is, like the phosphorous series, the doping fraction associated with a posited QCP [61].

5.1.1 Transition Temperature versus Doping

Figure 5.4 shows the critical temperature values obtained as a function of doping for this series of crystals. The expected dome shape is observed

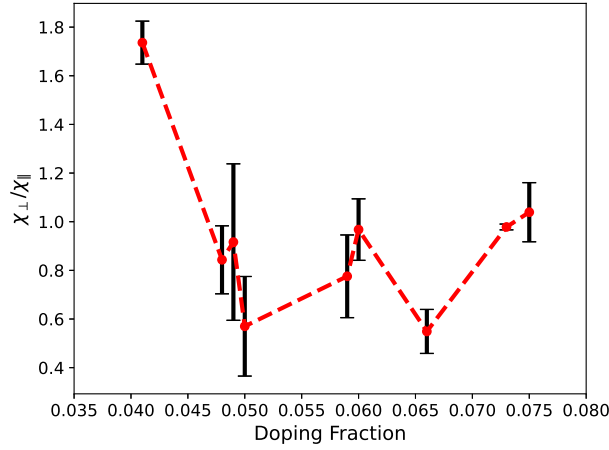


Figure 5.3: Anisotropy in χ below the superconducting transition temperature for each doping. The underdoped presents a significantly larger value to all other samples.

with the peak occurring in the range between $x = 0.041$ and $x = 0.050$. The general consensus of the literature available on $\text{Ba}(\text{Fe}_{1-x}\text{Ni}_x)\text{As}_2$ cites optimal T_c as occurring at a doping concentration around $x=0.05$ [94, 134–136]. We find from these measurements that T_c has very similar values at $x=0.049$ ($T_c = 19.0$ K) and $x=0.041$ ($T_c = 19.15$ K) with the $x=0.048, 0.050$ samples having a lower $T_c = 17.6$ K. Thus, it is difficult to assign an optimum doping concentration at this point for our set of samples. However, for the sake of convenience, we will refer to the $x=0.048$ - 0.050 samples as optimally doped, simply to be consistent with previous reports at this stage. This places these samples in the range of slightly underdoped ($x = 0.041$), near optimally doped ($x = 0.048, 0.049$, and 0.050) to overdoped ($x = 0.059, 0.060, 0.066, 0.073$).

The distinction between underdoped, optimally doped, and overdoped is important to keep in mind. This is because we are interested in observing any signs of quantum critical behaviour in this series, and the different doping fractions result in different proximity to the points of interest, $x = 0.05$ and 0.07 , which have been identified as possible QCPs via NMR measurements [61]. In Figure 5.4 we do not see any obvious signs of anomalous

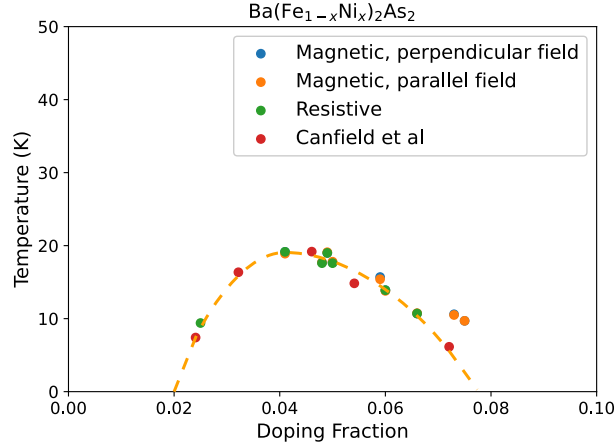


Figure 5.4: Values of T_c taken as T_c -crossover demonstrate the expected dome-like dependence of critical temperature on additional doping. All measurements are this work aside from the red. No significant difference is seen in the determination of T_c for different field orientation or measurement method. Dashed line is a guide to the eye.

behaviour at $x = 0.05$, however we do find that the values of T_c near $x = 0.07$ are significantly above what appears to be the trend. The values of 10.6 K and 9.7 K for $x = 0.073$ and 0.075, respectively, are higher than those obtained in reference [118] ($x = 0.075$, $T_c = 8$ K), and lower than that found in references [134] ($x = 0.070$, $T_c = 13$ K) and [137] ($x = 0.075$, $T_c = 15$ K), illuminating a sensitive dependence of T_c at this doping.

The phenomena of peak T_c values occurring at critical doping values, where normal state transitions are suppressed to 0 K, is observed for a range of superconducting materials. Examples of such materials and transitions include HTS cuprates with their pseudogap behaviour [56], AFM ordering in heavy fermion superconductors [57], or indeed suppression of T_S and T_N to 0 K in the presently studied Ba122 FeSC family [61, 138]. Thus, it is not unforeseen that the posited QCP at $x = 0.07$ is responsible for these values of T_c being larger than expected.

Figure 5.4 also shows the measured values of T_c from another doping dependent study of Ni-Ba122 single crystals by Canfield et al. [6], to show the consistency between these values and ours. Not all phase diagrams of other studies consistently overlap with ours. Studies by Chen et al. [130] and Xu et al. [139] find reasonably higher T_c values on the overdoped side of the phase diagram.

However, this discrepancy can be easily linked to differences in the measurement methods. The estimations by Chen are taken as the point of divergence from χ susceptibility, which would overestimate T_c in comparison to T_c -crossover. Chen et al. also use a different method for characterising the doping levels of their crystals (ICP) whereas Xu et al. quote values as midway through the resistive transition. Canfield et al. use the same EDS method for determination of x , as well as T_c -crossover. This results in values which easily compare to our own. The difference between a resistive, and magnetically derived T_c appears to be negligible as evidenced by our resistive measurements of T_c . Furthermore, there is clearly, as expected, no difference in the T_c obtained for different sample orientations.

It is also worth noting that the values at approximately optimal doping give two significantly different values. At $x = 0.048$ and 0.050 the crossover T_c obtained is 17.6 K, exactly in agreement with that obtained by Shahbazi et al. on single crystals at $x = 0.05$ [136]. The $x = 0.049$ sample has been measured to have a crossover T_c of 19.0 K which is closer to results obtained in another study by Pervakov et al. [134] who found single crystals at the same doping concentration to have $T_c = 19.5$ K.

Upper Critical Field

Figure 5.5 plots values of $H_{c2}(0)$ versus doping taken from a series of resistivity measurements performed on our series of crystals. T_c -crossover was determined for resistivity versus temperature measurements for a range of

fields from 0 to 9 T. Using the simplified Werthamer-Helfand-Hohenberg (WHH) formula [140]:

$$H_{c2}(0) = -0.693 \frac{dH_{c2}}{dT} \Big|_{T=T_c} \quad (37)$$

we are able to obtain estimates for the value of upper critical field for each doping.

The obtained values show a distinct drop off in H_{c2} at the optimal doping of $x = 0.050$. Estimations of the H_{c2} behaviour is closely linked to the condensation energy, and coherence length of each sample and will thus have flow on effects for the efficiency of flux pinning in the material, as well as its ability to screen incident fields in the first place.

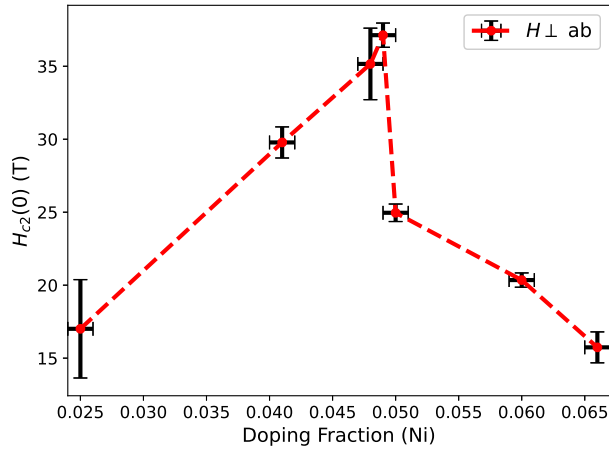


Figure 5.5: Measurements of T_c as a function of H in a) allow the determination of approximate values of $H_{c2}(0)$ by utilising the WHH approximation (equation 37). A clear drop off in H_{c2} can be seen to occur at the critical doping $x = 0.050$.

5.2 CRITICAL CURRENT DENSITY VERSUS APPLIED FIELD

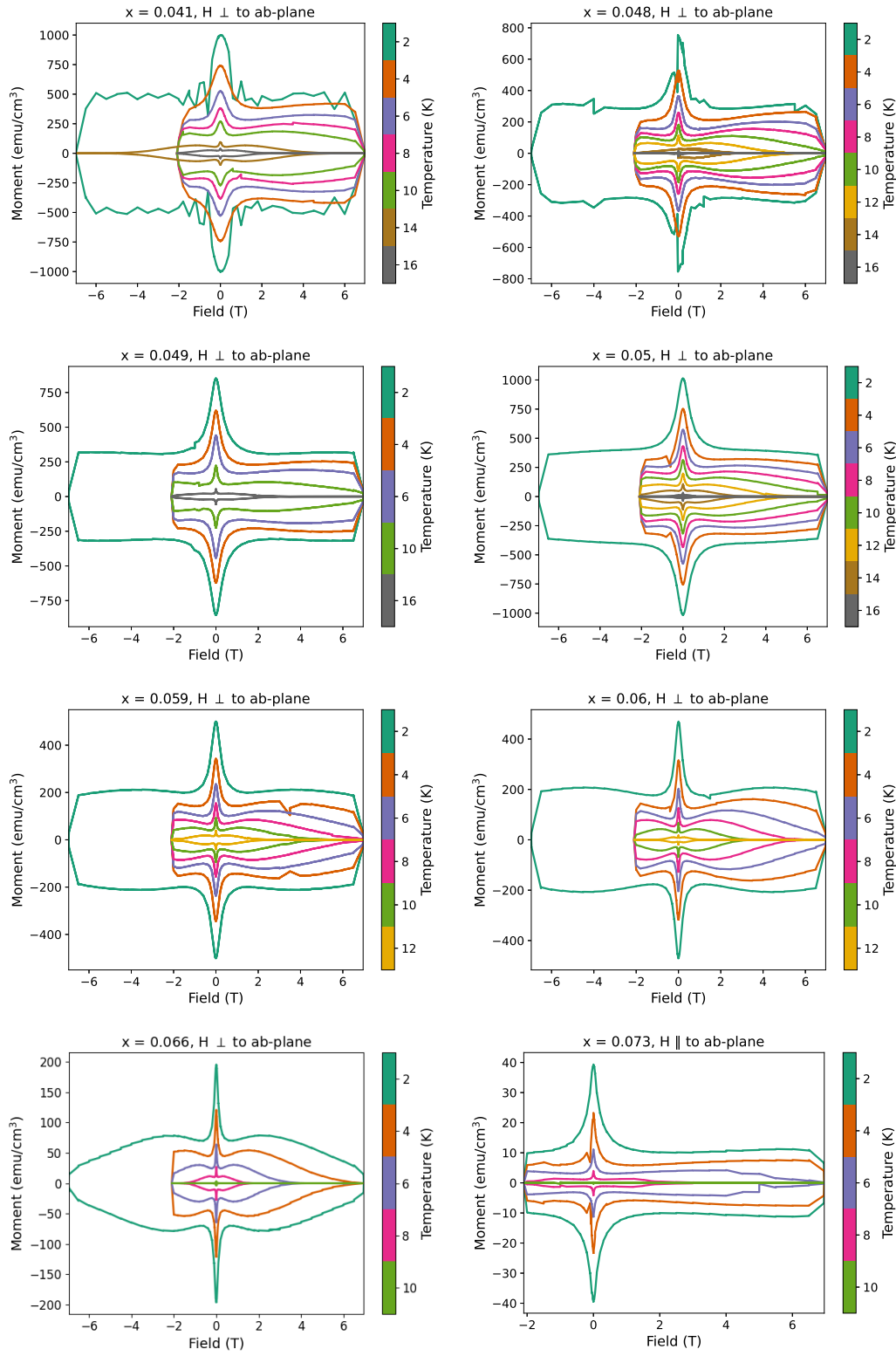


Figure 5.6: Hysteresis loops for each sample ranging in doping from $x = 0.041$ (underdoped) to $x = 0.075$ (overdoped) for field oriented perpendicular to ab -plane. Second magnetisation peak is clearly visible at all temperatures for all samples.

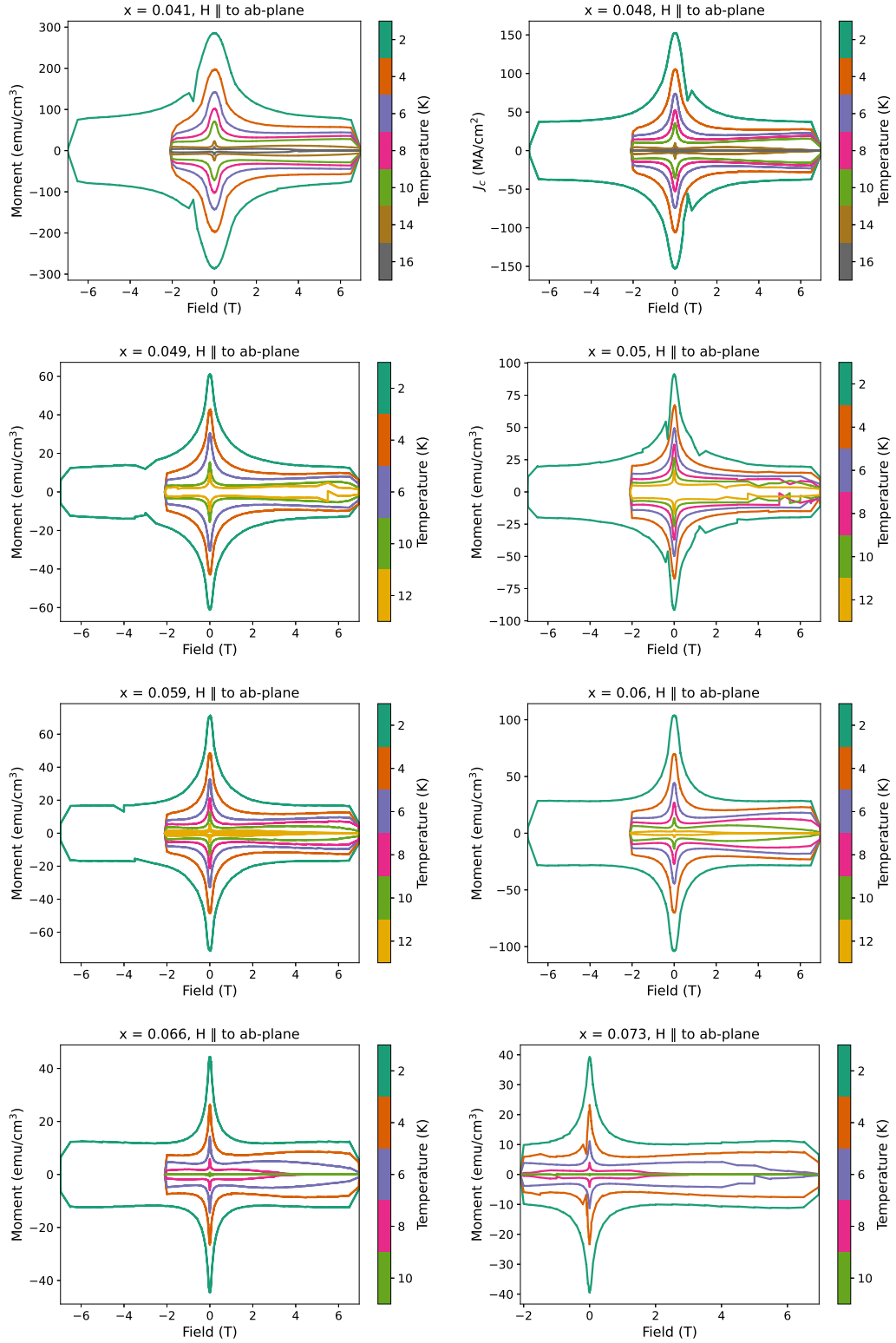


Figure 5.7: Hysteresis loops for each sample ranging in doping from $x = 0.041$ (underdoped) to $x = 0.075$ (overdoped) for field oriented parallel to ab-plane. Second magnetisation peak is definitely diminished in comparison to the perpendicular orientation at low temperatures.

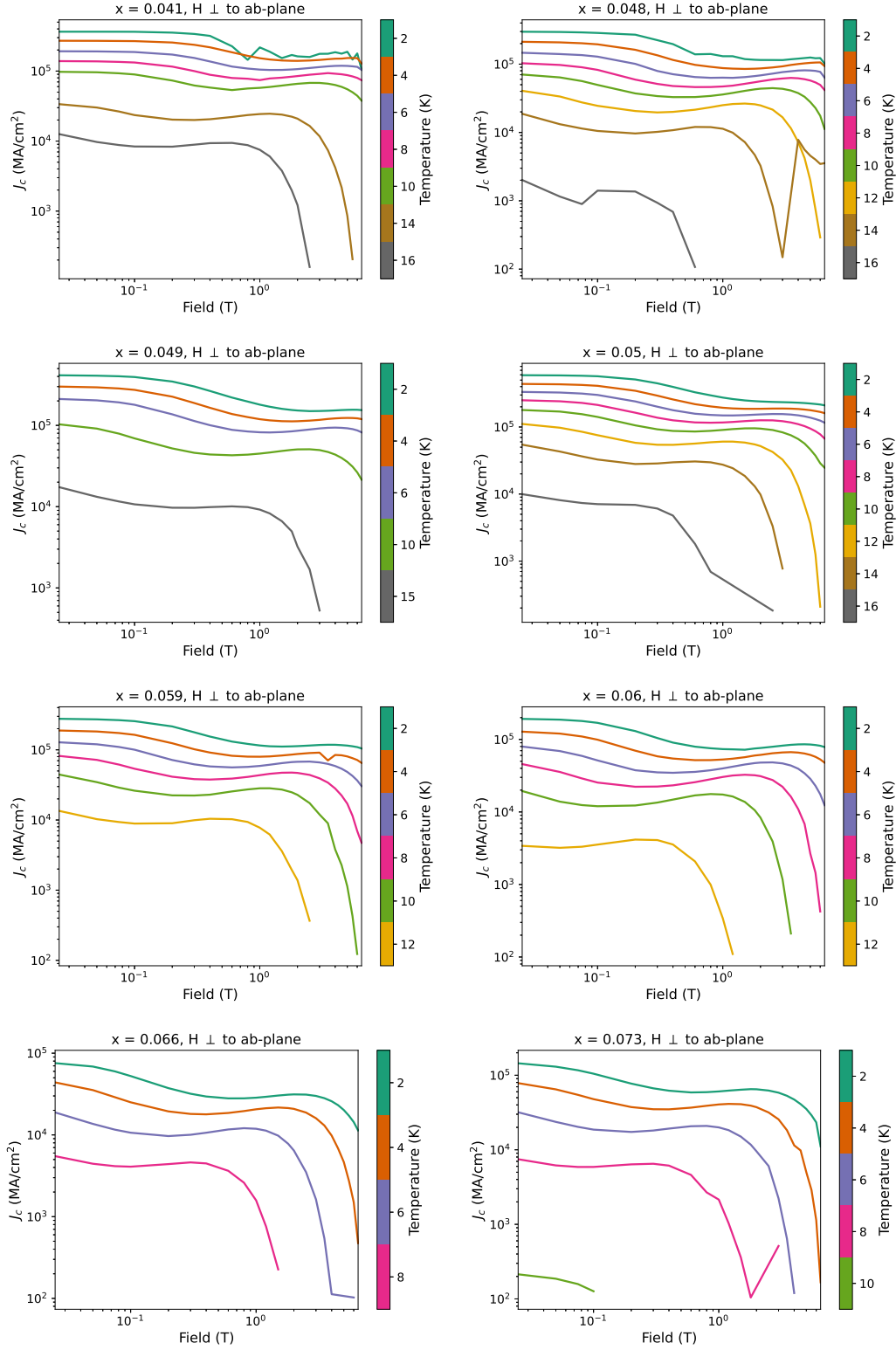


Figure 5.8: Critical current density estimated from the magnetisation loops in Figures 5.6 and 5.7 using the Bean model. Values reach as high as 0.5 MA/cm² in the optimally doped $x = 0.050$ sample. The shape of the field dependence splits into four regions related to single vortex pinning (I and II), collective pinning (III) and flux flow regions (IV) illustrated in Figure 4.7.

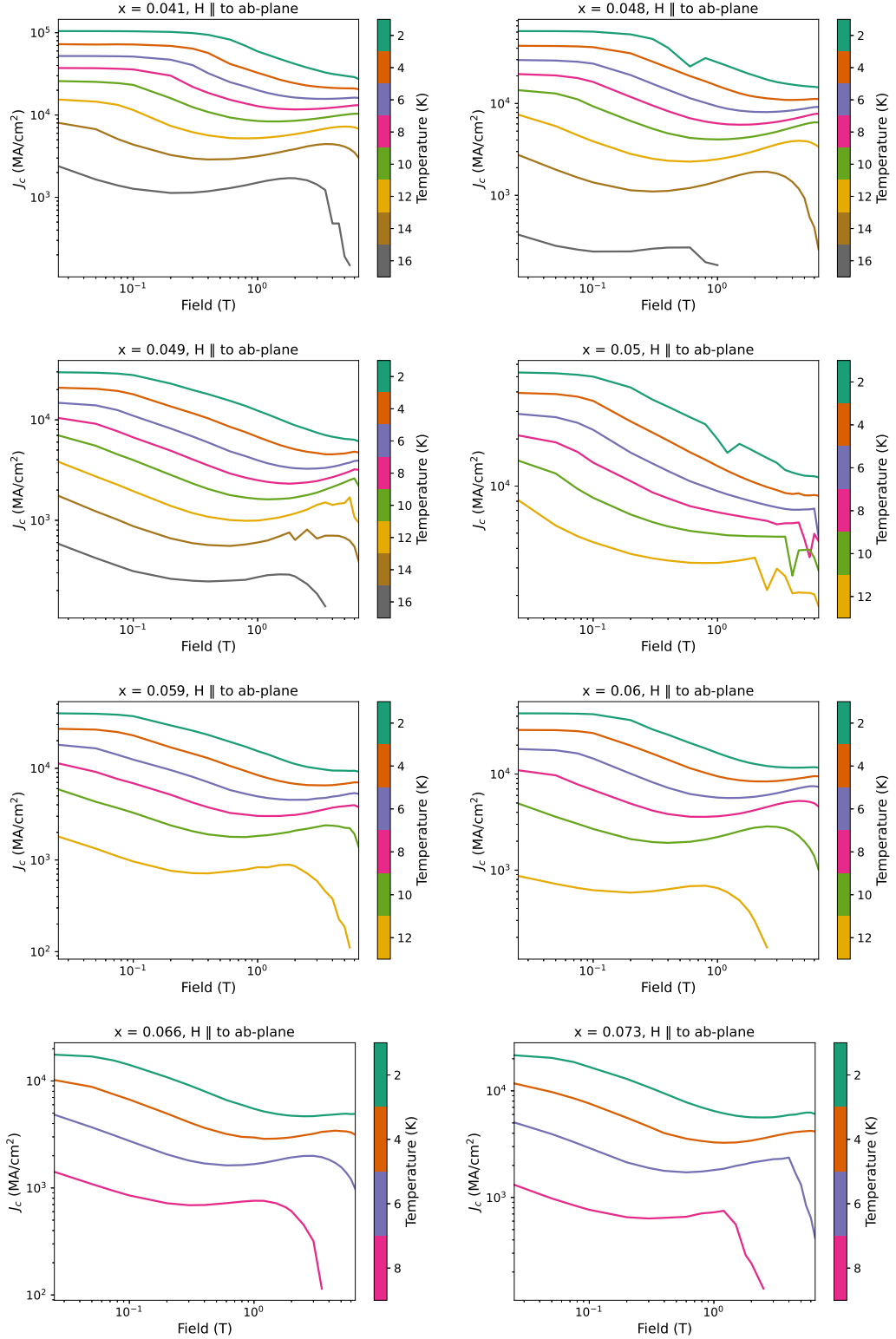


Figure 5.9: Critical current density estimated from the magnetisation loops in Figures 5.6 and 5.7 using the Bean model. Values are much lower in the parallel orientation due to intrinsic anisotropy in the superconducting characteristics, as well as changes in the flux pinning induced by different geometries as discussed further on. The shape of the field dependence splits into four regions related to single vortex pinning (I and II), collective pinning (III) and flux flow regions (IV) illustrated in Figure 4.7.

Values of J_c were obtained via the same methods presented as in the previous chapter. Measuring hysteresis loops for each sample in applied fields ranging from 0 to 7 T, temperatures from 2 K up to just below T_c , and each performed separately in fields oriented perpendicular and parallel to the ab-plane. The hysteresis data from these measurements can be seen in Figures 5.6 and 5.7, and the data processed via the Bean model is presented in Figures 5.8 and 5.9.

Second Magnetisation Peak (SMP)

The field dependence manifests as very similar to what has been observed in other studies of $\text{Ba}(\text{Fe}_{1-x}\text{Co}_x)_2\text{As}_2$ samples [112], with the prominence of the SMP increasing with increasing doping fractions. In $\text{Ba}(\text{Fe}_{1-x}\text{Ni}_x)_2\text{As}_2$, the fishtail effect has been quite concretely experimentally linked to a crossover in pinning behaviour via magnetic relaxation rate measurements [137].

The details of what is meant by this pinning crossover is detailed in the lengthy review of vortex dynamics in reference [15], and in a more narrow focus in reference [113]. In short, the elastic regime is defined for weak collective pinning, where the elasticity is the key force to balance with pinning forces. The crossover is triggered by a reduction in elasticity of the vortex resulting in the possibility of plastic deformation, where single vortex pinning by strong pinning defects become the dominant contribution.

In all the $\text{Ba}(\text{Fe}_{1-x}\text{Ni}_x)_2\text{As}_2$ samples, the SMP begins shortly after the onset of collective pinning, and before the onset of motion of vortex bundles. This contrasts with what was seen in the $\text{BaFe}_2(\text{As}_{1-x}\text{P}_x)_2$ crystals where, in some measurements, the SMP reappeared after the sharp drop in J_c associated with vortex bundle dissipation.

The change in orientation ubiquitously moved the SMP to higher fields, meaning that the weak collective pinning dominates for longer. This could be contributed to postponing the reduction in vortex elasticity, increasing the significance of intervortex interactions, or changing the pinning volume through which a vortex can deform to interact with pinning available centres. One other possibility is that the orientation of the vortices changes the curvature a vortex can attain when deforming to nearby pins, potentially due to a change in the density of pins in the transverse direction.

5.2.1 J_c versus Doping

Once we had finished the determination and characterisation of the superconducting transitions in this series of samples, the next step was to investigate the critical current phase diagram of nickel doped Ba122.

Figure 5.10 shows the final product, and the central result of this chapter; a sharp peak in the critical current density of Ni-Ba122 occurring at the optimal doping value of $x = 0.050$. This result was published in Superconducting Science and Technology [141], and has since also been observed by other groups also measuring J_c as a function of nickel doping [118].

Large increases in J_c are always of interest to the superconducting community, however, potentially the more immediately interesting feature of this data is that this peak only occurs when the samples ab-plane is perpendicular to the applied field.

The peak in J_c occurs somewhere close to the critical doping at $x = 0.050$ whereas the peak in T_c appears to be between 0.050 and 0.041. It has been pointed out in reference [112] that this peak behaviour in J_c is consistent with an enhancement of the vortex energy near a QCP.

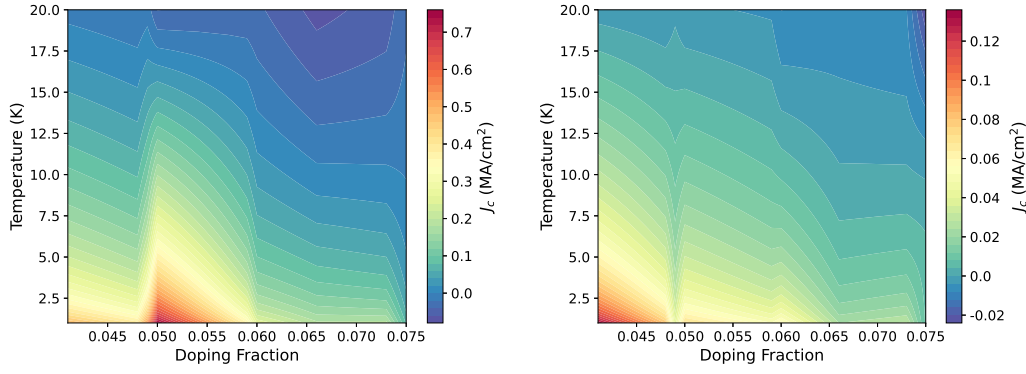


Figure 5.10: A peak in the doping dependence of J_c can be clearly discerned near optimal doping for magnetic measurements in $H \perp$ to the ab-plane (top), but not in the orientation with $H \parallel$ ab-plane (bottom).

This observation, in conjunction with the lack of a correlated peak in T_c , points to the pinning characteristics being the chief culprit for the large values of J_c and thus we will present Dew-Hughes geometrical, and strong/weak collective pinning models in order to ascertain the nature of pinning in our crystals and subsequently why we see such marked difference between the two orientations.

5.3 PINNING ANALYSES

The existence of this peak in the doping dependence J_c is highly likely to be related to the pinning characteristics of the material. Thus, the remainder of this chapter is devoted to presenting various analyses of the pinning behaviours. This follows three main avenues; application of the Dew-Hughes model, the characteristics of the strong pinning power-law regime, and temperature dependent pinning models.

5.3.1 Dew-Hughes

Figures 5.11 and 5.12 show the pinning force density ($F_p = J_c \times H$) normalised to its maximum value plotted as a function of the reduced field (h

$= H/H_{\text{irr}}$). For each sample, most of the measurements had H_{irr} fall outside of the accessible field range, and thus the data presented is only for temperatures close to T_c . Data from as many temperatures as possible are plotted based on whether a value for the irreversibility field was able to be obtained from the criteria that H_{irr} is equal to the field at which J_c is reduced to less than 1000 A/cm^2 .

The model utilises a definition of pinning force which takes into account only the amount of force required to move a vortex from a pinned to unpinned position, regardless of intricacies which would arise, most notably from things like the elasticity of said vortex. Nonetheless, the Dew-Hughes model [14] has become one of the standard models implemented in order to characterise the nature of a pinning mechanism in superconducting samples. So we will find it useful in order to compare to literature.

Note that this does not mean it we would not see differences in materials with different elastic moduli, just that an interpretation in this model would be incorrect. Even so, the Dew-Hughes model is used to discern between the proposed geometry of available pinning centres, the nature of the interaction mechanism (core or magnetic interactions), and whether the pinning centres result from non-superconducting conclusions or superconducting regions of contrasting values of the Ginzburg-Landau parameter (κ)

Perpendicular field

For samples in the perpendicular field orientation each doping and temperature agree well with a single fitting of the form $f_p = Ah^a(1-h)^b$ at low applied fields. The calculated maxima $h_{\text{max}} = a/(a+b)$ agrees well those obtained by studies on other iron arsenide materials. Previous studies have found h_{max} values to be between 0.32-0.4 for $\text{Ba}(\text{Fe}_{1-x}\text{Ni}_x)_2\text{As}_2$ [134, 135], 0.32-0.41 in $\text{Ba}(\text{Fe}_{1-x}\text{Co}_x)_2\text{As}_2$ [112, 142], 0.28 in $\text{Ba}(\text{Fe}_{1-x}\text{Na}_x)_2\text{As}_2$ [143].

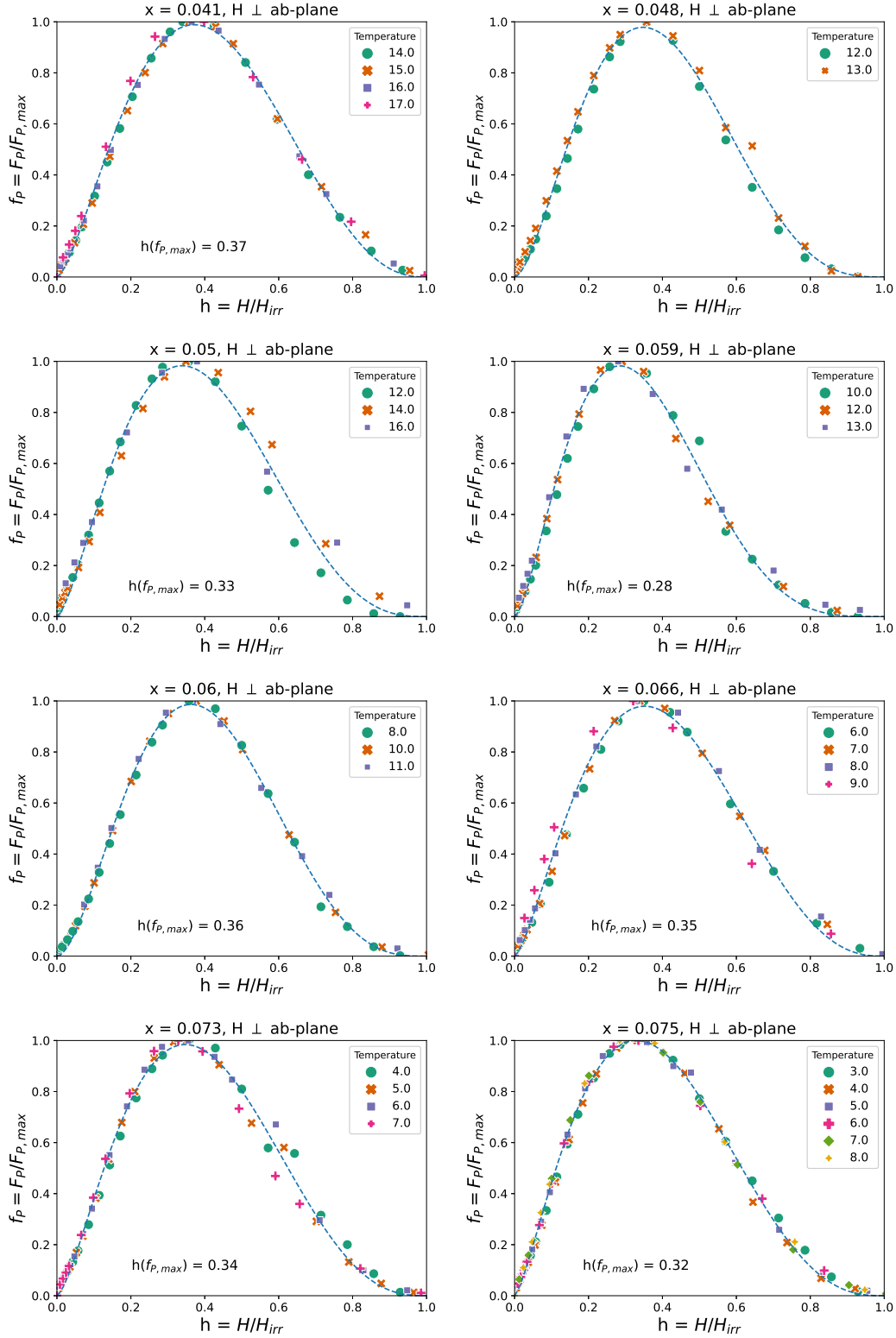


Figure 5.11: Dew-Hughes fits to each sample show peak positions independent of the temperature, when measurements are taken in the perpendicular field orientation.

All those previous studies cited above exhibit reasonably consistent values of h_{max} over a significant doping range. The study by Pervakov et al. [134] even found the data to scale convincingly over a large temperature range in their $\text{Ba}(\text{Fe}_{1-x}\text{Ni}_x)_2\text{As}_2$ samples ($T = 1.4\text{-}7.9$ K for $x = 0.07$, $T = 7\text{-}17$ K for $x = 0.05$) demonstrating that these results are only minorly affected by the elastic-plastic crossover. Values of h_{max} obtained in reference [137] are a bit lower, ranging from 0.26-0.3 over a similar doping range to our samples.

Whilst this is promising we do observe that data from different temperatures begins to spread when the applied field is past h_{max} . We believe this observation can be attributed to the existence of the second magnetisation peak as the plastic and elastic regimes will have different field dependencies, and the position of the SMP is temperature dependent.

So, apart from the slight divergence at high fields, all of these data points converging onto the one line in the perpendicular orientation is strong evidence that the nature of this pinning mechanism is independent of both temperature and doping concentration. In the context of the Dew-Hughes model, the obtained values of h_{max} (0.32-0.4) are correlated with either a core mechanism with point type geometry, or a magnetic interaction with volume type geometry [14].

Parallel field

In field parallel to the ab-plane, the Dew-Hughes results are strikingly different. The movement of the second magnetisation peak to higher fields in this orientation makes attaining a value for H_{irr} more difficult and, for this reason there are no plots for the $x = 0.041$ and 0.073 samples.

Figure 5.12 depicts several distinct differences in the model outcome for the parallel field orientation. The values of h_{max} are being shifted significantly

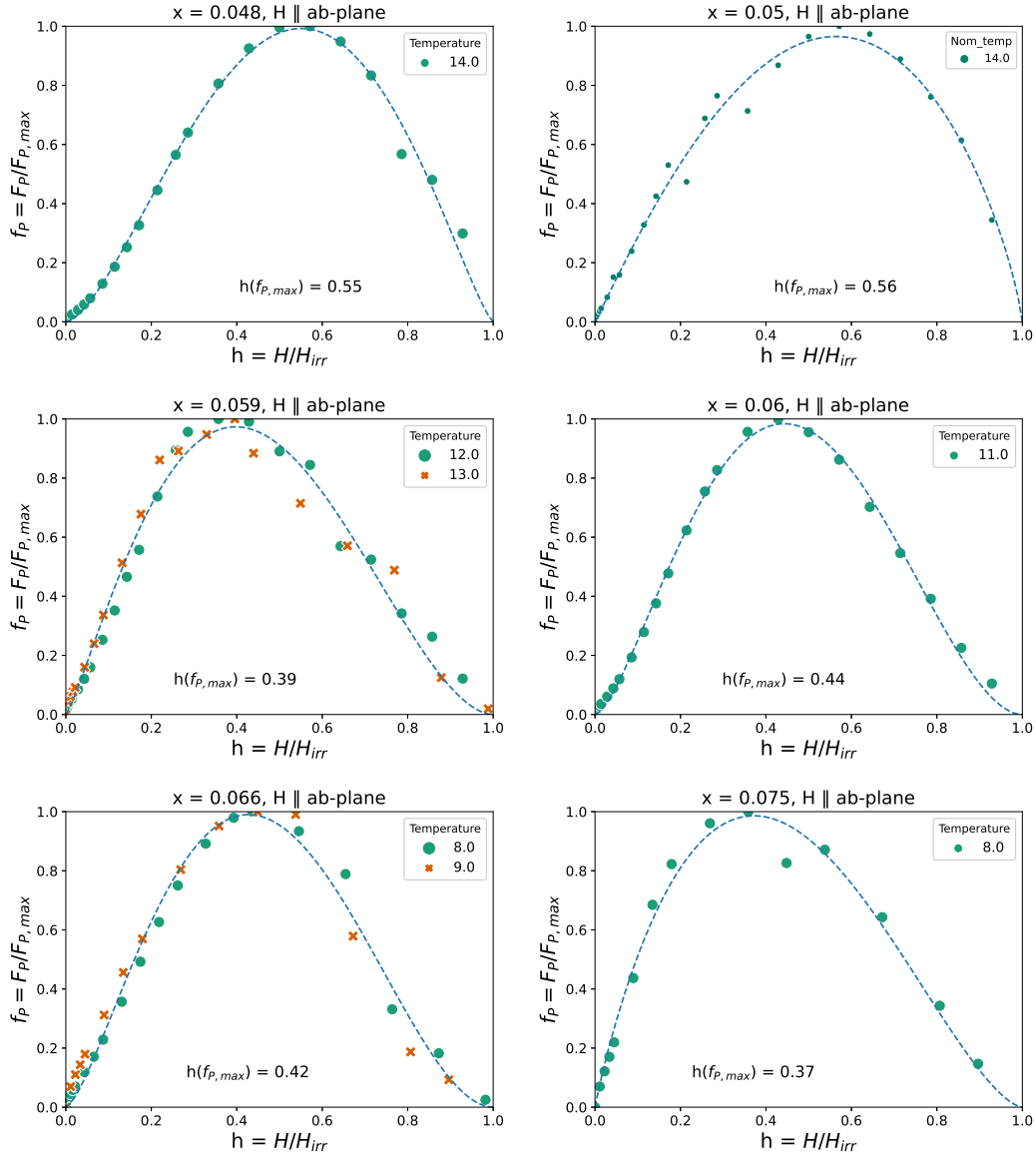


Figure 5.12: Dew-Hughes fits show a wide range of peak positions. The samples in parallel orientation had lower values of J_c which persisted to larger fields, resulting in more difficulty obtaining values for the irreversibility fields and thus less data for these plots. Two dopings, $x = 0.041$ and 0.073 , had data which was too noisy at the higher temperatures to obtain reliable fits.

higher in the parallel orientation for some samples, but not all. This fact points to a different form of pinning contributing significantly in this orientation, and contributing differently, dependent on the doping fraction.

Another study by Pervakov et al. [134] also found this shift in the pinning force density maximum for $\text{Ba}(\text{Fe}_{1-x}\text{Ni}_x)_2\text{As}_2$ single crystals, attributing it, as we have also, to a difference in pinning for vortices moving within or between layers, each of which will have different field dependencies. In parallel orientation, the induced currents circle in the ac (or bc) plane, and will thus have a contribution from the currents running parallel to the c-axis, which would not be seen for currents induced in the ab-plane.

However, our data shows us something more in that this effect seems to increase in significance around optimal doping. This is immediately significant to us as it verifies a distinction between orientations for the dominant pinning mechanism near our observed peak in J_c .

The h_{max} values for the optimally doped samples are 0.55 and 0.56, shifting towards the value 0.6 associated with a core pinning mechanism and a surface geometry. This seems reasonable, as the point pinning centres providing the major contribution in perpendicular orientation are likely created at dopant sites in the Fe-As plane which would appear as a surface for vortices oriented parallel to these planes.

When looked at side by side, in Figure 5.13, it is also easy to discern that there is a broadening of the peak in pinning force density. This can also be interpreted as resulting from the two pinning mechanisms being present, with two different values of h_{max} contributing to spreading out the field dependence of F_p .

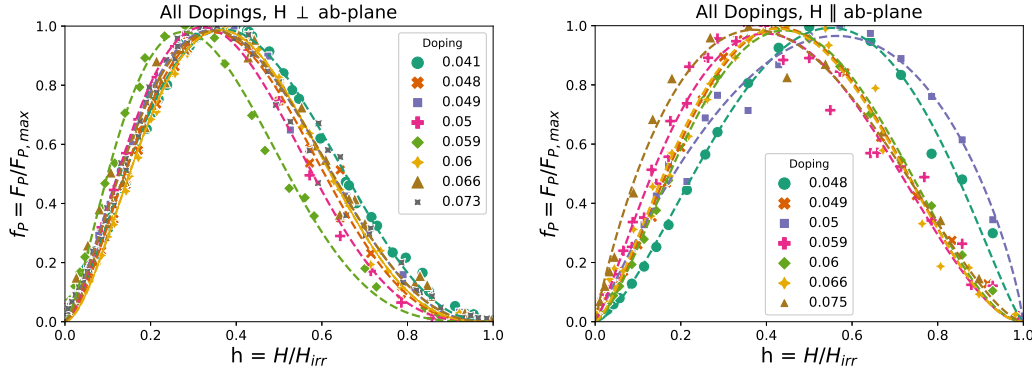


Figure 5.13: A plot of normalized pinning force density versus reduced field for a range of dopings and temperatures. The red line represents a fit of the form $f_p = Ah^a(1-h)^b$ taken from the Dew-Hughes model [14] for vortex pinning in type 2 superconductors. The scaling behaviour indicates a strong pinning mechanism with little to no temperature or doping dependence in perpendicular field orientation but not parallel.

This observation begins to form a coherent interpretation when combined with the ZFC curves in Figure 5.2. The breadth of superconducting transitions is larger in the parallel field orientation, indicative of an increase in the significance of weak-links. This means that the majority of weak-link behaviour is being contributed to by currents moving parallel to the c-axis and that pinning in this direction is weaker. This will return lower values of J_c in parallel orientation, and highlights the significance of surface pins in this orientation.

To further back up this interpretation, note that vortex lines will not need to deform in order to reach more pinning sites as the vortex is oriented such that its entire length is pinned by the surface. This would result in an elongated single vortex regime due to the significantly diminished pinning volume, an effect which can be very clearly seen when comparing the power law fits of the 0.05 sample in perpendicular and parallel orientation:

Figure 5.14 clearly shows the parallel orientation (left) resulting in a power law region up to almost 3 T whereas the perpendicular orientation (right) is finished with such a dependency observably before reaching 1 T. One

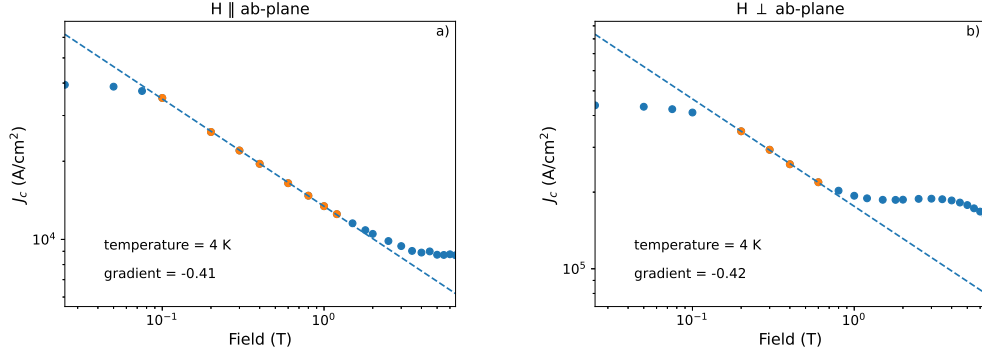


Figure 5.14: The difference in pinning between perpendicular and parallel field orientations result in a single vortex regime that extends to higher fields in parallel.

other possible effect of this dynamic would be to reduce intervortex interactions, shifting field at which we attain the reduction in flux-line elasticity responsible for the manifestation of a second magnetisation peak.

5.3.2 Strong Pinning

Next we present the result of power-law fits to Region II in order to provide us with information about the strength of pinning centres in the single vortex regime. In particular, this analysis tells us how well our measurements adhere to the strong-pinning described in [15, 20, 23, 115]. Figure 5.15 shows a representative fit to this region for our optimally doped sample.

Ishida et al. point out, that in $\text{Ba}(\text{Fe}_{1-x}\text{Co}_x)_2\text{As}_2$ single crystals, there is a coexistence of δT_c and δl pinning, with δT_c dominating at high temperatures, and δl contributing at low temperatures [112]. Thus, we expect to see in this analysis pinning associated with scattering off doping impurities.

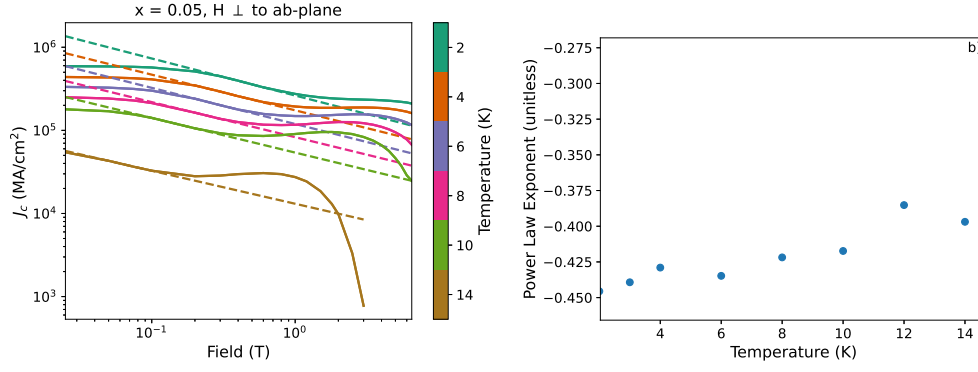


Figure 5.15: Log-log plots of the field dependence of J_c for different temperatures, with dashed lines representing a power-law fit to the proposed 'strong pinning' regime (a) and the resultant power law exponents as a function of temperature for the $x = 0.050$ optimally doped sample (b).

Perpendicular Field

In perpendicular field, at 2 K, we find a value of 0.45 for the strong pinning exponent (μ of the optimally doped sample ($x = 0.050$), and a small but definitive trend towards a lower magnitude at higher temperatures, in reasonable agreement with values obtained in reference [144]. The value at 2 K is lower than that obtained for the $\text{BaFe}_2(\text{As}_{1-x}\text{P}_x)_2$ crystals in the previous chapter, which was related to inhomogeneity in the local T_c . Thus, this data insinuates a dominant contribution to pinning at low temperatures which is not of δT_c type, but δl .

The formulation of strong pinning theory in reference [23] calculates that, when taking into account the possibility of vortices becoming pinned via long-range interactions, as opposed to head-on collisions, μ should have a value of $-5/8$ [23].

This information is more striking when looking at Figure 5.16, which shows how μ evolves with doping in perpendicular field. We see the same behaviour as seen in the $\text{BaFe}_2(\text{As}_{1-x}\text{P}_x)_2$ crystals, with μ clearly increasing when moving through the optimal doping. In $\text{BaFe}_2(\text{As}_{1-x}\text{P}_x)_2$ this was

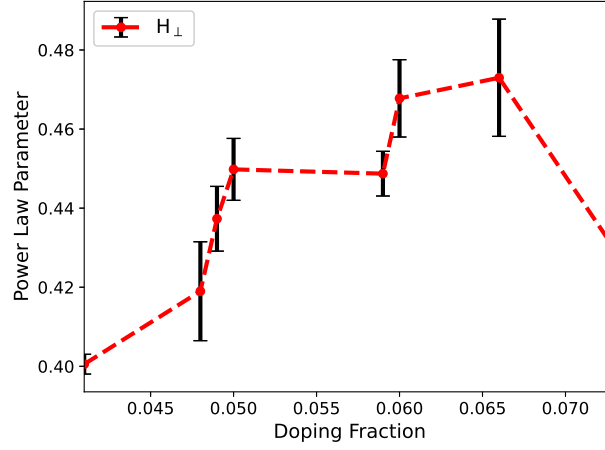


Figure 5.16: From measurements in perpendicular orientation, values of the power-law exponent (μ) increase as we reach the doping $x = 0.050$ associated with our peak in J_c . The underdoped sample returns a value incommensurate with strong pinning (0.4), which then increases towards the value $\mu = 0.5$ indicative existing strong pins.

correlated with an increase in the vortex core energy leading to stronger pinning and consequently, a higher value of J_c . Considering $x = 0.050$ is also a posited QCP, this appears to be evidence for the same mechanism occurring in our $\text{Ba}(\text{Fe}_{1-x}\text{Ni}_x)_2\text{As}_2$ material.

To further illustrate this point, we can interpret some of the data from our H_{c2} measurements. Figure 5.17 illustrates the change in ξ derived from transport measurements via the dirty limit of the WHH approximation [140].

The pinning energy derived in [20] is of the following form:

$$u_p \approx 2b_z \epsilon_0 \ln(b/\xi) \quad (38)$$

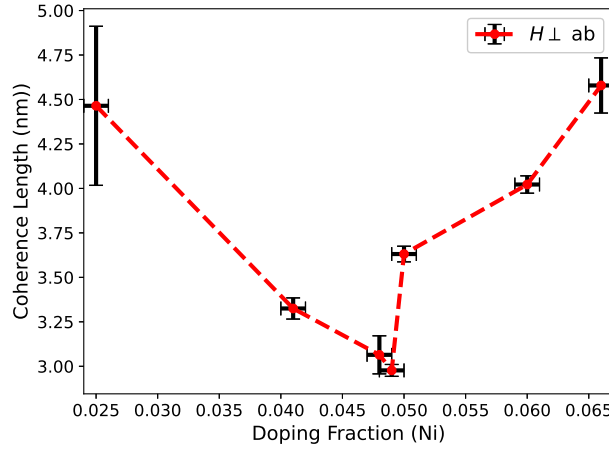


Figure 5.17: One interpretation of the difference in pinning behaviours could be linked to the observed change in coherence length with doping. The value can be seen in this figure to jump at the doping associated with the peak in J_c , and will result in a larger trapping volume and thus stronger pinning.

The maxima in H_{c2} occurring at optimal doping can be related to ξ via the GL definition of H_{c2} :

$$H_{c2} = \Phi_0 / 2\pi\xi^2 \quad (39)$$

meaning an decrease in ξ and thus a larger pinning energy. Assuming the size of pinning defects remains the same amongst all dopings, then this is indicative of stronger pinning occurring near optimal doping.

Parallel Field

In parallel field we find the opposite trend, when compared to Figure 5.16. In the underdoped sample, pinning begins acting significantly like the $\text{BaFe}_2(\text{As}_{1-x}\text{P}_x)_2$ samples, with μ indicating long-range strong pinning centres being the major contributor. However, this contribution is suppressed significantly when moving towards optimal doping.

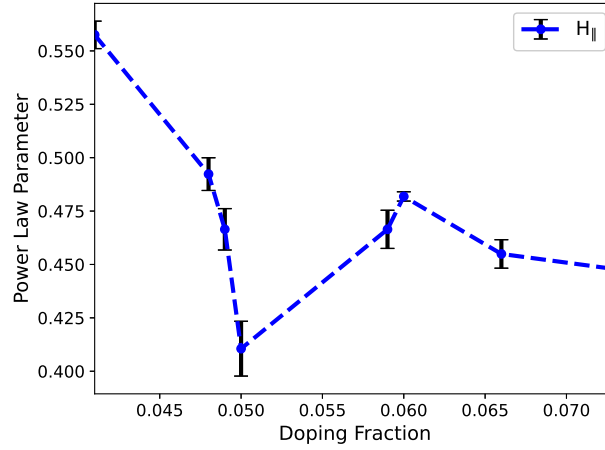


Figure 5.18: In parallel orientation, we observe the opposite trend to that observed in Figure 5.16. The increase in strength of individual pinning centres leads to an increase in contribution from the surface pins revealed in our Dew-Hughes analysis. This plot shows that these surface pins do not act as strong pinning cites.

This, in conjunction with Figure 5.16 clearly demonstrates a transition in the dominant pinning mechanism near $x = 0.050$. This transition results in an increase in the contribution from strong pinning centres in perpendicular orientation, and a decrease in parallel orientation. We posit that this change in the pinning behaviour is what results in the observed sharp peak in J_c .

5.3.3 Temperature Dependent Pinning

The other common source of theory for evaluating the nature of pinning in superconducting materials is reviewed in the very comprehensive work of Blatter et al. [15]. Starting from GL-theory free energy functionals and equating pinning forces with applied Lorentz forces and elasticity of pinned flux lines, Blatter provides a comprehensive overview of the effect of pinning over a range of different parameter regimes with the key aspects being the ‘strong’ or ‘weak’ nature and density of available pinning regimes to re-

sult in, amongst other things, the expected temperature dependence of J_c characteristics for two distinct types of pinning.

To this end, we have followed the procedure of a number of different authors to determine what this can tell us about our sample's behaviours. The standard approach involves taking the result of the general inversion scheme outlined in [145]:

$$J_c(T, B) = \left(\frac{J_c(T, B)}{J_c(0, B)} \right)^p G(T) \quad (40)$$

where $G(T)$ is a thermal function dependant on the dimensionality, vortex pinning and creep regimes for a given superconductor [24].

Combining this with the result from Griessen et al. which describes the different forms of $G(T)$ for two distinct types of pinning which, as previously described, arise as a result in local inhomogeneities of the mean free path of charge carriers or the local T_c . This results in two forms of the temperature dependence of J_c for the two possible types of pinning referred to as δl , and δT_c at a given field. This analysis, to be clear, is only valid in the single vortex regime of a crystals field dependence.

This model has proven effective with low field J_c measurements in well-known superconducting materials such as YBCO [24] and MgB_2 , [79] but not so well in FeSCs, as shown in a study by Vlasenko et al., who compiled various attempts at fitting this model to 122 and 11 samples [146]. See, for example, Figure 5.19 showing the attempted fitting of our data to this model at low fields.

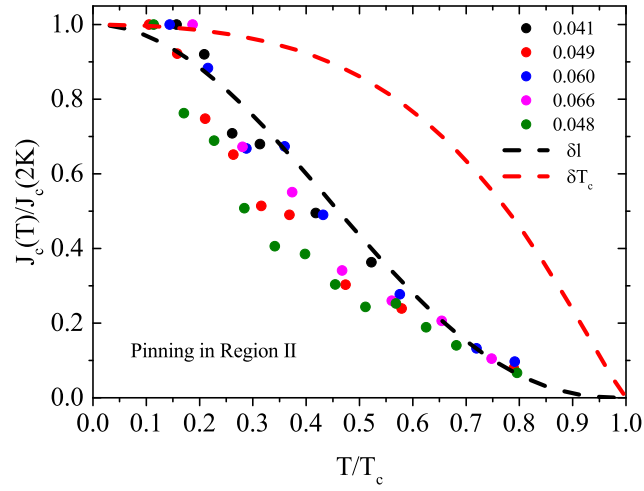


Figure 5.19: Plot of reduced J_c vs reduced temperature. The dashed lines represent theoretical models of vortex pinning dependent on local variations in T_c (red) and mean free path (black), referred to as δT_c and δl , respectively.

When briefly examined this null result makes a lot of sense. The strong temperature dependence of the pinning regime delineated as above in our field dependent J_c plots makes it abundantly clear that, for a given field, we are traversing very different regimes in vortex dynamics, and most significantly, will definitely be entering regimes beyond single vortex pinning where this model is applicable. Thus, more care is needed when utilising this analysis for our purposes.

So, instead of attempting to immediately insist our data falls on the line of a specific type of pinning, we will first attempt to see how our data fits to a more general equation of the form:

$$J_c(T)/J_c(0) = (1 - t^2)^p(1 + t^2)^q \quad (41)$$

where t is the reduced temperature $= T/T_c$

When plotting our critical current measurements as a function of $1 - t^2$ for very low applied field of $\chi = 0.050$ mT we obtain Figure 5.20 for three of our samples, one taken from the underdoped, optimally doped and overdoped region of the parameter space:

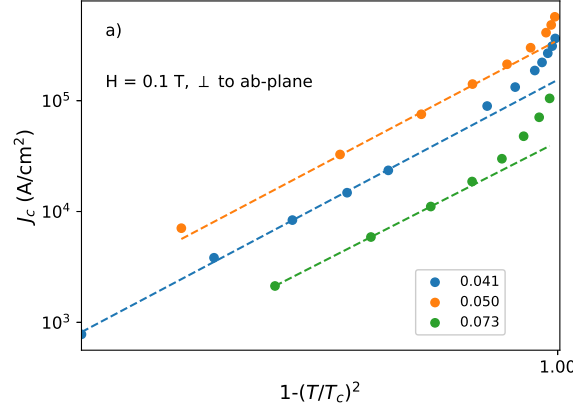


Figure 5.20: Linear fits to low temperature data reveals an adherence to equation 41 dependent on field orientation. This figure demonstrates fits for a representative from each region of the doping phase diagram. The values of the gradient obtained from these fits from all samples ranges between 1.92-2.58 where 2.5 is indicative of δl pinning, and $7/6$ is indicative of δT_c pinning.

The samples show a good agreement with this fitting expression at higher temperatures and in perpendicular field, manifesting as a linear fit when plotted in this fashion. The divergence towards low temperatures arises simply due to the fact that the two factors in the fitting expression become asymptotic to one another as t tends to 0, i.e. this is a mathematical feature rather than one integral to the nature of our material.

As we increase the applied field, the linear section of these plots becomes smaller and smaller as we push the measurements beyond the parameter space where single vortex pinning can be assumed, i.e. at high fields and high temperatures. For the equivalent data in the parallel orientation, it was clear that no such trends can be reliably assumed,

From these fits we are able to extract values for the exponent p in Equation 41, with the value of 2.5 corresponding to δT_c , and $7/6$ corresponding to $\delta l_{\text{pinning}}$. The values of p obtained ranged between 1.92 - 2.58 for the range of samples, with no obvious monotonic dependence on doping fraction. This result is strongly indicative of the coexistence of both forms of pinning, with a dominance of δl pins.

5.4 CONCLUSION

We have found a peak in J_c at the optimal doping of a series of $\text{Ba}(\text{Fe}_{1-x}\text{Ni}_x)_2\text{As}_2$ single crystals. This peak is only seen when the applied field in our magnetic measurements is applied perpendicular to the ab -plane, meaning that all screening currents are circulating in-plane and also, that vortices penetrating the sample at higher fields are oriented along the c -axis.

The application of the pinning model of Dew-Hughes show several things. First, pinning is dominated by a point-like core type pinning mechanism in perpendicular field, consistent across the doping phase diagram. Values of the strong pinning parameter, μ , increase at optimal doping, indicative of an increase in the pinning strength, which corresponds with a minima in ξ at this doping fraction. We believe this is indicative of the same form of peak in the vortex core energy which is seen in the $\text{BaFe}_2(\text{As}_{1-x}\text{P}_x)_2$ material [60].

In parallel field, this observation is flipped, with Dew-Hughes plots demonstrating a shift in the peak of pinning force to pins with a surface geometry near optimal doping. This corresponds to the same pinning centres, introduced at the dopant sites in the Fe-As planes, which appear as a surface for vortices oriented in the ab -plane. In terms of the strong pinning parameter, the shift in pinning geometry coincides with a large dip in μ , showing that the same transition which results in stronger pinning for the perpendicular

orientation, shifts the dominant pinning contribution to the surface pins which do not act as a strong pin and thus, return lower values of J_c .

Thus, the peak in J_c observed at optimal doping has been shown to be a phenomena stemming from changes to the pinning force characteristics of $\text{Ba}(\text{Fe}_{1-x}\text{Ni}_x)_2\text{As}_2$ with doping, rather than amelioration of the basic superconducting parameters such as T_c .

PRESSURE DEPENDENT PROPERTIES OF Ba(Fe_{1-x}Ni_x)₂As₂ SINGLE CRYSTALS

Now that we have established some fundamental aspects of J_c and flux pinning as a function of doping in Ba(Fe_{1-x}Ni_x)₂As₂ we will begin to explore the effect of applied hydrostatic pressure on our series of crystals.

From the previous chapter we have seen that there are two separate forms of pinning present in Ba(Fe_{1-x}Ni_x)₂As₂, a point-like contribution and a surface pinning contribution, each of which contribute to different degrees, dependent on the doping and orientation of the sample. The peak in J_c at $x = 0.050$ is correlated with a peak in the pinning strength of these point core-like pinning centres, which is not as effective in parallel orientation due to the increased contribution from the surface pins.

The fact that our peak in J_c coincides with an increase in the strength of these pinning centres and a minima in coherence length is very reminiscent of quantum critical behaviour, such as the peak in vortex core energy observed in BaFe₂(As_{1-x}P_x)₂ [60]. Applying pressure externally allows us to explore the effect of distorting the lattice and unit cell lattice parameters, without the added complication of adding new pinning centres. Thus, it is the hope that this line of enquiry will provide some insight into how these pinning centres are actually evolving in relation to the various lattice parameters and higher order transitions present in the Ba122 family.

6.1 TRANSITION TEMPERATURE MEASUREMENTS

Zero-field cooled temperature ramps were measured with an applied field of 0.5 mT for each sample and each pressure ranging from 0 GPa to 1.2 GPa. Six samples were measured as a function of pressure; one underdoped ($x = 0.041$), four optimally doped ($x = 0.048, 0.049, 0.050a, 0.050b$), and one on the overdoped side of the doping phase diagram ($x = 0.066$).

6.1.1 *Temperature Dependent Magnetisation versus Pressure*

Transition width

Figure 6.1 shows the effect pressure has on ZFC curves collected for the different samples. Each sample reacted in a slightly different way with the underdoped sample ($x = 0.041$) displaying a very marked introduction of weak link behaviour after application of pressure and the subsequent reduction of this behaviour as pressure continued to be increased. This broadening results in considerable difficulty in determining a value for T_c -crossover at these pressures. For severely broadened transitions, there are multiple temperature intervals through which it would be plausible to fit and extrapolate. When this occurred, as in the $x = 0.041$ sample at 0.2 and 0.4 GPa, T_c was taken as the average of the smallest and largest T_c obtainable via the T_c -crossover method, resulting in much larger uncertainties.

The $x = 0.048$ sample displays a consistent ZFC behaviour, with ΔT_c consistently less than 1.5 K. This sample will prove to be well behaved over all of our pressure dependent measurements, and this fact is likely related to less weak-link behaviour when compared to that observed in the underdoped and, to a lesser extent, the optimally doped $x = 0.050$ sample.

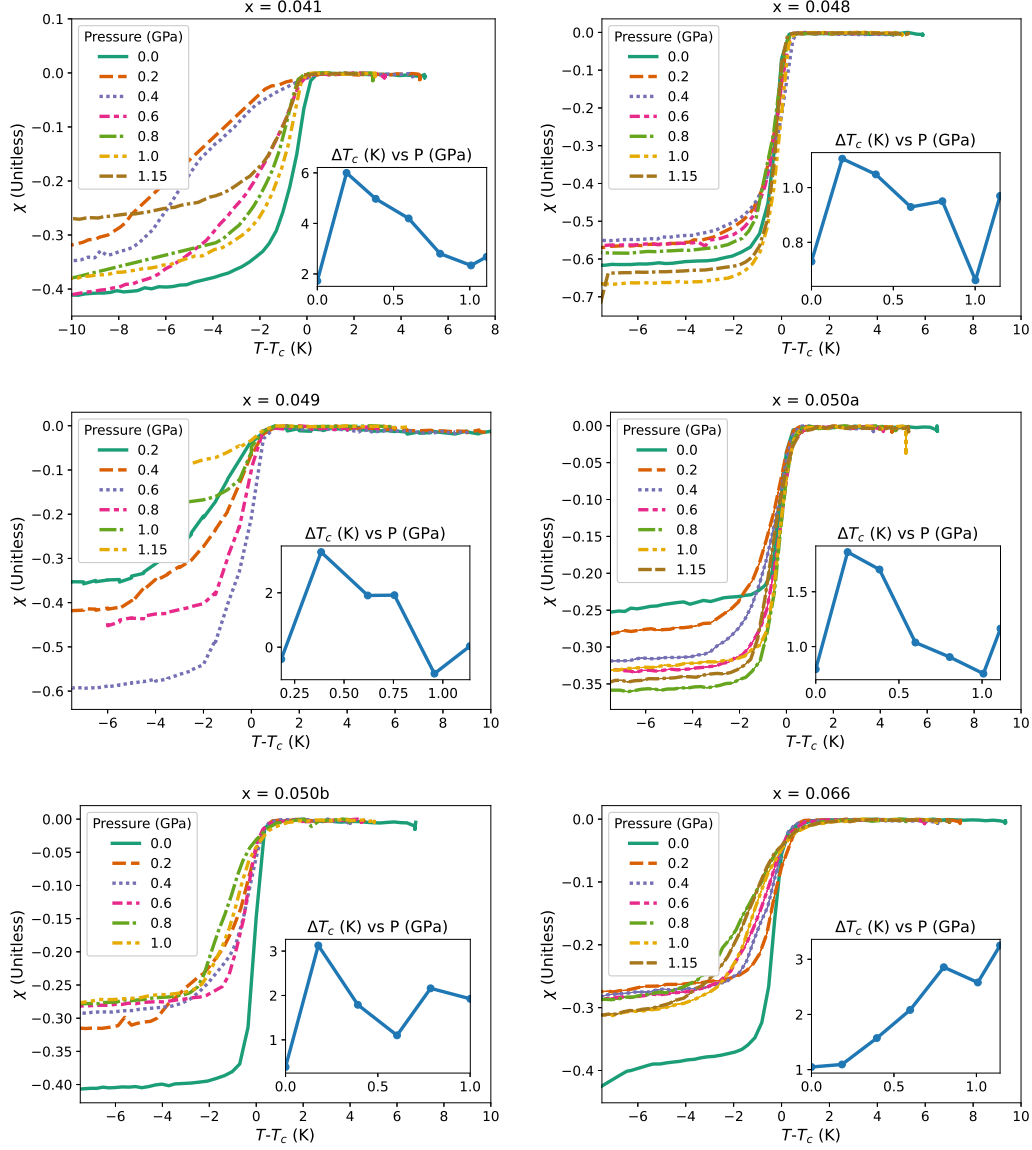


Figure 6.1: Pressures ranging from 0 to 1.2 GPa result in a distinctive broadening of ΔT_c , the value of which is depicted in each inset. Local maxima occur at approximately 0.4-0.6 GPa for the optimally doped and underdoped samples, whereas the overdoped samples display a steady increase.

Some key features are relatively consistent between the different samples. Each of the underdoped and optimally doped samples show a changeover from positive to negative gradient in ΔT_c somewhere around 0.4-0.6 GPa. This change in gradient appears to occur at the same pressure in the T_c versus doping plots in Figure 6.2, which exhibit a similar local maximum. This is not seen at all in the overdoped $x = 0.066$ sample which shows a consistent increase of ΔT_c with pressure.

6.1.2 *Transition Temperature versus Pressure*

Figure 6.2 displays the T_c -crossover values for each sample as a function of pressure. Each sample returned to the same value of T_c upon depressurisation of the pressure cell and remeasuring, meaning that any of the effects which actually manifest in a change in critical temperature are reversible.

Three of the optimally doped samples, $x = 0.048$, 0.050a and 0.050b, all display a rapid increase in T_c between 0 and 0.2 GPa, followed by a local maximum at between 19 and 20 K, and finally a slow decrease to lower values. The local maximum, which manifests in all samples except the underdoped representative, occurs at different pressures (P_c), dependent on the sample, ranging from 0.4 - 1.0 GPa. This behaviour has been observed both as a result of doping [6] and pressure in a range of FeSCs including 122 [4, 71, 124, 147], 1111 [67] and 111 structure families [66]. The optimally doped samples $x = 0.048$ and 0.050 have T_c increase at a rate of $dT_c/dP = 5.4$ and 7.7 K/GPa respectively, followed by a much slower change on the decreasing side of the dome.

Our measurements of this phenomena could be complicated by the proximity of the hydrostaticity limit of our pressure transmitting fluid i.e. it is plausible that solidification of the pressure medium is responsible for the delineation of the two separate behaviours. However, this would definitely

be on the low side for the hydrostaticity limit of FC 77:70, with reports ranging from $P_c = 0.8 - 1.2$ GPa [87, 148, 149]. Furthermore, this effect of changing from positive to negative T_c gradient has been seen in other studies [150–152], of which the measured critical pressure (1.5 - 2 GPa) lay well within the measured hydrostatic pressure limit of 10 GPa for a pentane mixture [87].

Non-linear pressure effects

This data contrasts heavily with that found for $\text{BaFe}_2(\text{As}_{1-x}\text{P}_x)_2$. Remember from Chapter 4 that the applied hydrostatic pressure would result in a large compressive strain on the c-axis lattice parameter, followed by a strain compressing a. We can see this dynamic play out in Figure 6.1, with an immediate increase in transition width followed by a slow reduction as we increase pressure. This insinuates that the compression along the c-axis introduces more weak-link behaviour into our system.

However, we see very little evidence of the non-linear pressure effect in the values of T_c versus P . Only the underdoped sample displays the same sensitive negative dependence of T_c at initial low pressures. Even so, T_c changes by at most 25 % significantly smaller than the changes observed in $\text{BaFe}_2(\text{As}_{1-x}\text{P}_x)_2$, but at a similarly large rate of 30 K/GPa. Furthermore, it appears that once we have reached near-optimal doping, this effect is completely suppressed.

In terms of studies on other materials, no evidence of this non-linearity is seen for LiFeAs [153, 154], FeSe [155, 156], or members of the cuprates families such as YBCO [157] of Hg_{1223} and Hg_{1212} [158]. However, of the studies cited, only those on LiFeAs are performed at similarly low pressure steps to ours. LiFeAs is a material which has been measured as having a much smaller anisotropy in its compressibility than the 122 family [159], and thus this contrast is to be expected. One example which defini-

tively manifests the same behaviour is the heavy fermion superconductor CeCu_2Si_2 [160], which is interesting in that it points to a common factor of non-Fermi liquid behaviour leading to this phenomena.

One other pressure study on $\text{Ba}(\text{Fe}_{1-x}\text{Ni}_x)_2\text{As}_2$ measured a small decrease in T_c when applying small uniaxial pressures (≈ 40 MPa) to a nearly optimally doped $\text{Ba}(\text{Fe}_{1-x}\text{Ni}_x)_2\text{As}_2$ crystal [161]. A future study into whether this non-linear pressure dependence of T_c at low pressures can be observed in doped $\text{Ba}(\text{Fe}_{1-x}\text{Co}_x)_2\text{As}_2$ would be instructive, as it could discern whether the degree to which this behaviour is suppressed is related to the difference in ionic radii, the amount of charge doping, or differences in the development of magnetic moments with doping, or even whether it is not seen at all for doping on the Fe site. Already performed studies on $\text{Ba}(\text{Fe}_{1-x}\text{Co}_x)_2\text{As}_2$, again, skip over this pressure range [162].

Change in sign of dT_c/dP

The observation of a local maxima in the pressure dependence consistently across our samples is a phenomenon more easily found in studies of other materials. Two studies by Tafti et al. [150, 151] on KFe_2As_2 and CsFe_2As_2 posit that the change in sign of dT_c/dP at a critical pressure value is in fact indicative of either a change in the superconducting character of the material, from s^\pm to d-wave pairing states, a transition in the normal state properties, such as a structural/magnetic ordering transition, or a Lifshitz transition of the Fermi surface. Our optimally doped samples are known to be near the doping level ($x = 0.050$) associated with a possible QCP [61], providing an interesting and feasible candidate to explain this behaviour.

When compared to the underdoped sample, these optimally doped crystals should require significantly less applied pressure in order to approach this transition. The measurements shown in Figure 6.2 show values of P_c

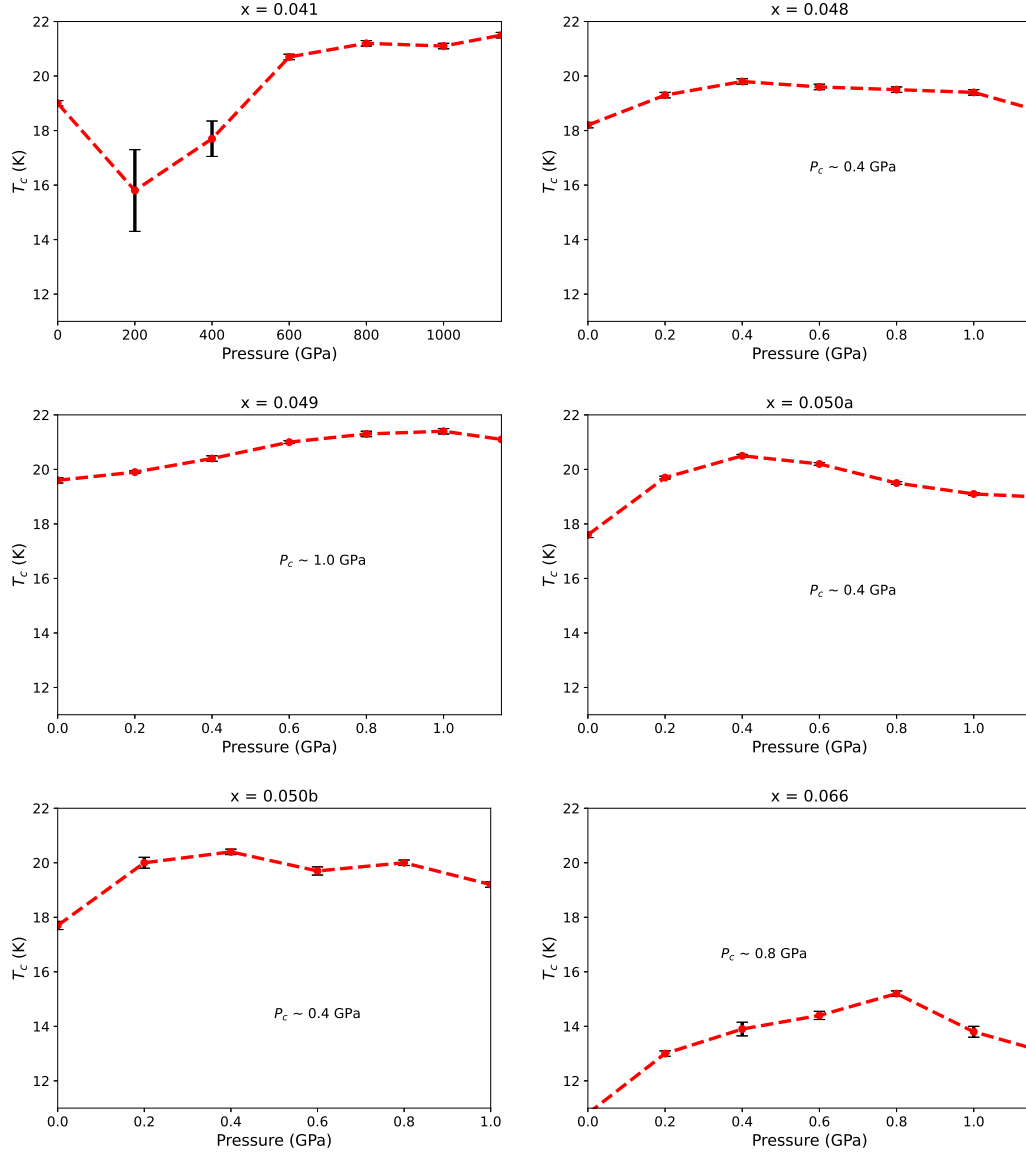


Figure 6.2: T_c as a function of applied pressure for each sample shows consistent behaviour for all except the underdoped sample. A change in sign of the gradient with pressure occurs at a critical pressure (P_c) potentially associated with a AFM and structural transitions having been pushed to lower temperatures. Thus, P_c is indicative of the proximity to proposed QCPs at $x = 0.050$ and 0.070 , meaning the sample at $x = 0.049$ is potentially closer to underdoped than the other three optimally doped samples. The underdoped sample ($x = 0.041$) shows drastic reduction of T_c at low pressures.

between 0.4-1.0 GPa for the optimally doped samples, whereas no critical pressure in the underdoped sample is ascertainable. This means that the value of P_c , can be used as a gauge for how close a particular sample is to critical doping. One important consequence of this is that the sample with $x = 0.049$ is possibly more underdoped than the other near optimally doped ($x = 0.048, 0.050$) samples.

Interplay of doping and pressure effects on T_c

From Figure 6.2 we can see that the underdoped sample actually reaches a higher maximum T_c (21.5 K) than the optimally doped samples (20.5 K). This observation concurs with that seen in single crystals of Co-doped Ba_{122} , which found that underdoped samples at optimal pressure have larger values of T_c and U_0 than optimally doped at ambient pressure [147].

This observation was interpreted as meaning that the introduction of dopant impurities increases the amount of pair breaking in the material, whereas the application of pressure avoids this effect whilst still ameliorating the superconducting strength of samples - an interpretation which appears to nicely fit our data also.

Another possible interpretation comes from some observed differences in the way pressure and doping scale to the lattice parameters in these materials. As detailed by Canfield et al. for transition metal (TM) doping on the iron site [46], changes to the c-axis are linear with increased doping, as is the suppression of higher temperature transitions (T_N and T_s). Regardless of the dopant (either Co, Ni, or Cu) the trends of T_N/T_s vs x fell close to being on top of one another, whereas T_c definitively did not.

However, the converse is true if, instead of looking at plotting χ as a function of T_c , T_c was plotted as a function of extra electrons donated by the TM dopant (i.e. +1, 2, 3 for each Co, Ni, or Cu atom respectively). It was shown then, that the T_c domes scaled on top of one another, and this coincides with a linear relationship between extra electrons and the ratio a/c . Furthermore it is shown that the a -axis increases at a larger rate directly proportional to the number of valence electrons added.

Thus, the peak value of T_c is reached for a particular value of a/c , but each will attain this optimal value for a different value of c (or a) because of the different dopant, meaning the peak T_c value will be different. This process can be manipulated by combining pressure and doping due to the fact that pressure significantly favours compressing the c -axis. Thus, first underdoping and then subsequent compression of the c -axis with applied pressure will result in reaching the optimal value of a/c for a more optimal value of c . This interpretation also explains the fact that the optimally doped crystals reach peak T_c at a lower applied pressure.

6.2 MAGNETIC HYSTERESIS LOOPS

Figure 6.3 shows the hysteresis loops for each sample varying as a function of applied pressure. The fact that each sample had to be cut smaller in order to fit into the pressure cell, as well as the presence of Teflon capsules and copper ring gaskets etc. mean the data itself is prone to a lot more noise and interference. This results in not all of our samples being able to produce reliable hysteresis loop data, meaning the overdoped and one optimally doped sample are excluded from the J_c data in this section. This was not a problem for the ZFC measurements due to the large difference in magnitude of applied fields. Aside from the $x = 0.049$ sample, each were cut from the crystals measured in the doping dependent series presented

in the previous chapter.

The smaller sample and presence of the pressure cell manifests as a linear contribution to the dipole fit which the MPMS uses to obtain each data point, and occasionally results in more dubious fits. In order to trim dubious data, points were excluded on the basis of the SQUIDS output standard deviation. This value represents an uncertainty of the individual fit of the measurement for each data point. Background measurements were taken without any sample present and found to display no hysteretic behaviour and thus the final loops are the result of taking the difference between top and bottom branches and centering around the x-axis.

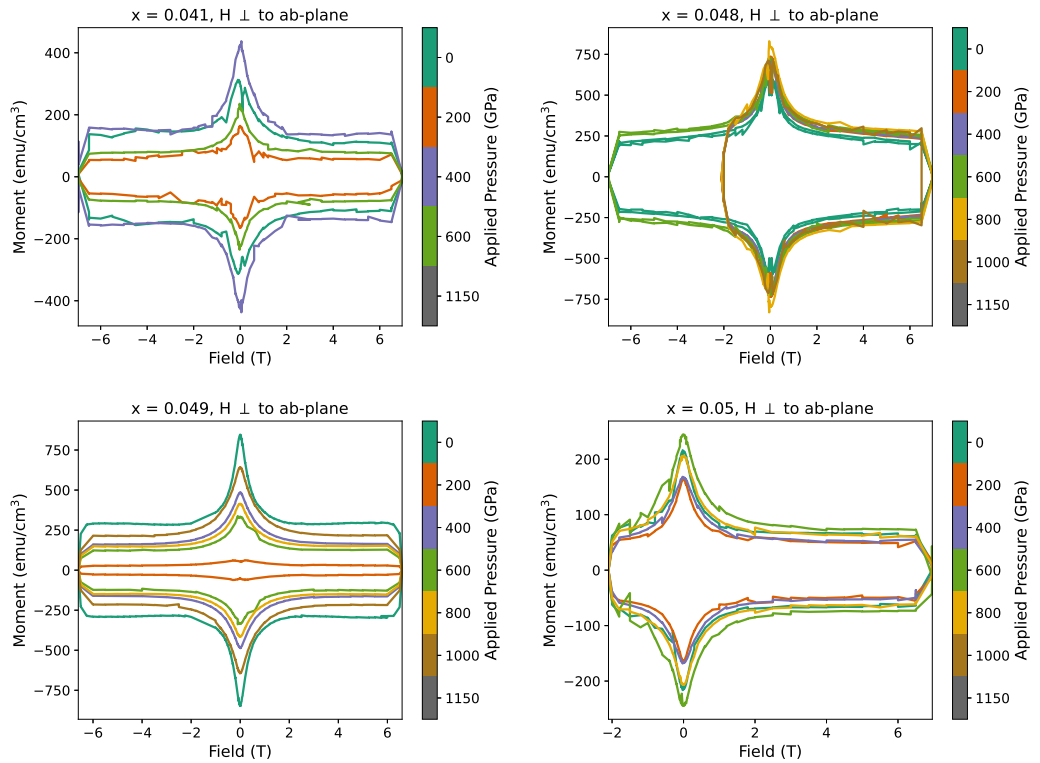


Figure 6.3: Hysteresis loops obtained for four of the available $\text{Ba}(\text{Fe}_{1-x}\text{Ni}_x)_2\text{As}_2$ samples at 2 K. There is a large variation in the size of measured moments with pressure for each sample. Thus, the features of each of these measurement sets is investigated separately in subsequent sections.

Each loop, as is to be expected, displayed the same general shape as those measurements taken outside of the pressure cell. It is interesting to note that the prevalence of the second magnetisation peak is severely diminished in these measurements. This can be seen particularly when contrasting the measurements of $x = 0.048$ inside and outside of the pressure cell. Also, when comparing these measurements note that all the loops in Figure 6.3 were taken at 2 K.

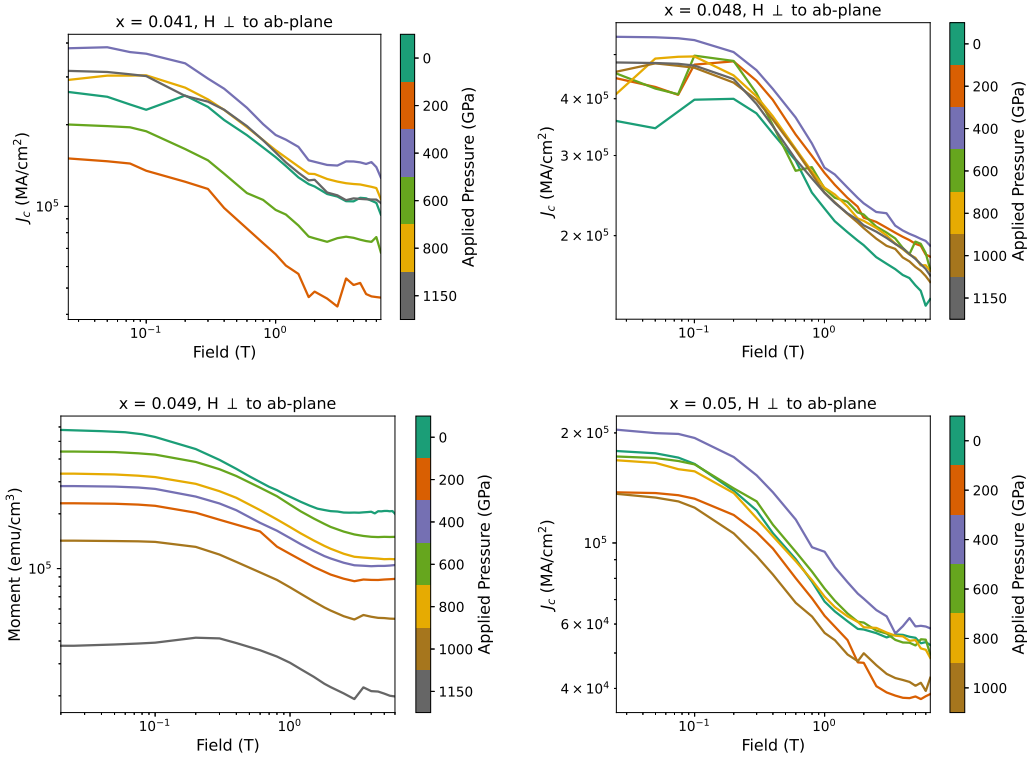


Figure 6.4: Plots of J_c as a function of applied magnetic field for each sample and pressure at 2 K. Values were calculated from the above hysteresis loops via the Bean Model.

6.3 CRITICAL CURRENT DENSITY VERSUS APPLIED FIELD

Figure 6.4 shows the field dependence of J_c for each doping and pressure, with all measurements taken at 2 K. We again see the initial field-independent region occurring up to approximately 0.1 T in each sample

followed by the power-law strong pinning region finally and the plateau towards higher fields as we transition into a collective pinning regime.

6.3.1 *Pressure results by sample*

The results of pressure dependent measurements varied significantly with each sample. Thus, in order to provide a followable account of the results for this pressure dependent chapter, each are presented separately. The complete outlook drawing together the common and uncommon aspects of each set of measurements is presented following.

6.3.1.1 $x = 0.049$

The first sample which we measured the pressure dependence of was the $x = 0.049$ sample. The T_c of this sample with pressure shows steady increases and the brief resolution of local maxima around 1 GPa with an increase on the low pressure side of approximately 1.4 K/GPa.

This trend is not at all seen in the corresponding values for J_c shown in Figure 6.5a. J_c as a function of pressure is characterised by a sharp decrease moving from 0 to 0.4 GPa followed by a sharp local maximum at approximately 0.6 GPa. The local maximum is severely reminiscent of the peak in J_c achieved with doping near this doping level and, if this behaviour is in fact reflective of superconducting properties rather than sample quality this could be interpreted as reproducing the same effect as the small amount of doping from $x = 0.049$ to 0.050.

However, this interpretation seems unlikely due to the fact that we are not in fact improving the value of J_c between 0 GPa and 0.6 GPa as shown in Figure 6.5b. The values of J_c at 0.6 GPa do not quite make up for the large

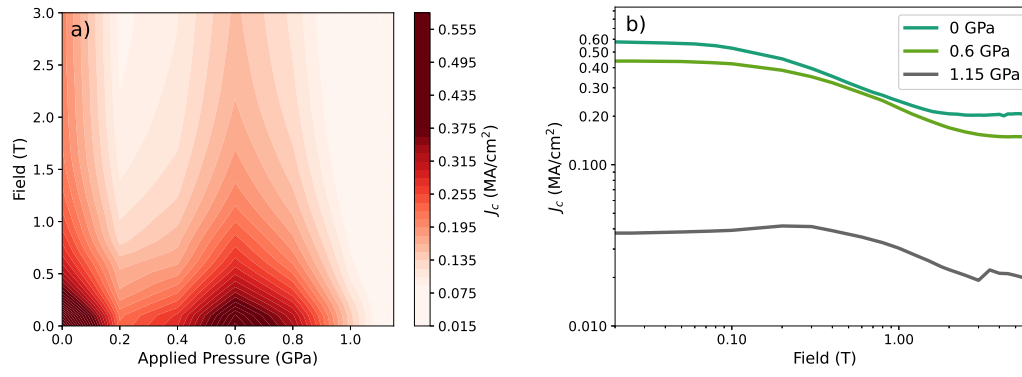


Figure 6.5: $J_c(P)$ for the $x = 0.049$ sample (a) shows a large reduction at low pressures followed by a distinct large peak at 0.6 GPa, and then continued reduction up to 1.2 GPa. Between these three pressures we see that we do not improve J_c with the initial and peak J_c being very similar, with small changes to the onset of the power law strong pinning regime (b). The difference between max and min pressures is a order of magnitude reduction.

loss in J_c at lower pressures.

The application of pressure does however have a consistent effect on the field values at which the different $J_c(H)$ regimes begin. The initial field independent regime extends further to higher fields with increased pressure, and the plateau indicating the onset of collective pinning is also pushed to higher fields.

The most important aspect of these measurements which is anomalous is the initial large decreases of J_c at low pressures. Immediate candidates to produce this effect would be:

1. A non-hydrostatic effect causing the sample to shift from a geometry where the applied field direction and the ab-plane are orthogonal to one where they are parallel. This will cause the intrinsic anisotropy of the crystals to realise lower J_c values.
2. A physical cracking or breaking of the sample, resulting in a smaller superconducting volume fraction and consequently lower mass of the

superconductor which would result in a wrong conversion factor from measured magnetic moment to Bean critical state current, or

3. Intercalation of the pressure medium causing a separation of layers of our superconductor leading to the same effect described for a physical breaking of the sample.

However, a repeat measurement at 0 GPa was not taken for this sample, making the distinction between these scenarios difficult. So, the subsequent pressure dependent sample measurements were taken with some mind to first of all reproducing this result, and secondly distinguishing whether any of these possibilities were indeed the case.

Any changes of orientation should be immediately discernible in the ZFC measurements due to the different demagnetisation factor when placed in the different orientations. We will be able to distinguish whether any irreversible damage is done to the sample by virtue of remeasuring future samples at 0 GPa after the high pressure measurements. Unfortunately, the process of retrieving the samples from the pressure cell is quite difficult to do consistently, in fact more often than not, the sample was destroyed during the process of attempting to unlock the piston clamp cell at the end of each range of measurements.

Thus, for the remainder of our pressure dependent samples, we will perform a second 0 GPa measurement after the application of a full cycle of pressures. Comparing J_c vs H and temperature dependent magnetisation curves will allow us to uncover permanent changes to the sample induced by applying large pressures throughout the course of our measurements.

When taking into account the size of the molecules in the pressure medium, the third scenario does not seem reasonable. Fluorinert liquids are made of perfluorocarbons, with FC70 in particular containing perfluorotripty-

lamine molecules, with an average volume on the order of 600 \AA [163]. This fluid intercalating between FeAs planes in BaFe_2As_2 which have an interplanar distance less than the c-axis lattice parameter and thus on the order of 10 \AA is very unlikely.

$$\underline{x = 0.048}$$

Next, we present the pressure dependent measurements of another close to optimally doped sample with doping fraction $x = 0.048$ (Figure 6.6).

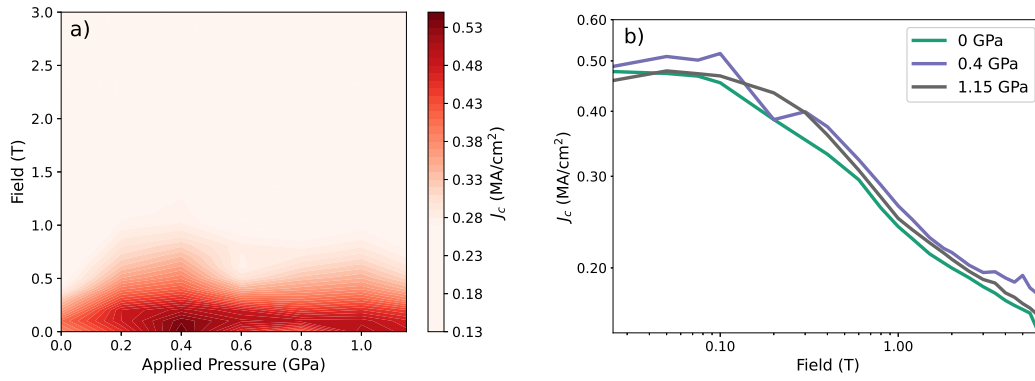


Figure 6.6: $J_c(P)$ (a) for the $x = 0.048$ sample displays only moderate changes. A small peak is distinguished at 0.4 GPa, corresponding to a change of 10 % and coinciding with the P_c associated with the change in T_c behaviour. The figure right (b) demonstrates very little change to the field profile with pressure except for the movement of the low-field H_{irr} being shifted to higher fields at the peak pressure.

This sample has an initial value for T_c of 18.2 K, and upon pressurisation increases up to a maximum value of 19.8 K at 0.4 GPa at a rate of 4 K/GPa. This is significantly faster than the $x = 0.049$ sample which did not reach a peak in T_c until approximately 1 GPa.

This sample contrasts with the previous result in a number of other ways. Firstly, the value of J_c at $(H, P) = (0,0)$ coincides with the measurement taken outside of the pressure cell, meaning we can be quite confident that

the process of placing the sample in the pressure medium and lightly hand tightening the cell was not rough enough to cause any change in the pinning landscape of our crystal. Secondly, there is no large initial decrease in the J_c at low pressures, insinuating that this was indeed a sample dependent feature. J_c reaches a maximum at approximately 0.4 GPa, with a change of 10 % at 0.15 MA/cm²/GPa moving from 0 GPa to peak pressure.

Secondly, the shape of the pressure dependence of T_c and J_c are very similar with a broad maximum form 0.4-0.8 GPa in both. The difference in T_c between 0 GPa and 0.4 GPa are 10 % and 20 %, respectively, meaning that either the proportionality between T_c is not simply one to one, or that additional amelioration is being caused by changes in the pinning landscape.

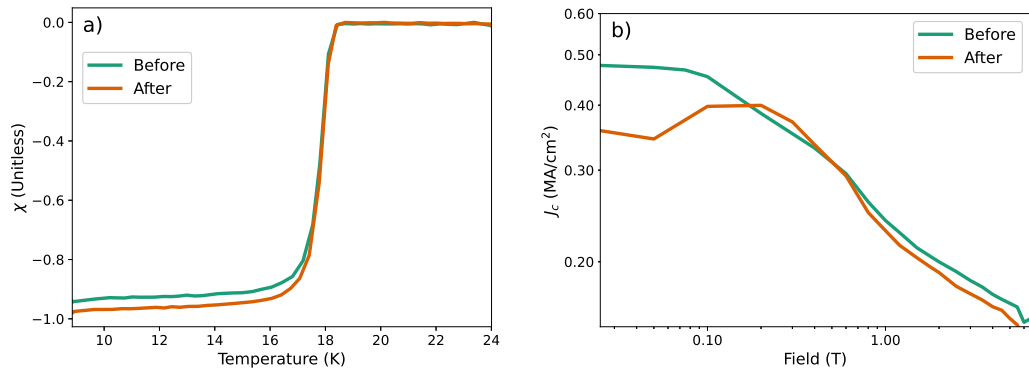


Figure 6.7: Plots of J_c at 2 K (a) and superconducting transition (b) both at 0 GPa before and after a pressurisation cycle. The ZFC curves show no change in the demagnetisation, and thus orientation, of our sample during this process. J_c profiles also lie nicely upon one another demonstrating the reversibility of this process. However, one obvious difference in the J_c profiles is the removal of the low-field dip.

Figure 6.7 shows the result of measurements, both $J_c(H)$ and ZFC, at 0 GPa before and after a round of pressurisation measurements. The ZFC transitions lay almost exactly on top of each other verifying that the sample did not move in the Teflon capsule, nor was there any irreversible introduction of weak-link type micro cracking or reactions on the surface of the sam-

ple.

The J_c before/after snapshot shows that the changes in J_c with pressure are indeed reversible. However, we can see that the behaviour at low fields does differ between the two measurements with the low-field irreversibility dip present in the latter measurement.

$$\underline{x = 0.050}$$

Another sample near optimal doping was investigated, largely to discern whether the large initial dip observed in the $x = 0.049$ sample was reproducible, but also to see whether the application of pressure to the sample at which we see maximum J_c in the phase diagram will have an observable difference.

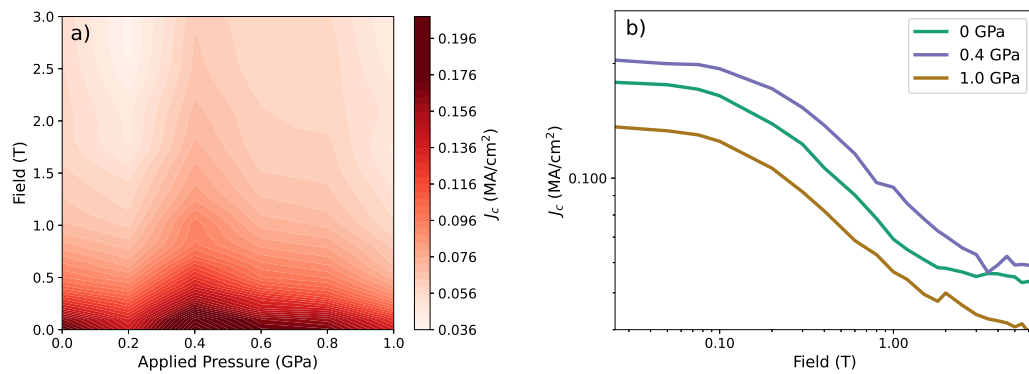


Figure 6.8: This final optimally doped sample ($x = 0.050$) reproduces the $J_c(P)$ (a) profile of the $x = 0.049$ sample, with an initial dip, peak at 0.4 GPa, and continued reduction of J_c following. $J_c(H)$ for minimum and maximum pressure values, and pressure associated with the peak in J_c are presented (b) also. Field profiles are very similar, with an improvement of 25 %.

In Figure 6.8 not only do we recover the dip in J_c moving from 0 to 0.2 GPa, but in fact the value of J_c after cutting the sample down to fit in the pressure cell and applying a hand-tightening amount of pressure has already caused the samples J_c to diminish by a factor of 4. Figure 6.9 shows that this can

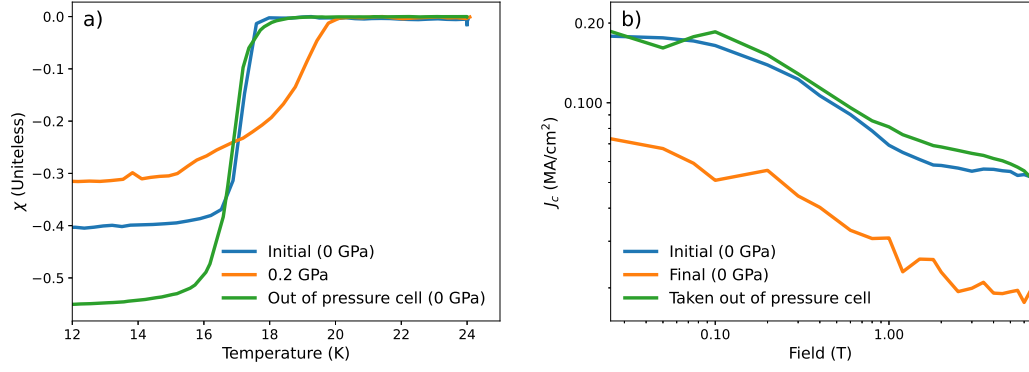


Figure 6.9: The plot of ZFC (a) shows an immediate reduction in the susceptibility when moving from initial 0 GPa to 0.2 GPa of pressure. This definitively shows a shift of the sample to less demagnetisation and consequently a change towards the field orientation. This means the measured change in J_c from 0 to 0.2 GPa (b) should actually be an improvement due to the effect of the large J_c anisotropy. Measurements after the pressure cycle show the difference between J_c at 0 GPa and peak pressure is actually an improvement of 300 % at 0.6 MA/cm²/GPa.

be explained by virtue of changing orientation of the sample within the cell. During the application of pressure the ZFC curves show a transition of low temperature susceptibility from -0.4 to -0.2. This is indicative of a change in orientation of the sample, where the application of pressure has pushed the sample towards the parallel field orientation.

Following this, the value of the low temperature susceptibility remains constant indicating that results aside from the transition from 0 to 0.2 GPa can be taken as consistent. This is reiterated by data taken after having recovered the sample from the cell and remeasuring recovering the original J_c values and similar susceptibility indicating that no permanent damage was done to the sample. Applying the same logic to the $x = 0.049$ sample results in the increase J_c from 0.2 GPa to peak pressure gives increases of 90 % at a rate of 0.5 MA/cm²/GPa.

Thus, we find significant increases from 0 to 0.4 GPa of pressure, where the 0 GPa measurement was taken as the measurement post applying pressures.

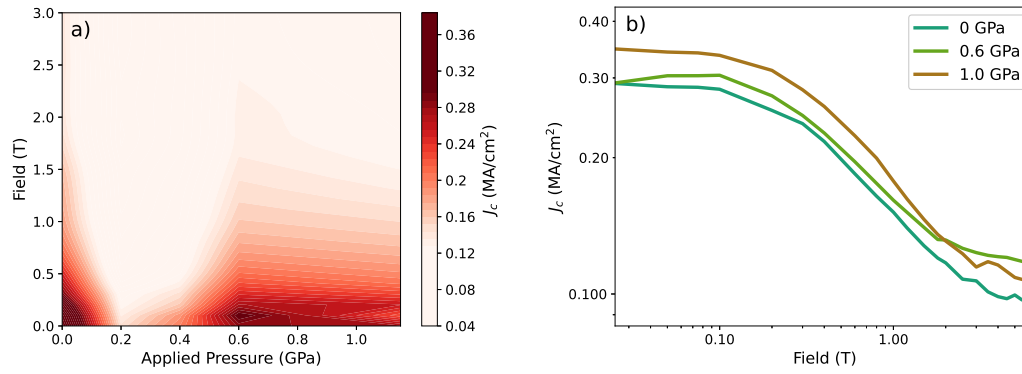


Figure 6.10: $J_c(P)$ for the underdoped sample (a) displays distinctly different behaviour. $J_c(P)$ shows the same initial decrease although this follows the same trend as that seen in the T_c behaviour. Thus, we expect that this behaviour is not related to a change in orientation as shown for previous samples. The J_c as a function of H (b) shows that there is very little change in the values of J_c outside of the large dip at low pressures.

J_c at 2 K and 0 T increases by 300 % at a rate of $0.6 \text{ MA/cm}^2/\text{GPa}$ and then proceeds to diminish on the far side of this local maxima, following the trend delineated by the T_c pressure dependence. So far it would seem that this consistent local maxima is simply related to the local maxima in the change in T_c , indicative of the closeness in doping concentrations of each of these samples meaning a similar pressure effect to push them towards optimal doping.

6.3.1.2 Underdoped Sample

Finally, we performed measurements on the nominally underdoped sample with doping fraction $x = 0.041$.

The underdoped sample again shows the significant decrease in J_c at low pressures, moving from 0 to 0.2 GPa. At 0 T and 2 K, J_c reduced by a factor of 50 % at a rate of 0.6 MA/cm^2 . At first glance this appears to be the same phenomena as that exhibited by the $x = 0.049, 0.050$ samples, however this samples J_c behaviour follows the trend delineated by the T_c vs pressure

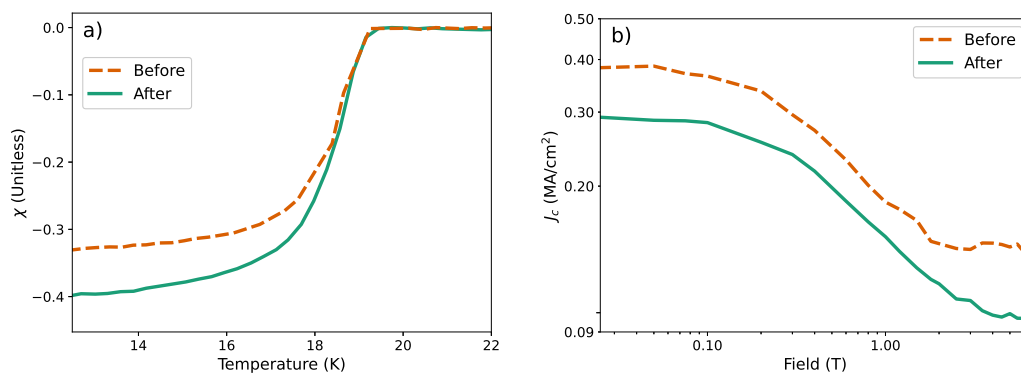


Figure 6.11: Plots of $J_c(H)$ (a) and ZFC curves (b) before and after a pressure cycle. The ZFC curves show very little change in the demagnetisation of the sample meaning the orientation was changed enough to account for the large decrease in J_c at low pressures. Returning to 0 GPa also reveals an improvement in J_c that is retained after this pressure cycle, despite the change in demagnetisation indicating a slight change in orientation which should result in a reduction of J_c .

measurements. Over the same pressure variation, T_c reduces by a factor of 37 % and a monstrous rate of 35 K/GPa. Changes in orientation/superconducting volume fraction would not affect the deduction of T_c from ZFC measurements and thus, this must be a separate phenomenon related to the fact that this sample is underdoped.

Apart from the data at 0.2 GPa, the overall amelioration of J_c between initial and peak pressures gives a factor of improvement of 30 % and a rate of 0.1 MA/cm².

Figure 6.11 shows the ZFC and J_c measurements before and after cycling the pressure, showing very little change in the demagnetisation and thus orientation of the sample and consequently reliability of the pressure dependent measurements for this sample.

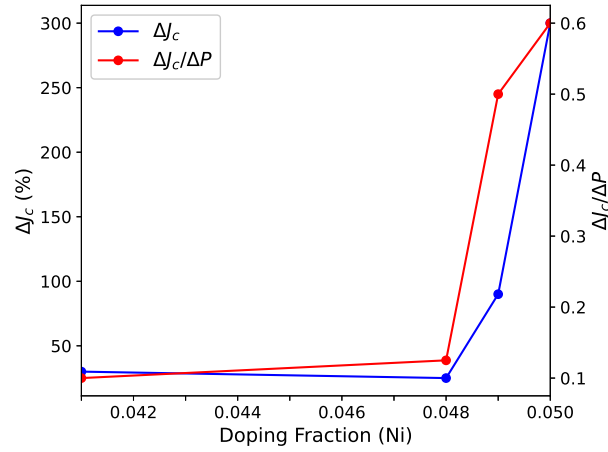


Figure 6.12: The observed changes in J_c at initial 0 GPa and its peak value with pressure show a large improvement as we approach the proposed QCP at $x = 0.050$.

6.3.2 Pressure Effects on Critical Current Density

Previous reports on the pressure dependence of J_c have led to it being considered a very plausible avenue for the purposeful amelioration of critical current properties. Papers describing application of similar max pressures have proclaimed increases of 500 % in potassium doped Ba122 [78], 3000 % in $\text{Sr}_4\text{V}_2\text{O}_6\text{Fe}_2\text{As}_2$ [77], and increases of 8000 % for the pinning force in cobalt doped NaFeAs [3]. Quite often these numbers are a result of measuring the large and quick degradation of J_c that is seen at high temperatures and high fields.

However, as we have taken pressure induced differences at 2 K and 0 T, the gains in J_c are relatively moderate - 25 percent between the initial 0 GPa measurement in the $x = 0.048$ sample, 30 % in the underdoped sample. However, these gains do become more significant as we approach the values corresponding to the posited QCP and our peak in J_c doping diagram, indicative of the obviously sensitive nature of this peak.

Each of the samples at $x = 0.041$, 0.048 , 0.049 , and 0.050 each show a local maximum in the value of J_c between 0.4 and 0.6 GPa. In Figure 6.12 we present the percentage increases in J_c between minimum pressure and the pressure coinciding with the local maxima in J_c . Note that we have been careful to take these difference between pressures which exhibit similar volume fractions presented in Figure 6.1. The increase in J_c is significantly more for the $x = 0.049$ and 0.050 samples.

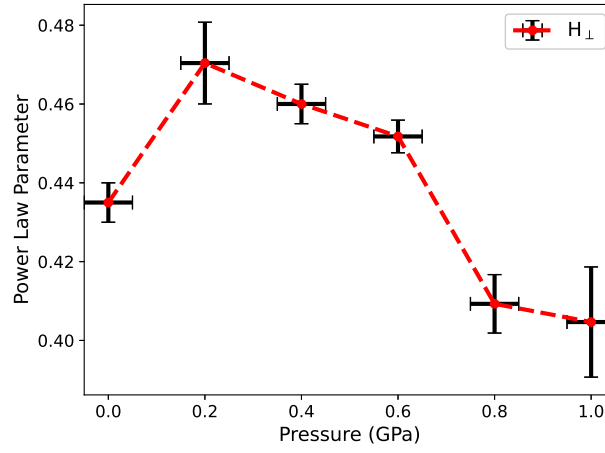


Figure 6.13: Values of μ obtained via fits to the strong pinning region of each pressure for the $x = 0.050$ sample at 2 and 4 K. This plot demonstrates an increase in the strength of the pinning centres upon pressurisation, commensurate with the observed peak in J_c for this sample.

This behaviour concurs with reports of increased J_c in studies by Shabbir et al. [3, 78] in $\text{Ba}_{1-x}\text{K}_x\text{Fe}_2\text{As}_2$ and $\text{NaFe}_{0.97}\text{Co}_{0.03}\text{As}$ who found very large increases in J_c for the an optimally doped sample. However, very few studies have been performed on J_c as a function of both pressure and doping, and only pressure studies which increase J_c tend to be reported. Thus, more pressure- J_c studies would need to be performed on samples which are not optimally doped in order to verify that this behaviour is consistent amongst iron pnictides.

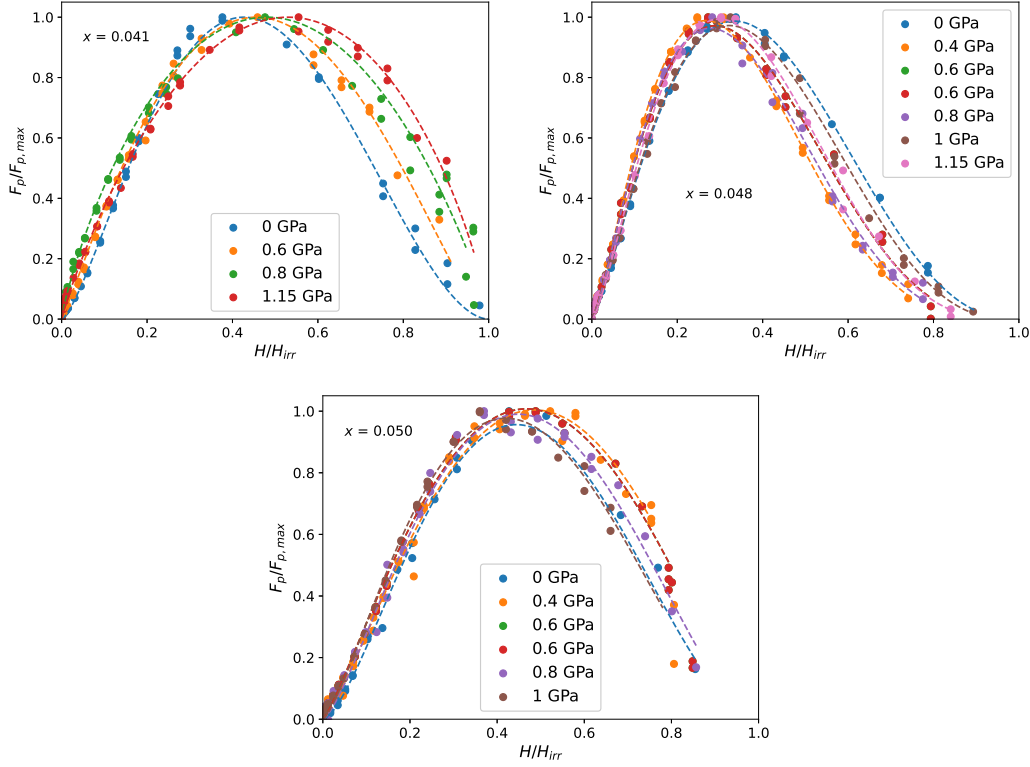


Figure 6.14: Dew-Hughes pinning plots show that pressure does not appear to significantly change the nature of pinning in the optimally doped samples. However, the underdoped sample shows a distinct move of peak pinning force density to higher fields.

With the exception of the underdoped sample observed increases in J_c coincide with increases in the T_c of each sample. However, we know that J_c is affected both by changes in superconducting parameters and also pinning landscape. Thus, we will now attempt to glean some information as to the evolution of pinning properties as a function of pressure.

Fits to the strong pinning regime as a function of pressure showed very little effect, with the samples at $x = 0.041$, and 0.048 both returning values of $\mu \approx 0.4$ with no variation with pressure. The $x = 0.050$ sample however did display a local maximum in μ coinciding with increases in T_c and J_c . This shows that the increase in ΔJ_c at optimal doping are related to a pressure induced increase in the strength of pinning centres.

The Dew-Hughes plots in Figure 6.14 depict definitive differences between each sample. The $x = 0.048$, and 0.050 samples retains the same pinning over the pressure range, whereas the underdoped sample clearly manifests a movement to higher fields of the peak position as we increase the applied pressure. The $x = 0.048$ sample displays a value of $h_{\text{max}} = 0.30 \pm 0.03$, corresponding to the dominance of point pinning, core pinning centres, whereas the optimally doped sample displays a higher value of the peak position which is directly in line with our observation that the initial application of pressure has pushed the sample closer to a parallel field orientation.

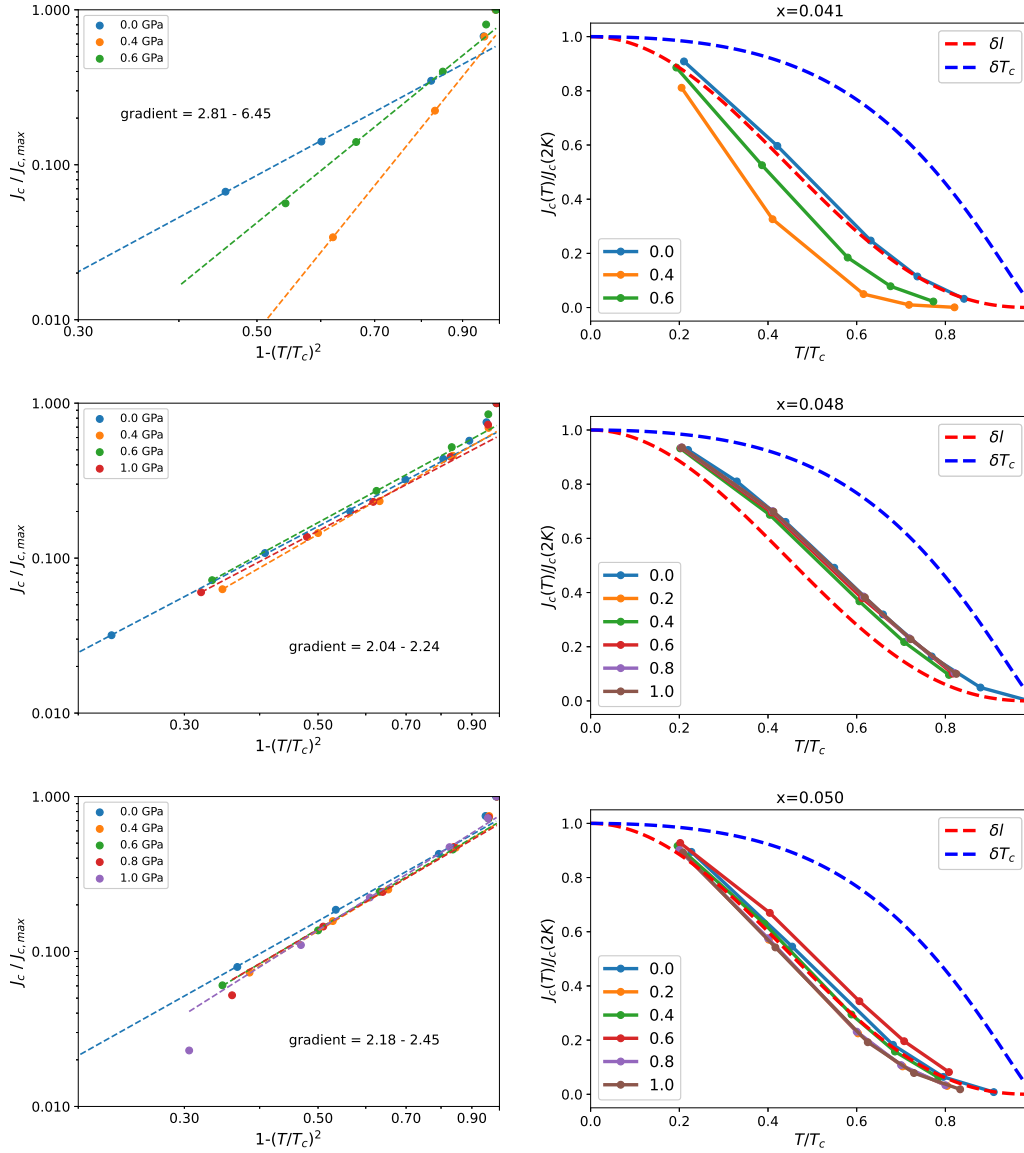


Figure 6.15: Fits of the temperature dependence at each pressure show a consistent combination of δT_c and δI pinning in the two optimally doped samples. Again, the underdoped sample does not follow this trend, showing an initial δI pinning profile which immediately is shifted.

It is already quite definitive from the T_c and J_c behaviours that the underdoped sample is quite different from the rest of the samples but, even further, we can see that the singular behaviour exhibited by the underdoped sample occurs in tandem with a change in the pinning landscape of those crystals. This difference can be related to some of the data from the previous chapter. In particular, the magnetic anisotropy for $x = 0.041$ was

significantly different to the rest of the samples, an observation linked with its position in relation to the structural transition in Ba122 .

This will directly affect the anisotropy of strains induced by hydrostatic pressure seen in this sample, and the $\text{BaFe}_2(\text{As}_{1-x}\text{P}_x)_2$ series. Thus, we can posit that the effects seen our optimally and overdoped samples correspond with hydrostatic strain being applied to the crystal structure.

Figure 6.15 shows the results of temperature dependent pinning analyses. The $x = 0.048$ and 0.050 samples show little variance in the dominant pinning mechanism, with both of these samples displaying a combination of δT_c and δl pinning, with a dominance of δl pinning for the whole pressure range. The underdoped sample initially exhibits an uniquely δl pinning dependence, with the application of pressure immediately destroying any adherence to either model at 0.4 GPa. Further application of pressure at 0.6 GPa results in a shift back towards the δl trend.

6.4 CONCLUSION

To conclude this section, we reiterate the key observations resulting from the pressure dependent measurements of $\text{Ba}(\text{Fe}_{1-x}\text{Ni}_x)_2\text{As}_2$ single crystals:

- Over the pressure range 0 - 1.2 GPa we found that samples near optimal doping both followed a trend of initial increases in J_c followed by a switch to negative pressure dependence at a local maxima occurring at P_c in both $J_c(P)$ and $T_c(P)$ data. The improvements in J_c between P_{initial} and P_c increased dramatically upon approaching the optimal doping value associated with both the anomalous peak in J_c from the previous chapter and the potential location of a QCP and a corresponding increase in the strength of pinning centres.

- The underdoped sample at $x = 0.041$ is a notable exception to this behaviour, displaying a markedly different T_c behaviour. This sample behaves similarly to the $\text{BaFe}_2(\text{As}_{1-x}\text{P}_x)_2$ series of samples, indicating that anisotropy of strains induced by hydrostatic pressure is a dominant factor in this sample. At small pressures, lower than 0.6 GPa, we observed an immediate and reversible degradation of T_c at a rate of 35 K/GPa.
- These two different behaviours were also distinguished by the pinning analysis. Optimally doped samples showed consistent peak positions in the Dew-Hughes analysis, and a clear combination of both δT_c and δl pinning.

CONCLUSIONS

In this thesis we have seen a significant range of ways in which hydrostatic pressure. Overall, we have highlighted the significant intricacies which must be taken into account when interpreting magnetic J_c measurements under pressure in BaFe_2As_2 . Throughout this study we have shown that J_c values must be interpreted within the context of a known field orientation, and particular doping level - a parameter which comes with a range of complicating factors, including proximity to normal-state transitions, quantum critical points, and different dominant pinning mechanisms.

In Chapter 4, we uncovered that the application of pressures between 0 and 1.2 GPa results in very non-linear trends in the superconducting parameters. In a series of $\text{BaFe}_2(\text{As}_{1-x}\text{P}_x)_2$ single crystals, application of pressures resulted in significant suppression of the superconducting transition temperature. The optimally doped sample in this series presented a decrease in T_c from 29 K to 15 K between 0 and 0.4 GPa - a 50 % decrease. This decrease in T_c was then reversed upon further pressurisation, recovering the zero-pressure values. The pressure dependent J_c measurements show that these changes to T_c dominate the trends in J_c vs pressure.

This non-linear response, we believe, is a result of anisotropic strains induced by hydrostatic pressure and provides a intermediate regime between observations of sharp decreases in T_c at pressures on the tens of MPa scale [42], and the broad dome-like dependence observed over the range of tens of GPa [108]. Furthermore, the effect of doping causes this effect to increase in prominence near the critical doping $x = 0.3$, indicating a softening of the

structural lattice.

In Chapter 5 we uncover a sharp peak in J_c as a function of doping in $\text{Ba}(\text{Fe}_{1-x}\text{Ni}_x)_2\text{As}_2$ single crystals, and demonstrate that this occurs only in an orientation with the applied field applied parallel to the c-axis. Comparison of the pinning characteristic in different field orientations illuminate the importance of orientation for pinning behaviours. We demonstrate that, in an orientation with field parallel to the ab-plane, the increase in strength of point pinning centres responsible for the peak in J_c actually results in a shift of the dominant pinning contribution, causing less effective pinning and significantly lower values of J_c .

Finally, in Chapter 6, we show the difference in how applied pressure affects $\text{Ba}(\text{Fe}_{1-x}\text{Ni}_x)_2\text{As}_2$ single crystals, in comparison to $\text{BaFe}_2(\text{As}_{1-x}\text{P}_x)_{22}$. Below optimal doping, the $\text{Ba}(\text{Fe}_{1-x}\text{Ni}_x)_2\text{As}_2$ crystals behaved similarly, displaying the same non-linear T_c characteristics, and corresponding changes to J_c . When doped further, we move beyond the structural transition which occurs in Ba_{122} materials where the anisotropic strains no longer could be seen to have an effect on T_c .

For the optimally doped $\text{Ba}(\text{Fe}_{1-x}\text{Ni}_x)_2\text{As}_2$ crystals, hydrostatic pressure resulted in a more standard dome-like trend, with J_c following suit. However, the percentage increases in J_c increased significantly upon approaching optimal doping, from 50 % to 250 % increases at 0 T and 2 K.

This thesis will provide a good deal of insight into the way pressure can affect magnetic J_c and T_c measurements, ensuring that any future studies take into account the significance of a large range of complicating factors which can be the difference between huge and moderate changes to superconducting parameters.

BIBLIOGRAPHY

- [1] Yoichi Kamihara, Takumi Watanabe, Masahiro Hirano, and Hideo Hosono. "Iron-based layered superconductor $\text{LaO}_{1-x}\text{F}_x\text{FeAs}$ ($x = 0.05$ - 0.12) with $T_c = 26$ K." In: *Journal of the American Chemical Society* 130.11 (2008), pp. 3296–3297.
- [2] Elliot Snider, Nathan Dasenbrock-Gammon, Raymond McBride, Mathew Debessai, Hiranya Vindana, Kevin Vencatasamy, Keith V Lawler, Ashkan Salamat, and Ranga P Dias. "Room-temperature superconductivity in a carbonaceous sulfur hydride." In: *Nature* 586.7829 (2020), pp. 373–377.
- [3] Babar Shabbir, Xiaolin Wang, Shaban Reza Ghorbani, AF Wang, Shixue Dou, and XH Chen. "Giant enhancement in critical current density, up to a hundredfold, in superconducting $\text{NaFe}_{0.97}\text{Co}_{0.03}\text{As}$ single crystals under hydrostatic pressure." In: *Scientific reports* 5 (2015), p. 10606.
- [4] Awadhesh Mani, Nilotpal Ghosh, S Paulraj, A Bharathi, and CS Sundar. "Pressure-induced superconductivity in BaFe_2As_2 single crystal." In: *EPL (Europhysics Letters)* 87.1 (2009), p. 17004.
- [5] E Colombier, SL Bud'Ko, N Ni, and PC Canfield. "Complete pressure-dependent phase diagrams for SrFe_2As_2 and BaFe_2As_2 ." In: *Physical Review B* 79.22 (2009), p. 224518.
- [6] Paul C Canfield and Sergey L Bud'Ko. "FeAs-based superconductivity: a case study of the effects of transition metal doping on BaFe_2As_2 ." In: (2010).
- [7] GR Stewart. "Non-Fermi-liquid behavior in d- and f-electron metals." In: *Reviews of modern Physics* 73.4 (2001), p. 797.

- [8] Gerald Burns. "High-temperature superconductivity." In: (1992).
- [9] Fritz London and Heinz London. "The electromagnetic equations of the supraconductor." In: *Proceedings of the Royal Society of London. Series A-Mathematical and Physical Sciences* 149.866 (1935), pp. 71–88.
- [10] Michael Tinkham. *Introduction to superconductivity*. Courier Corporation, 2004.
- [11] AB Pippard. "The coherence concept in superconductivity." In: *Physica* 19.1-12 (1953), pp. 765–774.
- [12] John Bardeen, Leon N Cooper, and John Robert Schrieffer. "Theory of superconductivity." In: *Physical review* 108.5 (1957), p. 1175.
- [13] Alexei Alexeyevich Abrikosov. "The magnetic properties of superconducting alloys." In: *Journal of Physics and Chemistry of Solids* 2.3 (1957), pp. 199–208.
- [14] D Dew-Hughes. "Flux pinning mechanisms in type II superconductors." In: *Philosophical Magazine* 30.2 (1974), pp. 293–305.
- [15] Gianni Blatter, Mikhail V Feigel'man, Vadim B Geshkenbein, Anatoly I Larkin, and Valerii M Vinokur. "Vortices in high-temperature superconductors." In: *Reviews of Modern Physics* 66.4 (1994), p. 1125.
- [16] EJ Nicol and JP Carbotte. "Temperature dependence of the critical pair-breaking current in thin-film, strong-coupling superconductors." In: *Physical Review B* 43.13 (1991), p. 10210.
- [17] Vitalii Lazarevich Ginzburg. "Critical current for superconducting films." In: *Sov. Phys.-Dokl.(Engl. Transl.);(United States)* 3.1 (1958).
- [18] FA Lindemann. "The calculation of molecular vibration frequencies." In: *Physik. Zeits* 11 (1910), p. 609.
- [19] Gianni Blatter and Boris Ivlev. "Fluctuations and disorder in high temperature superconductors." In: *Physica B: Condensed Matter* 194 (1994), pp. 1795–1796.

- [20] Wai-Kwong Kwok, Ulrich Welp, Andreas Glatz, Alexei E Koshelev, Karen J Kihlstrom, and George W Crabtree. "Vortices in high-performance high-temperature superconductors." In: *Reports on Progress in Physics* 79.11 (2016), p. 116501.
- [21] Reiner Labusch. "Calculation of the critical field gradient in type-II superconductors." In: *Cryst. Lattice Defects; (United Kingdom)* 1 (1969).
- [22] AI Larkin and Yu N Ovchinnikov. "Pinning in type II superconductors." In: *Journal of Low Temperature Physics* 34.3 (1979), pp. 409–428.
- [23] Yu N Ovchinnikov and BI Ivlev. "Pinning in layered inhomogeneous superconductors." In: *Physical Review B* 43.10 (1991), p. 8024.
- [24] R Griessen, Wen Hai-Hu, AJJ Van Dalen, B Dam, J Rector, HG Schnack, S Libbrecht, E Osquiguil, and Y Bruynseraede. "Evidence for mean free path fluctuation induced pinning in $\text{YBa}_2\text{Cu}_3\text{O}_7$ and $\text{YBa}_2\text{Cu}_4\text{O}_8$ films." In: *Physical review letters* 72.12 (1994), p. 1910.
- [25] II Mazin and MD Johannes. "A key role for unusual spin dynamics in ferropnictides." In: *Nature Physics* 5.2 (2009), pp. 141–145.
- [26] GA Sawatzky, IS Elfimov, J Van Den Brink, and J Zaanen. "Heavy-anion solvation of polarity fluctuations in pnictides." In: *EPL (Europhysics Letters)* 86.1 (2009), p. 17006.
- [27] J George Bednorz and K Alex Müller. "Possible high T_c superconductivity in the Ba-La-Cu-O system." In: *Zeitschrift für Physik B Condensed Matter* 64.2 (1986), pp. 189–193.
- [28] Ni Ni, SL Bud'ko, A Kreyssig, S Nandi, GE Rustan, AI Goldman, S Gupta, JD Corbett, A Kracher, and PC Canfield. "Anisotropic thermodynamic and transport properties of single-crystalline $\text{Ba}_{1-x}\text{K}_x\text{Fe}_2\text{As}_2$ ($x=0$ and 0.45)." In: *Physical Review B* 78.1 (2008), p. 014507.
- [29] Zhao-Sheng Wang, Hui-Qian Luo, Cong Ren, and Hai-Hu Wen. "Upper critical field, anisotropy, and superconducting properties of $\text{Ba}_{1-x}\text{K}_x\text{Fe}_2\text{As}_2$ single crystals." In: *Physical Review B* 78.14 (2008), p. 140501.

- [30] MM Altarawneh, K Collar, CH Mielke, N Ni, SL Bud'Ko, and PC Canfield. "Determination of anisotropic H_{c2} up to 60 T in $Ba_{0.55}K_{0.45}Fe_2As_2$ single crystals." In: *Physical Review B* 78.22 (2008), p. 220505.
- [31] Ni Ni, ME Tillman, J-Q Yan, A Kracher, ST Hannahs, SL Bud'Ko, and PC Canfield. "Effects of Co substitution on thermodynamic and transport properties and anisotropic H_{c2} in $Ba(Fe_{1-x}Co_x)_2As_2$ single crystals." In: *Physical Review B* 78.21 (2008), p. 214515.
- [32] MA Tanatar, N Ni, C Martin, RT Gordon, H Kim, VG Kogan, GD Samolyuk, SL Bud'ko, PC Canfield, and R Prozorov. "Anisotropy of the iron pnictide superconductor $Ba(Fe_{1-x}Co_x)_2As_2$ ($x = 0.074$, $T_c = 23$ K)." In: *Physical Review B* 79.9 (2009), p. 094507.
- [33] SV Chong, S Hashimoto, and K Kadowaki. "Upper critical fields and critical current density of $BaFe_2(As_{0.68}P_{0.32})_2$ single crystal." In: *Solid state communications* 150.27-28 (2010), pp. 1178–1181.
- [34] Athena S Sefat, Rongying Jin, Michael A McGuire, Brian C Sales, David J Singh, and David Mandrus. "Superconductivity at 22 K in Co-doped $BaFe_2As_2$ crystals." In: *Physical review letters* 101.11 (2008), p. 117004.
- [35] GR Stewart. "Superconductivity in iron compounds." In: *Reviews of Modern Physics* 83.4 (2011), p. 1589.
- [36] FC Hsu, JY Luo, KW Yeh, TK Chen, TW Huang, PM Wu, YC Lee, and YL Huang. "Y.-Y. Chu, D.-C. Yan, and M.-K." In: *Proc. Natl. Acad. Sci. USA* 105.14262 (2008), p. 8.
- [37] XC Wang, QQ Liu, YX Lv, WB Gao, LX Yang, RC Yu, FY Li, and CQ Jin. "The superconductivity at 18 K in LiFeAs system." In: *Solid State Communications* 148.11-12 (2008), pp. 538–540.
- [38] Marianne Rotter, Marcus Tegel, and Dirk Johrendt. "Superconductivity at 38 K in the iron arsenide $(Ba_{1-x}K_x)Fe_2As_2$." In: *Physical Review Letters* 101.10 (2008), p. 107006.

- [39] Ren Zhi-An, Lu Wei, Yang Jie, Yi Wei, Shen Xiao-Li, Che Guang-Can, Dong Xiao-Li, Sun Li-Ling, Zhou Fang, Zhao Zhong-Xian, et al. "Superconductivity at 55 K in iron-based F-doped layered quaternary compound $\text{SmO}_{1-x}\text{F}_x\text{FeAs}$." In: *Chinese Physics Letters* 25.6 (2008), p. 2215.
- [40] James Schilling, Narelle Hillier, and Neda Foroozani. "What have we learned from high-pressure experiments on Cu-oxide and Fe-based superconductors?" In: *Journal of Physics: Conference Series*. Vol. 449. 1. IOP Publishing. 2013, p. 012021.
- [41] F Hardy, T Wolf, RA Fisher, R Eder, P Schweiss, P Adelman, H v Löhneysen, and C Meingast. "Calorimetric evidence of multiband superconductivity in $\text{Ba}(\text{Fe}_{0.925}\text{Co}_{0.075})_2\text{As}_2$ single crystals." In: *Physical Review B* 81.6 (2010), p. 060501.
- [42] H-H Kuo, James G Analytis, J-H Chu, RM Fernandes, J Schmalian, and IR Fisher. "Magnetoelastically coupled structural, magnetic, and superconducting order parameters in $\text{BaFe}_2(\text{As}_{1-x}\text{P}_x)_2$." In: *Physical Review B* 86.13 (2012), p. 134507.
- [43] RA Jishi and HM Alyahyaei. "Effect of hybridization on structural and magnetic properties of iron-based superconductors." In: *New Journal of Physics* 11.8 (2009), p. 083030.
- [44] Kirill D Belashchenko and Vladimir P Antropov. "Role of covalent Fe-As bonding in the magnetic moment formation and exchange mechanisms in iron-pnictide superconductors." In: *Physical Review B* 78.21 (2008), p. 212505.
- [45] Jiansheng Wu, Philip Phillips, and AH Castro Neto. "Theory of the magnetic moment in iron pnictides." In: *Physical review letters* 101.12 (2008), p. 126401.
- [46] PC Canfield, SL Bud'Ko, Ni Ni, JQ Yan, and A Kracher. "Decoupling of the superconducting and magnetic/structural phase transi-

- tions in electron-doped BaFe_2As_2 ." In: *Physical Review B* 80.6 (2009), p. 060501.
- [47] Marianne Rotter, Christine Hieke, and Dirk Johrendt. "Different response of the crystal structure to isoelectronic doping in $\text{BaFe}_2(\text{As}_{1-x}\text{P}_x)_2$ and $(\text{Ba}_{1-x}\text{Sr}_x)\text{Fe}_2\text{As}_2$." In: *Physical Review B* 82.1 (2010), p. 014513.
- [48] N Eguchi, M Kodama, F Ishikawa, A Nakayama, A Ohmura, Yuh Yamada, and S Nakano. "Powder x-ray diffraction of BaFe_2As_2 under hydrostatic pressure." In: *Journal of Physics: Conference Series*. Vol. 400. 2. IOP Publishing. 2012, p. 022017.
- [49] Chul-Ho Lee, Akira Iyo, Hiroshi Eisaki, Hijiri Kito, Maria Teresa Fernandez-Diaz, Toshimitsu Ito, Kunihiro Kihou, Hirofumi Matsuhata, Markus Braden, and Kazuyoshi Yamada. "Effect of structural parameters on superconductivity in fluorine-free LnFeAsO_{1-y} ($\text{Ln} = \text{La}, \text{Nd}$)." In: *Journal of the Physical Society of Japan* 77.8 (2008), p. 083704.
- [50] EZ Kuchinskii, Igor Aleksandrovich Nekrasov, and Mikhail Vissarionovich Sadovskii. "Anion height dependence of T_c and the density of states in iron-based superconductors." In: *JETP letters* 91.10 (2010), pp. 518–522.
- [51] Athena S Sefat. "Pressure effects on two superconducting iron-based families." In: *Reports on progress in physics* 74.12 (2011), p. 124502.
- [52] WJ Duncan, OP Welzel, C Harrison, XF Wang, XH Chen, FM Grosche, and PG Niklowitz. "High pressure study of BaFe_2As_2 —the role of hydrostaticity and uniaxial stress." In: *Journal of Physics: Condensed Matter* 22.5 (2010), p. 052201.
- [53] Y Su, P Link, A Schneidewind, Th Wolf, P Adelman, Y Xiao, M Meven, R Mittal, M Rotter, D Johrendt, et al. "Antiferromagnetic ordering and structural phase transition in $\text{Ba}_2\text{Fe}_2\text{As}_2$ with Sn incorporated from the growth flux." In: *Physical Review B* 79.6 (2009), p. 064504.

- [54] MG Kim, RM Fernandes, Andreas Kreyssig, JW Kim, A Thaler, Sergey L Bud'ko, Paul C Canfield, Robert J McQueeney, J Schmalian, and Alan I Goldman. "Character of the structural and magnetic phase transitions in the parent and electron-doped BaFe_2As_2 compounds." In: *Physical Review B* 83.13 (2011), p. 134522.
- [55] Milan Tomić, Roser Valenti, and Harald O Jeschke. "Uniaxial versus hydrostatic pressure-induced phase transitions in CaFe_2As_2 and BaFe_2As_2 ." In: *Physical Review B* 85.9 (2012), p. 094105.
- [56] Jeffery L Tallon, JW Loram, GVM Williams, JR Cooper, IR Fisher, JD Johnson, MP Staines, and C Bernhard. "Critical Doping in Overdoped High- T_c Superconductors: a Quantum Critical Point?" In: *physica status solidi (b)* 215.1 (1999), pp. 531–540.
- [57] ND Mathur, FM Grosche, SR Julian, IR Walker, DM Freye, RKW Haselwimmer, and GG Lonzarich. "Magnetically mediated superconductivity in heavy fermion compounds." In: *Nature* 394.6688 (1998), pp. 39–43.
- [58] John A Hertz. "Quantum critical phenomena." In: *Physical Review B* 14.3 (1976), p. 1165.
- [59] GR Stewart. "Unconventional superconductivity." In: *Advances in Physics* 66.2 (2017), pp. 75–196.
- [60] C Putzke, P Walmsley, JD Fletcher, L Malone, D Vignolles, C Proust, S Badoux, P See, Harvey Edward Beere, David Alastair Ritchie, et al. "Anomalous critical fields in quantum critical superconductors." In: *Nature communications* 5 (2014), p. 5679.
- [61] R Zhou, Z Li, J Yang, DL Sun, CT Lin, and Guo-qing Zheng. "Quantum criticality in electron-doped $\text{BaFe}_{2-x}\text{Ni}_x\text{As}_2$." In: *Nature communications* 4 (2013), p. 2265.

- [62] P Walmsley, C Putzke, L Malone, I Guillamón, D Vignolles, C Proust, S Badoux, AI Coldea, MD Watson, S Kasahara, et al. "Quasiparticle mass enhancement close to the quantum critical point in $\text{BaFe}_2(\text{As}_{1-x}\text{P}_x)_2$." In: *Physical review letters* 110.25 (2013), p. 257002.
- [63] K Hashimoto, Kyuil Cho, T Shibauchi, S Kasahara, Y Mizukami, R Katsumata, Y Tsuruhara, T Terashima, H Ikeda, MA Tanatar, et al. "A sharp peak of the zero-temperature penetration depth at optimal composition in $\text{BaFe}_2(\text{As}_{1-x}\text{P}_x)_2$." In: *Science* 336.6088 (2012), pp. 1554–1557.
- [64] Soon-Gil Jung, Soonbeom Seo, Sangyun Lee, Eric D Bauer, Han-Oh Lee, and Tuson Park. "A peak in the critical current for quantum critical superconductors." In: *Nature communications* 9.1 (2018), p. 434.
- [65] Simon AJ Kimber, Andreas Kreyssig, Yu-Zhong Zhang, Harald O Jeschke, Roser Valentí, Fabiano Yokaichiya, Estelle Colombier, Jiaqiang Yan, Thomas C Hansen, Tapan Chatterji, et al. "Similarities between structural distortions under pressure and chemical doping in superconducting BaFe_2As_2 ." In: *Nature materials* 8.6 (2009), pp. 471–475.
- [66] Yu-Zhong Zhang, Hem C Kandpal, Ingo Opahle, Harald O Jeschke, and Roser Valentí. "Microscopic origin of pressure-induced phase transitions in the iron pnictide superconductors AFe_2As_2 : An ab initio molecular dynamics study." In: *Physical Review B* 80.9 (2009), p. 094530.
- [67] Hironari Okada, Kazumi Igawa, Hiroki Takahashi, Yoichi Kamihara, Masahiro Hirano, Hideo Hosono, Kazuyuki Matsubayashi, and Yoshiya Uwatoko. "Superconductivity under high pressure in LaFeAsO ." In: *Journal of the Physical Society of Japan* 77.11 (2008), p. 113712.
- [68] Hiroki Takahashi, Kazumi Igawa, Kazunobu Arii, Yoichi Kamihara, Masahiro Hirano, and Hideo Hosono. "Superconductivity at 43 K in an iron-based layered compound $\text{LaO}_{1-x}\text{F}_x\text{FeAs}$." In: *Nature* 453.7193 (2008), pp. 376–378.

- [69] Nao Takeshita, Takehiro Yamazaki, Akira Iyo, Hiroshi Eisaki, Hijiri Kito, Toshimitsu Ito, Kenji Hirayama, Hideto Fukazawa, and Yoh Kohori. "Superconductivity of NdFeAsO_{1-y} under Hydrostatic Pressure." In: *Journal of the Physical Society of Japan* 77.Suppl. C (2008), pp. 131–133.
- [70] Wei Yi, Liling Sun, Zhian Ren, Wei Lu, Xiaoli Dong, Hai-jun Zhang, Xi Dai, Zhong Fang, Zhengcai Li, Guangcan Che, et al. "Pressure effect on superconductivity of iron-based arsenic-oxide $\text{ReFeAsO}_{0.85}$ (Re= Sm and Nd)." In: *EPL (Europhysics Letters)* 83.5 (2008), p. 57002.
- [71] Kazumi Igawa, Hironari Okada, Hiroki Takahashi, Satoru Matsuishi, Yoichi Kamihara, Masahiro Hirano, Hideo Hosono, Kazuyuki Matsubayashi, and Yoshiya Uwatoko. "Pressure-induced superconductivity in iron pnictide compound SrFe_2As_2 ." In: *Journal of the Physical Society of Japan* 78.2 (2009), pp. 025001–025001.
- [72] J-E Jørgensen and TC Hansen. "High-pressure neutron diffraction study of BaFe_2As_2 ." In: *The European Physical Journal B* 78.4 (2010), pp. 411–415.
- [73] Yukimichi Tajima, Makoto Hikita, Minoru Suzuki, and Yoshikazu Hidaka. "Pressure-effect study on high- T_c superconducting single crystal of 84 K Bi-Sr-Ca-Cu-O system." In: *Physica C: Superconductivity* 158.1-2 (1989), pp. 237–240.
- [74] Patricia L Alireza, YT Chris Ko, Jack Gillett, Chiara M Petrone, Jacqueline M Cole, Gilbert G Lonzarich, and Suchitra E Sebastian. "Superconductivity up to 29 K in SrFe_2As_2 and BaFe_2As_2 at high pressures." In: *Journal of Physics: Condensed Matter* 21.1 (2008), p. 012208.
- [75] Takehiro Yamazaki, Nao Takeshita, Ryosuke Kobayashi, Hideto Fukazawa, Yoh Kohori, Kunihiro Kihou, Chul-Ho Lee, Hijiri Kito, Akira Iyo, and Hiroshi Eisaki. "Appearance of pressure-induced superconductivity in BaFe_2As_2 under hydrostatic conditions and its extremely

- high sensitivity to uniaxial stress." In: *Physical Review B* 81.22 (2010), p. 224511.
- [76] AP Drozdov, MI Erements, IA Troyan, Vadim Ksenofontov, and SI Shylin. "Conventional superconductivity at 203 kelvin at high pressures in the sulfur hydride system." In: *Nature* 525.7567 (2015), p. 73.
- [77] Babar Shabbir, Xiaolin Wang, Shaban Reza Ghorbani, Chandra Shekhar, Shixue Dou, and ON Srivastava. "Hydrostatic pressure: A very effective approach to significantly enhance critical current density in granular iron pnictide superconductors." In: *Scientific reports* 5 (2015), p. 8213.
- [78] Babar Shabbir, Xiaolin Wang, Yanwei Ma, SX Dou, Shi-Shen Yan, and Liang-Mo Mei. "Study of flux pinning mechanism under hydrostatic pressure in optimally doped (Ba,K)Fe₂As₂ single crystals." In: *Scientific reports* 6 (2016), p. 23044.
- [79] Babar Shabbir, XL Wang, Shaban Reza Ghorbani, SX Dou, and Feixiang Xiang. "Hydrostatic pressure induced transition from δT_c to δl pinning mechanism in MgB₂." In: *Superconductor Science and Technology* 28.5 (2015), p. 055001.
- [80] B Lorenz and CW Chu. "High pressure effects on superconductivity." In: *Frontiers in Superconducting Materials*. Springer, 2005, pp. 459–497.
- [81] J Rodriguez-Carvajal. "Fullprof Program." In: *Physica B* 192 (1993), pp. 55–69.
- [82] Quantum Design. "Magnetic Property Measurement System MPMS 3 User's Manual." In: *Quantum Design Inc* (2016).
- [83] Matthew J Coak, Cheng Liu, David M Jarvis, Seunghyun Park, Matthew J Cliffe, and Paul A Goddard. "SquidLab—A user-friendly program for background subtraction and fitting of magnetization data." In: *Review of Scientific Instruments* 91.2 (2020), p. 023901.

- [84] Quantum Design. "MPMS MultiVu application user's manual." In: *Part number* (2004).
- [85] N Suresh and JL Tallon. "Thermodynamic properties of Pb determined from pressure-dependent critical-field measurements." In: *Physical Review B* 75.17 (2007), p. 174502.
- [86] A Eiling and JS Schilling. "Pressure and temperature dependence of electrical resistivity of Pb and Sn from 1-300K and 0-10 GPa-use as continuous resistive pressure monitor accurate over wide temperature range; superconductivity under pressure in Pb, Sn and In." In: *Journal of Physics F: Metal Physics* 11.3 (1981), p. 623.
- [87] Naoyuki Tateiwa and Yoshinori Haga. "Evaluations of pressure-transmitting media for cryogenic experiments with diamond anvil cell." In: *Review of Scientific Instruments* 80.12 (2009), p. 123901.
- [88] Shuai Jiang, Hui Xing, Guofang Xuan, Cao Wang, Zhi Ren, Chunmu Feng, Jianhui Dai, Zhu'an Xu, and Guanghan Cao. "Superconductivity up to 30 K in the vicinity of the quantum critical point in $\text{BaFe}_2(\text{As}_{1-x}\text{P}_x)_2$." In: *Journal of Physics: Condensed Matter* 21.38 (2009), p. 382203.
- [89] S Kasahara, HJ Shi, K Hashimoto, S Tonegawa, Y Mizukami, T Shibauchi, K Sugimoto, T Fukuda, T Terashima, Andriy H Nevidomskyy, et al. "Electronic nematicity above the structural and superconducting transition in $\text{BaFe}_2(\text{As}_{1-x}\text{P}_x)_2$." In: *Nature* 486.7403 (2012), pp. 382–385.
- [90] H Wadati, I Elfimov, and GA Sawatzky. "Where are the extra d electrons in transition-metal-substituted iron pnictides?" In: *Physical review letters* 105.15 (2010), p. 157004.
- [91] AF Kemper, C Cao, PJ Hirschfeld, and H-P Cheng. "Effects of cobalt doping and three-dimensionality in BaFe_2As_2 ." In: *Physical Review B* 80.10 (2009), p. 104511.

- [92] ZR Ye, Y Zhang, F Chen, M Xu, QQ Ge, J Jiang, BP Xie, and DL Feng. "Doping dependence of the electronic structure in phosphorus-doped ferropnictide superconductor $\text{BaFe}_2(\text{As}_{1-x}\text{P}_x)_2$ studied by angle-resolved photoemission spectroscopy." In: *Physical Review B* 86.3 (2012), p. 035136.
- [93] Jiun-Haw Chu, James G Analytis, Chris Kucharczyk, and Ian R Fisher. "Determination of the phase diagram of the electron-doped superconductor $\text{Ba}(\text{Fe}_{1-x}\text{Co}_x)_2\text{As}_2$." In: *Physical Review B* 79.1 (2009), p. 014506.
- [94] LJ Li, YK Luo, QB Wang, H Chen, Z Ren, Q Tao, YK Li, X Lin, M He, ZW Zhu, et al. "Superconductivity induced by Ni doping in BaFe_2As_2 single crystals." In: *New Journal of Physics* 11.2 (2009), p. 025008.
- [95] L Lyard, Thierry Klein, J Marcus, R Brusetti, C Marcenat, M Konczykowski, V Mosser, KH Kim, BW Kang, HS Lee, et al. "Geometrical barriers and lower critical field in MgB_2 single crystals." In: *Physical Review B* 70.18 (2004), p. 180504.
- [96] Z Pribulova, Thierry Klein, J Kacmarcik, C Marcenat, M Konczykowski, SL Bud'Ko, M Tillman, and PC Canfield. "Upper and lower critical magnetic fields of superconducting $\text{NdFeAsO}_{1-x}\text{F}_x$ single crystals studied by Hall-probe magnetization and specific heat." In: *Physical Review B* 79.2 (2009), p. 020508.
- [97] WC Lee and DC Johnston. "Superconducting and normal-state magnetic-susceptibility anisotropy in $\text{YBa}_2\text{Cu}_3\text{O}_7$." In: *Physical Review B* 41.4 (1990), p. 1904.
- [98] AS Klepikova, TB Charikova, MR Popov, EA Stepanova, and AA Ivanov. "Magnetic susceptibility anisotropy of electron overdoped high temperature superconductor $\text{Nd}_{2-x}\text{Ce}_x\text{CuO}_4$." In: *Journal of Physics and Chemistry of Solids* 148 (2021), p. 109770.
- [99] Mingquan He, Liran Wang, Frédéric Hardy, Liping Xu, Thomas Wolf, Peter Adelman, and Christoph Meingast. "Evidence for short-range magnetic order in the nematic phase of FeSe from anisotropic

- in-plane magnetostriction and susceptibility measurements." In: *Physical Review B* 97.10 (2018), p. 104107.
- [100] JQ Yan, Andreas Kreyssig, Shibabrata Nandi, N Ni, Sergey L Bud'ko, A Kracher, RJ McQueeney, RW McCallum, TA Lograsso, AI Goldman, et al. "Structural transition and anisotropic properties of single-crystalline SrFe_2As_2 ." In: *Physical Review B* 78.2 (2008), p. 024516.
- [101] JPC Ruff, J-H Chu, H-H Kuo, RK Das, H Nojiri, IR Fisher, and Z Islam. "Susceptibility anisotropy in an iron arsenide superconductor revealed by X-ray diffraction in pulsed magnetic fields." In: *Physical review letters* 109.2 (2012), p. 027004.
- [102] Ni Ni, SL Bud'ko, A Kreyssig, S Nandi, GE Rustan, AI Goldman, S Gupta, JD Corbett, A Kracher, and PC Canfield. "Anisotropic thermodynamic and transport properties of single-crystalline $\text{Ba}_{1-x}\text{K}_x\text{Fe}_2\text{As}_2$ ($x = 0$ and 0.45)." In: *Physical Review B* 78.1 (2008), p. 014507.
- [103] Mingquan He, Liran Wang, Felix Ahn, Frédéric Hardy, Thomas Wolf, Peter Adelman, Jörg Schmalian, Ilya Eremin, and Christoph Meingast. "Dichotomy between in-plane magnetic susceptibility and resistivity anisotropies in extremely strained BaFe_2As_2 ." In: *Nature communications* 8.1 (2017), pp. 1–6.
- [104] YK Kim, WS Jung, GR Han, K-Y Choi, K-H Kim, C-C Chen, TP Devereaux, A Chainani, J Miyawaki, Y Takata, et al. "Existence of Orbital Order and its Fluctuation in $\text{Ba}(\text{Fe}_{1-x}\text{Co}_x)_2\text{As}_2$ Revealed by X-ray Absorption Spectroscopy." In: *arXiv preprint arXiv:1112.2243* (2011).
- [105] William D Gregory. "Superconducting transition width in pure gallium single crystals." In: *Physical Review* 165.2 (1968), p. 556.
- [106] KK Likharev. "Superconducting weak links." In: *Reviews of Modern Physics* 51.1 (1979), p. 101.

- [107] F Iga, AK Grover, Y Yamaguchi, Y Nishihara, N Goyal, and SV Bhat. "Irreversibility line and the hierarchy of weak links in $\text{Bi}_2\text{Sr}_2\text{CaCu}_2\text{O}_{8+\delta}$." In: *Physical Review B* 51.13 (1995), p. 8521.
- [108] Lina E. Klintberg, Swee K. Goh, Shigeru Kasahara, Yusuke Nakai, Kenji Ishida, Michael Sutherland, Takasada Shibauchi, Yuji Matsuda, and Takahito Terashima. "Chemical Pressure and Physical Pressure in $\text{BaFe}_2(\text{As}_{1-x}\text{P}_x)_2$." In: *Journal of the Physical Society of Japan* 79.12 (2010), p. 123706.
- [109] S Senoussi, C Aguillon, and P Manuel. "The origin of the low field peak in the hysteresis cycle of high- T_c oxides and the influence of magnetic pinnings." In: *Physica C: Superconductivity* 175.1-2 (1991), pp. 202–214.
- [110] David R Nelson. "Vortex entanglement in high- T_c superconductors." In: *Physical review letters* 60.19 (1988), p. 1973.
- [111] David R Nelson and H Sebastian Seung. "Theory of melted flux liquids." In: *Physical Review B* 39.13 (1989), p. 9153.
- [112] Shigeyuki Ishida, Dongjoon Song, Hiraku Ogino, Akira Iyo, Hiroshi Eisaki, Masamichi Nakajima, Jun-ichi Shimoyama, and Michael Eisterer. "Doping-dependent critical current properties in K, Co, and P-doped BaFe_2As_2 single crystals." In: *Physical Review B* 95.1 (2017), p. 014517.
- [113] G Blatter, VB Geshkenbein, and JAG Koopmann. "Weak to strong pinning crossover." In: *Physical review letters* 92.6 (2004), p. 067009.
- [114] S Demirdiř, Yanina Fasano, Shigeru Kasahara, Takahito Terashima, Takasada Shibauchi, Yuji Matsuda, Marcin Konczykowski, Hernan Pastoriza, and Cornelis Jacominus Van Der Beek. "Disorder, critical currents, and vortex pinning energies in isovalently substituted $\text{BaFe}_2(\text{As}_{1-x}\text{P}_x)_2$." In: *Physical Review B* 87.9 (2013), p. 094506.

- [115] CJ Van der Beek, M Konczykowski, A Abal'oshev, I Abal'osheva, P Gierlowski, SJ Lewandowski, MV Indenbom, and S Barbanera. "Strong pinning in high-temperature superconducting films." In: *Physical Review B* 66.2 (2002), p. 024523.
- [116] CJ Van der Beek, Giancarlo Rizza, Marcin Konczykowski, Pierre Fertey, Isabelle Monnet, Thierry Klein, Ryuji Okazaki, Motoyuki Ishikado, Hijiri Kito, Akira Iyo, et al. "Flux pinning in $\text{PrFeAsO}_{0.9}$ and $\text{NdFeAsO}_{0.9}\text{F}_{0.1}$ superconducting crystals." In: *Physical Review B* 81.17 (2010), p. 174517.
- [117] Huai-Xiang Huang, Wei Li, Yi Gao, Yan Chen, and Fu-Chun Zhang. "Anomalous sharp peak in the London penetration depth induced by the nodeless-to-nodal superconducting transition in $\text{BaFe}_2(\text{As}_{1-x}\text{P}_x)_2$." In: *Physical Review B* 100.14 (2019), p. 144501.
- [118] Derrick Van Gennep, Abdelwahab Hassan, Huiqian Luo, and Mahmoud Abdel-Hafiez. "Sharp peak of the critical current density in $\text{BaFe}_{2-x}\text{Ni}_x\text{As}_2$ at optimal composition." In: *Physical Review B* 101.23 (2020), p. 235163.
- [119] Shaban Reza Ghorbani, Xiao Lin Wang, Mahboobeh Shahbazi, SX Dou, and CT Lin. "Fluctuation of mean free path and transition temperature induced vortex pinning in $(\text{Ba}, \text{K})\text{Fe}_2\text{As}_2$ superconductors." In: *Applied Physics Letters* 100.21 (2012), p. 212601.
- [120] F Parvin and SH Naqib. "Structural, elastic, electronic, thermodynamic, and optical properties of layered BaPd_2As_2 pnictide superconductor: a first principles investigation." In: *Journal of Alloys and Compounds* 780 (2019), pp. 452–460.
- [121] PL Paulose, S Ramakrishnan, Z Hossain, et al. "Doping dependent evolution of magnetism and superconductivity in $\text{Eu}_{1-x}\text{K}_x\text{Fe}_2\text{As}_2$ ($x=0-1$) and temperature dependence of the lower critical field H_{c1} ." In: *Journal of Physics: Condensed Matter* 23.45 (2011), p. 455702.

- [122] Ruslan Prozorov and Vladimir G Kogan. "London penetration depth in iron-based superconductors." In: *Reports on Progress in Physics* 74.12 (2011), p. 124505.
- [123] Jiun-Haw Chu, James G Analytis, Kristiaan De Greve, Peter L McMahon, Zahirul Islam, Yoshihisa Yamamoto, and Ian R Fisher. "In-plane resistivity anisotropy in an underdoped iron arsenide superconductor." In: *Science* 329.5993 (2010), pp. 824–826.
- [124] E Hassinger, G Gredat, F Valade, S René de Cotret, A Juneau-Fecteau, J-Ph Reid, H Kim, MA Tanatar, R Prozorov, B Shen, et al. "New Phase Induced by Pressure in the Iron-Arsenide Superconductor K-Ba₁₂₂." In: *arXiv preprint arXiv:1205.6730* (2012).
- [125] NJ Hillier, N Foroozani, DA Zocco, JJ Hamlin, RE Baumbach, IK Lum, MB Maple, and JS Schilling. "Intrinsic dependence of T_c on hydrostatic (He-gas) pressure for superconducting LaFePO, PrFePO, and NdFePO single crystals." In: *Physical Review B* 86.21 (2012), p. 214517.
- [126] F Chen, L Gao, RL Meng, YY Xue, and CW Chu. "Hydrostatic pressure on HgBa₂CaCu₂O_{6+δ} and HgBa₂Ca₂Cu₃O_{8+δ}." In: *Journal of Applied Physics* 76.10 (1994), pp. 6941–6943.
- [127] L Gao, YY Xue, F Chen, Q Xiong, RL Meng, D Ramirez, CW Chu, JH Eggert, and HK Mao. "Superconductivity up to 164 K in HgBa₂Ca_{m-1}Cu_mO_{2m+2+δ} (m= 1, 2, and 3) under quasihydrostatic pressures." In: *Physical Review B* 50.6 (1994), p. 4260.
- [128] CR Rotundu and RJ Birgeneau. "First-and second-order magnetic and structural transitions in BaFe_{2(1-x)}Co_{2x}As₂." In: *Physical Review B* 84.9 (2011), p. 092501.
- [129] Robert D Shannon. "Revised effective ionic radii and systematic studies of interatomic distances in halides and chalcogenides." In: *Acta crystallographica section A: crystal physics, diffraction, theoretical and general crystallography* 32.5 (1976), pp. 751–767.

- [130] Yanchao Chen, Xingye Lu, Meng Wang, Huiqian Luo, and Shiliang Li. "Systematic growth of $\text{BaFe}_{2-x}\text{Ni}_x\text{As}_2$ large crystals." In: *Superconductor Science and Technology* 24.6 (2011), p. 065004.
- [131] N Ni, A Thaler, JQ Yan, A Kracher, E Colombier, SL Bud'Ko, PC Canfield, and ST Hannahs. "Temperature versus doping phase diagrams for $\text{Ba}(\text{Fe}_{1-x}\text{TM}_x)_2\text{As}_2$ (TM= Ni, Cu, Cu/Co) single crystals." In: *Physical Review B* 82.2 (2010), p. 024519.
- [132] David J Singh. "Electronic structure and doping in BaFe_2As_2 and LiFeAs : Density functional calculations." In: *Physical Review B* 78.9 (2008), p. 094511.
- [133] Takayoshi Katase, Hikaru Sato, Hidenori Hiramatsu, Toshio Kamiya, and Hideo Hosono. "Unusual pressure effects on the superconductivity of indirectly electron-doped $(\text{Ba}_{1-x}\text{La}_x)\text{Fe}_2\text{As}_2$ epitaxial films." In: *Physical Review B* 88.14 (2013), p. 140503.
- [134] KS Pervakov, VA Vlasenko, EP Khlybov, A Zaleski, VM Pudalov, and Yu F Eltsev. "Bulk magnetization and strong intrinsic pinning in Ni-doped BaFe_2As_2 single crystals." In: *Superconductor Science and Technology* 26.1 (2012), p. 015008.
- [135] DL Sun, Y Liu, and CT Lin. "Comparative study of upper critical field H_{c2} and second magnetization peak H_{sp} in hole-and electron-doped BaFe_2As_2 superconductor." In: *Physical Review B* 80.14 (2009), p. 144515.
- [136] Mahboobeh Shahbazi, XL Wang, ZW Lin, JG Zhu, SX Dou, and KY Choi. "Magnetoresistance, critical current density, and magnetic flux pinning mechanism in nickel doped BaFe_2As_2 single crystals." In: *Journal of Applied Physics* 109.7 (2011), 07E151.
- [137] Shyam Sundar, Said Salem Sugui Jr, Edmund Lovell, Alexander Vanstone, Lesley F Cohen, Dongliang Gong, Rui Zhang, Xingye Lu, Huiqian Luo, and Luis Ghivelder. "Doping Dependence of the Sec-

- ond Magnetization Peak, Critical Current Density and Pinning Mechanism in $\text{BaFe}_{2-x}\text{Ni}_x\text{As}_2$ Pnictide Superconductors." In: *ACS Applied Electronic Materials* (2019).
- [138] T Shibauchi, A Carrington, and Y Matsuda. "A quantum critical point lying beneath the superconducting dome in iron pnictides." In: *Annu. Rev. Condens. Matter Phys.* 5.1 (2014), pp. 113–135.
- [139] Zhuan Xu, Qian Tao, Linjun Li, Jingqin Shen, Xiao Lin, and Guanghan Cao. "Ni doping effect and phase diagram of Ni-doped $\text{BaFe}_{2-x}\text{Ni}_x\text{As}_2$." In: *Physica C: Superconductivity and its applications* 470 (2010), S447–S448.
- [140] NR Werthamer, Ef Helfand, and PC Hohenberg. "Temperature and purity dependence of the superconducting critical field, H_{c2} . III. Electron spin and spin-orbit effects." In: *Physical Review* 147.1 (1966), p. 295.
- [141] G Bioletti, GVM Williams, MA Susner, TJ Haugan, DM Uhrig, and SV Chong. "The effect of pressure and doping on the critical current density in nickel doped BaFe_2As_2 ." In: *Superconductor Science and Technology* 32.6 (2019), p. 064001.
- [142] A Yamamoto, J Jaroszynski, C Tarantini, L Balicas, J Jiang, A Gurevich, DC Larbalestier, Rongying Jin, AS Sefat, Michael A McGuire, et al. "Small anisotropy, weak thermal fluctuations, and high field superconductivity in Co-doped iron pnictide $\text{Ba}(\text{Fe}_{1-x}\text{Co}_x)_2\text{As}_2$." In: *Applied Physics Letters* 94.6 (2009), p. 062511.
- [143] AK Pramanik, S Aswartham, AUB Wolter, S Wurmehl, V Kataev, and B Büchner. "Flux jumps and vortex pinning in $\text{Ba}_{0.65}\text{Na}_{0.35}\text{Fe}_2\text{As}_2$ single crystals." In: *arXiv preprint arXiv:1205.2210* (2012).
- [144] Tatiana E Kuzmicheva, Andrei Viktorovich Muratov, Svetoslav Aleksandrovich Kuzmichev, Andrei Vladimirovich Sadakov, Yu A Aleshchenko, Vladimir Aleksandrovich Vlasenko, Viktor Petrovich Martovitsky,

- Kirill Sergeevich Pervakov, Yu F Eltsev, and Vladimir Moiseevich Pudalov. "On the structure of the superconducting order parameter in high-temperature Fe-based superconductors." In: *Physics-Uspekhi* 60.4 (2017), p. 419.
- [145] HG Schnack, R Griessen, JG Lensink, and Wen Hai-Hu. "Generalized inversion scheme for the determination of activation energies from flux-creep experiments in high- T_c superconductors." In: *Physical Review B* 48.17 (1993), p. 13178.
- [146] VA Vlasenko, KS Pervakov, S Yu Gavrillkin, and Yu F Eltsev. "Unconventional pinning in iron based superconductors of 122 family." In: *Physics Procedia* 67 (2015), pp. 952–957.
- [147] Yan Zheng, Yuxing Wang, Frederic Hardy, Anna E Böhmer, Thomas Wolf, Christoph Meingast, and Rolf Lortz. "High-pressure evolution of the specific heat of a strongly underdoped Ba (Fe_{0.963}Co_{0.037})₂As₂ iron-based superconductor." In: *Physical Review B* 89.5 (2014), p. 054514.
- [148] H Amitsuka, K Matsuda, M Yokoyama, I Kawasaki, S Takayama, Y Ishihara, K Tenya, N Tateiwa, TC Kobayashi, and H Yoshizawa. "Dependence of pressure-induced phase transitions on pressure-transmitting media in the heavy-electron superconductor URu₂Si₂." In: *Physica B: Condensed Matter* 403.5-9 (2008), pp. 925–927.
- [149] VA Sidorov and RA Sadykov. "Hydrostatic limits of Fluorinert liquids used for neutron and transport studies at high pressure." In: *Journal of Physics: Condensed Matter* 17.40 (2005), S3005.
- [150] Fazel Fallah Tafti, JP Clancy, M Lapointe-Major, C Collignon, S Faucher, JA Sears, A Juneau-Fecteau, N Doiron-Leyraud, AF Wang, X-G Luo, et al. "Sudden reversal in the pressure dependence of T_c in the iron-based superconductor CsFe₂As₂: A possible link between inelastic scattering and pairing symmetry." In: *Physical Review B* 89.13 (2014), p. 134502.

- [151] FF Tafti, A Juneau-Fecteau, M-E Delage, S René De Cotret, J-Ph Reid, AF Wang, XG Luo, XH Chen, N Doiron-Leyraud, and Louis Taillefer. "Sudden reversal in the pressure dependence of T_c in the iron-based superconductor KFe_2As_2 ." In: *Nature Physics* 9.6 (2013), pp. 349–352.
- [152] FF Tafti, A Ouellet, A Juneau-Fecteau, S Faucher, M Lapointe-Major, N Doiron-Leyraud, AF Wang, X-G Luo, XH Chen, and Louis Taillefer. "Universal V-shaped temperature-pressure phase diagram in the iron-based superconductors KFe_2As_2 , $RbFe_2As_2$, and $CsFe_2As_2$." In: *Physical Review B* 91.5 (2015), p. 054511.
- [153] SJ Zhang, XC Wang, R Sammynaiken, JS Tse, LX Yang, Z Li, QQ Liu, S Desgreniers, Y Yao, HZ Liu, et al. "Effect of pressure on the iron arsenide superconductor Li_xFeAs ($x = 0.8, 1.0, 1.1$)." In: *Physical Review B* 80.1 (2009), p. 014506.
- [154] Melissa Gooch, Bing Lv, Joshua H Tapp, Zhongjia Tang, Bernd Lorenz, Arnold M Guloy, and Paul CW Chu. "Pressure shift of the superconducting T_c of $LiFeAs$." In: *EPL (Europhysics Letters)* 85.2 (2009), p. 27005.
- [155] Gaston Garbarino, Amadou Sow, Pascal Lejay, André Sulpice, Pierre Toulemonde, Mohamed Mezouar, and Manuel Nunez-Regueiro. "High-temperature superconductivity (T_c onset at 34 K) in the high-pressure orthorhombic phase of $FeSe$." In: *EPL (Europhysics Letters)* 86.2 (2009), p. 27001.
- [156] S Margadonna, Y Takabayashi, Y Ohishi, Y Mizuguchi, Y Takano, T Kagayama, T Nakagawa, M Takata, and K Prassides. "Pressure evolution of the low-temperature crystal structure and bonding of the superconductor $FeSe$ ($T_c = 37$ K)." In: *Physical Review B* 80.6 (2009), p. 064506.
- [157] Yuh Yamada, Takehiko Matsumoto, Yoshinari Kaieda, and Nobuo Mōri. "Pressure effects on T_c of superconductor $YBa_2Cu_4O_8$." In: *Japanese journal of applied physics* 29.2A (1990), p. L250.

- [158] Ayako Yamamoto, Nao Takeshita, Chieko Terakura, and Yoshinori Tokura. "High pressure effects revisited for the cuprate superconductor family with highest critical temperature." In: *Nature communications* 6.1 (2015), pp. 1–7.
- [159] Masaki Mito, Michael J Pitcher, Wilson Crichton, Gaston Garbarino, Peter J Baker, Stephen J Blundell, Paul Adamson, Dinah R Parker, and Simon J Clarke. "Response of superconductivity and crystal structure of LiFeAs to hydrostatic pressure." In: *Journal of the American Chemical Society* 131.8 (2009), pp. 2986–2992.
- [160] F Thomas, J Thomasson, C Ayache, C Geibel, and F Steglich. "Precise determination of the pressure dependence of T_c in the heavy-fermion superconductor $CeCu_2Si_2$." In: *Physica B: Condensed Matter* 186 (1993), pp. 303–306.
- [161] David W Tam, Yu Song, Haoran Man, Sky C Cheung, Zhiping Yin, Xingye Lu, Weiyi Wang, Benjamin A Frandsen, Lian Liu, Zizhou Gong, et al. "Uniaxial pressure effect on the magnetic ordered moment and transition temperatures in $BaFe_{2-x}T_xAs_2$ ($T = Co, Ni$)." In: *Physical Review B* 95.6 (2017), p. 060505.
- [162] K Ahilan, J Balasubramaniam, FL Ning, T Imai, AS Sefat, Rongying Jin, Michael A McGuire, Brian C Sales, and David Mandrus. "Pressure effects on the electron-doped high T_c superconductor $Ba(Fe_{1-x}Co_x)_2As_2$." In: *Journal of Physics: Condensed Matter* 20.47 (2008), p. 472201.
- [163] Re3Data.Org. *Perfluorotripentylamine*.

